



# Experimental study and numerical modeling of crushing and mechanical behavior of rockfill materials : influence of particle size

Xialong Zhao

## ► To cite this version:

Xialong Zhao. Experimental study and numerical modeling of crushing and mechanical behavior of rockfill materials : influence of particle size. Civil Engineering. Université de Lille, 2021. English. NNT : 2021LILUI047 . tel-03528523

**HAL Id: tel-03528523**

**<https://theses.hal.science/tel-03528523>**

Submitted on 17 Jan 2022

**HAL** is a multi-disciplinary open access archive for the deposit and dissemination of scientific research documents, whether they are published or not. The documents may come from teaching and research institutions in France or abroad, or from public or private research centers.

L'archive ouverte pluridisciplinaire **HAL**, est destinée au dépôt et à la diffusion de documents scientifiques de niveau recherche, publiés ou non, émanant des établissements d'enseignement et de recherche français ou étrangers, des laboratoires publics ou privés.

**THÈSE DE DOCTORAT  
DE L'UNIVERSITÉ DE LILLE**

**LABORATOIRE DE MÉCANIQUE, MULTIPHYSIQUE ET  
MULTIECHELLE (UMR 9013)**

Présentée par

**Xiaolong ZHAO**

pour obtenir le grade de

**DOCTEUR DE L'UNIVERSITÉ DE LILLE**

Domaine

**GÉNIE CIVIL**

Sujet de la thèse

**Experimental study and numerical modeling of crushing  
and mechanical behavior of rockfill materials:  
influence of particle size  
(Etude expérimentale et modélisation numérique de la  
rupture et le comportement mécanique des enrochements:  
influence de la taille des particules)**

Soutenance le 9 juillet 2021

<b>A. DAOUADJI, Professeur</b>	INSA Lyon	<i>Rapporteur</i>
<b>Z.Y. YIN, Professeur</b>	The Hong Kong Polytechnic University	<i>Rapporteur</i>
<b>J.G. ZHU, Professeur</b>	Hohai University	<i>Membre</i>
<b>Y. MALECOT, Professeur</b>	Université Grenoble Alpes	<i>Président</i>
<b>J.B. COLLIAT, Professeur</b>	Université de Lille	<i>Directeur de thèse</i>
<b>Y. JIA, MCF</b>	Université de Lille	<i>Co-directeur de thèse</i>

**LaMcube - UNIVERSITÉ LILLE**





# Abstract

Crushing and mechanical behaviours are two of the most important issues in the design and stability of rockfill constructions. The present thesis is devoted to experimental investigation and numerical modelling of this mechanism by putting the emphasis on the influences of particle size. It is composed of two parts: experimental investigation and numerical simulation.

To investigate the particle size effect on the crushing and strength of rockfill particles, single-particle crushing tests are carried out on Shuangjiangkou rockfill materials with three particle sizes. The obtained particle strength decreases with increasing particle size and can be described by the Weibull distribution with the Weibull modulus of 3.29. The influence of particle size on the minimum and maximum dry densities of studied materials is also investigated by using dry density tests. Finally, the mechanical behaviour of studied rockfill materials is studied via a series of triaxial compression tests. One observes that the stress-strain curves depend strongly on the particle size, for instance, the peak stress, the mobilized internal friction angle and the secant Young's modulus increase with increasing maximum particle size  $d_{max}$ . The experimental results exhibit that the effects of particle sizes are related to the combination effect of gradation and single particle strength.

The numerical simulations are performed by using an open-source discrete element software, YADE. Firstly, the single-particle crushing tests are simulated to understand the micro-mechanisms of the particle size effects on breakage characteristics of rockfill materials. Numerical simulation results exhibit that the flaw volume ratio is the key issue of size effects on particle strength. After that, a new breakage criterion considering the effects of coordination number is proposed. The formulation and implementation of proposed model and numerical method are first presented and discussed. Its efficiency in modelling the influence of particle size on the mechanical behaviour of rockfill materials are then demonstrated. The emphasis is to put on the effects of particle size on the crushing patterns and deformation behaviour. Comparisons between numerical results and experimental observations are presented.

Keywords: rockfill materials; size effects; mechanical behaviour; particle breakage; Weibull distribution; discrete element modelling, triaxial test.



# Résumé

La rupture et le comportement mécanique sont des mécanismes essentiels à prendre en compte dans la conception et l'étude de la durabilité des barrages poids en enrochement. La thèse est consacrée à l'étude expérimentale et à la modélisation numérique de ces deux mécanismes en mettant l'accent sur l'influence de la taille des particules. Le mémoire est composé de deux parties : une partie sur l'étude expérimentale et une autre partie sur les simulations numériques.

Afin d'étudier l'influence de la taille des particules sur la rupture des particules d'enrochement, des essais de broyage avec une seule particule sont effectués sur les enrochements de Shuangjiangkou avec trois tailles différentes. La résistance à l'écrasement des particules diminue avec l'augmentation de la taille et peut être décrite par la loi de Weibull (module de Weibull de 3,29). L'influence de la taille des particules sur les densités sèches minimales et maximales des matériaux est également étudiée. Enfin, le comportement mécanique des enrochements est étudié via une série d'essais en compression triaxiale. Les résultats expérimentaux montrent que les courbes contrainte-déformation dépendent fortement de la taille des particules : contrainte maximale, angle de frottement interne mobilisé et module sécant augmentent avec l'augmentation de la taille maximale des particules  $d_{max}$ . Les résultats expérimentaux montrent que l'influence de la taille des particules est liée à l'effet combinatoire de la granulométrie et de la résistance à écrasement des grains.

Les simulations numériques sont effectuées en utilisant un logiciel open-source par la méthode des éléments discrets, Yade. Dans un premier temps, des essais de broyage à une seule particule sont simulés pour comprendre les micro-mécanismes des effets de la taille des particules sur les caractéristiques de la rupture des enrochements. Les résultats numériques montrent que le rapport volumique des défauts est le principal mécanisme qui contrôle les effets de taille sur la résistance des particules. En se basant sur les investigations expérimentales, un nouveau critère de rupture prenant en compte les effets de la taille des particules est proposé. La formulation et la mise en œuvre du modèle proposé et de la méthode numérique sont d'abord présentées et discutées. Son efficacité dans la modélisation de l'influence de la taille des particules sur le comportement mécanique des matériaux d'enrochement est ensuite démontrée. L'accent est mis sur les effets de la taille des particules sur la résistance à l'écrasement des grains et le comportement de

déformation. Les résultats numériques et les observations expérimentales sont comparés et analysés.

Mots clés : enrochements ; effet de la taille des particules ; comportement mécanique ; écrasement des particules ; loi de Weibull ; méthode des éléments discrets, essais triaxiaux.

# Acknowledgement

I would like to express my sincere gratitude to my director of thesis, Prof. Jean-Baptiste COLLIAT, who helped me all throughout the period of my research with his guidance, support, and encouragement. I would also like to thank my second supervisor, Mrs. Yun JIA, for her support and guidance in both my study and daily life.

I would like to specially thank Prof. Jungao ZHU for his patient guidance on my research in China. I will never get the chance to come to France without him. His rigorous attitude will always encourage me.

I would like to thank Mr. Hanbing BIAN for his support in both my study and daily life. And I would also thank all the members in Lamcube, including Prof. Jianfu SHAO, Mr. Wanqing SHEN, Mr. Jérôme HOSDEZ, Dr. Qier WU, Dr. Yue SUN, Dr. Zhan YU, Dr. Hailing SHI, Dr. Yue TONG, Dr. Xi CHEN, Dr. Jianjian ZHAO, Dr. Yudan JIN, Dr. Jinzhou BAI, Dr. Wang ZHANG, Dr. Liping ZHU, Dr. Jueliang CHEN, Dr. Siyu LIU, Dr. Changdong DING, Dr. Jing XUE, Dr. Meng WANG. They give me not only the help on research, but also more helps on my living in France.

I would also like to thank all the reviewers and members for my thesis defense.

Finally, special thanks to my parents and my friends in China for their continuous support, patience and encouragement.



# List of symbols

$b$	size effect parameter on particle strength for a material
$C_c$	coefficient of curvature
$C_u$	coefficient of uniformity
$d$	particle size (diameter)
$d_e$	Elementary ball size (diameter)
$d_M$	maximum particle size (diameter)
$d_n$	nominal particle size (diameter)
$d_r$	referenced particle size (diameter)
$D$	fractal dimension
$e$	void ratio
$e_y$	void ratio at the yield point in normal compression
$E$	Young's modulus
$F$	force
$k_n$	particle normal stiffness
$k_s$	particle shear stiffness
$M$	critical state ratio
$m$	Weibull modulus
$N$	number of objects
$N_e$	number of elementary balls
$p$	mean stress



---

$p_s$	mean stress corresponding to the particle failure in single-particle crushing test
$q$	deviatoric stress
$q_s$	value of deviatoric stress such that 37% of a given size of particles are stronger
$q_m$	mean deviatoric stress
$V$	volume
$\Gamma$	gamma function
$\varepsilon_1$	major principal strain
$\varepsilon_2$	intermediate principal strain
$\varepsilon_3$	minor principal strain
$\varepsilon_V$	volumetric strain\vertical strain
$\lambda$	normalized parameter
$\mu$	friction coefficient
$\nu$	Poisson's ratio
$\sigma$	stress
$\sigma_1$	major principal stress
$\sigma_2$	intermediate principal stress
$\sigma_3$	minor principal stress
$\sigma_f$	stress at failure
$\sigma_v$	vertical stress
$\sigma_y$	vertical yield stress in normal compression
$\varphi$	friction angle
$c$	cohesion of the material

# Contents

<b>Contents</b>	<b>i</b>
<b>I General introduction</b>	<b>1</b>
<b>II Literature review</b>	<b>5</b>
1 Rockfill and particle size effect . . . . .	5
2 Laboratory study . . . . .	8
2.1 Scaling techniques used for rockfill materials . . . . .	8
2.1.1 Scalping technique . . . . .	8
2.1.2 Parallel gradation technique . . . . .	9
2.1.3 Quadratic grain size distribution technique . . . . .	9
2.1.4 Replacement technique . . . . .	9
2.2 Laboratory compaction test . . . . .	10
2.2.1 Effect of density on the strength of soil sample . . . . .	10
2.2.2 Vibratory compaction tests for RFM . . . . .	12
2.2.3 Study the influence of particle size on the density of rockfill materials . . . . .	13
2.3 Laboratory shear test . . . . .	14
2.3.1 General introduction to laboratory shear tests . . . . .	14
2.3.2 Study the influence of particle size in shear tests . . . . .	14
3 Numerical analysis . . . . .	18
3.1 General introduction of DEM model . . . . .	18
3.1.1 Numerical implementation . . . . .	19
3.1.2 Governing equations . . . . .	19
3.1.3 Contact models . . . . .	20
3.1.4 Particle packing . . . . .	26
3.1.5 DEM codes . . . . .	28
3.2 DEM study of granular materials . . . . .	30
3.2.1 DEM study of grading effects . . . . .	30
3.2.2 DEM study of particle size effect . . . . .	32
4 Particle breakage in RFM . . . . .	33
4.1 Single particle strength . . . . .	34

4.1.1	Single-particle crushing test . . . . .	34
4.1.2	Weibull statistical distribution . . . . .	36
4.1.3	Size-hardening law . . . . .	39
4.1.4	DEM simulation of single particle crushing . . . . .	41
4.2	Experimental study of particle breakage . . . . .	42
4.2.1	Measurement of particle breakage . . . . .	43
4.2.2	Particle size effect on particle breakage . . . . .	44
4.3	DEM study of particle breakage . . . . .	45
4.3.1	Bonded particle model (BPM) . . . . .	45
4.3.2	Population balance model (PBM) . . . . .	46
5	Research scope . . . . .	49

### **III Experimental study of the particle size effects on the crushing and mechanical behavior of RFM**

**51**

1	Introduction . . . . .	51
2	Rockfill materials . . . . .	52
3	Single-particle crushing tests . . . . .	54
4	Density and triaxial test programs . . . . .	56
4.1	Test apparatus . . . . .	56
4.2	Test procedure . . . . .	57
5	Experimental results of density and triaxial tests . . . . .	58
5.1	Particle size effect on dry density . . . . .	58
5.2	Particle size effect on stress-strain-volume relationship . . . . .	61
5.3	Particle size effect on strength indexes . . . . .	62
5.4	Particle size effect on deformation indexes . . . . .	63
5.5	Particle size effect on characteristic stress state . . . . .	65
6	Discussion . . . . .	66
6.1	Fractal behavior . . . . .	66
6.2	Relative particle breakage . . . . .	71
7	Conclusions . . . . .	73

### **IV Influence of particle size on the breakage characteristics of rockfill particles in single-particle crushing tests**

**75**

1	Introduction . . . . .	75
2	Weibull statistical analysis of single-particle crushing tests . . . . .	76
2.1	Weibull distribution for brittle materials . . . . .	76

2.2	Validation of Weibull distribution . . . . .	77
2.3	Particle size effects on the tensile strength of studied rockfill materials . . . . .	80
3	DEM modelling of particle size effects . . . . .	84
3.1	Constitutive model used in Yade . . . . .	84
3.2	Model calibration: single-particle crushing simulation . . . . .	87
3.2.1	Preliminary study . . . . .	87
3.2.2	Simulation of single-particle crushing test . . . . .	91
3.2.3	Model validation using Buckingham $\pi$ theorem . . . . .	93
3.3	Numerical modelling of particle size effects . . . . .	94
3.3.1	Effects of agglomerate size and internal flaws . . . . .	95
3.3.2	Effect of flaw size . . . . .	96
3.3.3	Effect of flaw number . . . . .	97
3.3.4	Effect of flaw volume ratio . . . . .	98
4	Conclusions . . . . .	99

## V Influence of particle size on the mechanical behavior of studied rockfill materials in oedometer tests 101

1	Introduction . . . . .	101
2	Numerical analysis of the effect of coordination number on the crushing of rockfill particles . . . . .	104
2.1	Influence of coordination number on the crushing pattern of crushable agglomerate . . . . .	107
2.2	Influence of coordination number on the crushing strength of crushable agglomerate . . . . .	108
2.3	Partial conclusion . . . . .	110
3	Proposition of a new breakage criterion for rockfill particles considering the effect of coordination number . . . . .	110
3.1	Proposition of a breakage criterion . . . . .	111
3.2	Simulation setup . . . . .	114
4	Numerical simulation of oedometer tests . . . . .	116
4.1	Parametric study . . . . .	118
4.2	Numerical simulation of the oedometer test with the nominal diameter $d_n = 2.5$ mm . . . . .	121
4.3	Numerical analysis of the effects of particle size . . . . .	124
5	Comparison of the proposed breakage criterion with different breakage criteria	125

5.1	NCL and PSD . . . . .	126
5.2	Evolution of $CN$ . . . . .	127
5.3	Evolution of particle stress . . . . .	130
6	Conclusions . . . . .	132
<b>VI Conclusions and perspectives</b>		<b>135</b>
1	Conclusions . . . . .	135
2	Perspectives . . . . .	136
<b>Bibliography</b>		<b>139</b>

# Chapter I

## General introduction

As an endless and clean energy, the hydro-power has been widely developed in the world, and many rockfill dams have been constructed in the last decades ([Marachi et al., 1969](#); [Varadarajan et al., 2003](#); [Charles, 2008](#); [Hu et al., 2011](#); [Tabibnejad et al., 2015](#); [Gupta, 2016](#); [Xiao et al., 2016](#)). China is rich in hydroelectric resource, nearly 80% of which exists in the mid-western region. However, the current hydro-power is still under development, which is mainly through the construction of high dams ([Xiao et al., 2016](#)). The rockfill dam is widely used in the hydro-power engineering due to its easy material selection, low cost, simple structure, capacity to absorb large seismic energy and adaptability to various types of foundations.

As rockfill materials are generally obtained from rock quarry or riverbed, a wide range of particle sizes is observed. Nowadays, the particle size of rockfill materials may be up to more than 1.0m ([Varadarajan et al., 2006, 2003](#)). Under the high stress field of rockfill dams, the occurrence of particle crushing significantly alters the mechanical behaviour of rockfill materials ([Coop et al., 2004](#); [Daouadji and Hicher, 2010](#); [Daouadji et al., 2001](#); [Kh et al., 2011](#); [Lade et al., 1996](#); [Luzzani and MR, 2002](#); [McDowell and Bolton, 1998](#); [Tarantino and Hyde, 2005](#); [Varadarajan et al., 2003](#)). Moreover, as the force transmission depends on the number of contacts between particles ([Ben-Nun and Einav, 2008](#); [Lobo-Guerrero et al., 2006](#)), the packing of assembly has an important impact on the breakage mechanics of rockfill materials. In view of this, the design and durability of rockfill dams require a good understanding of the influence of particle size on the crushing and mechanical behaviour of rockfill materials.

In the literature, different types of laboratory tests have been developed to study the particle breakage and the mechanical behaviour of granular materials: single-particle crushing tests, oedometer tests, triaxial compression tests and plane strain tests, etc.

According to the crushing of particle, single-particle crushing tests are usually used to study the breakage characteristics of granular materials (e.g., sand, ballast and rockfill) (Cil and Alshibli, 2012; Altuhafi and Coop, 2011; Cheshomi and Sheshde, 2013; Darvell, 1990; McDowell and Bolton, 1998; Nakata et al., 1999; Xiao et al., 2020). The breakage behaviour of particles depends on the material properties (i.e. size (Zhou et al., 2016), structure (Jansen and Stoyan, 2000; Lobo-Guerrero and Vallejo, 2006a; McDowell and Humphreys, 2002) and shape (Huang et al., 2020; Le Pen et al., 2013)) and the stress paths, etc. In addition, the influence of particle breakage on the mechanical behaviours of rockfill materials are also investigated by different researchers (Daouadji and Hicher, 2010; Daouadji et al., 2001; Hardin, 1985; Lade et al., 1996; Marsal, 1967; Ovalle et al., 2014; Varadarajan et al., 2003; Wang et al., 2021; Xiao et al., 2014b, 2020). The obtained results exhibit that the particle breakage induces the irreversible volumetric contraction in one-dimensional and isotropic compression tests. Under high confining pressures, the particle breakage induces the decrease of volumetric dilation in triaxial compression tests (Hardin, 1985; Wang et al., 2021; Xiao et al., 2014b). Moreover, the internal frictional angle is strongly affected by particle breakage (Ovalle et al., 2014; Tarantino and Hyde, 2005; Varadarajan et al., 2003). The present thesis focus on the influence of particle size on the crushing and mechanical behaviour of rockfill materials.

According to the effects of particle size, numerous experiment results exhibit that for natural materials (e.g., sand and ballast), the individual particle strength increases with decreasing particle size (de Bono, 2013; Wang and Yan, 2013; Nakata et al., 1999; Zhou et al., 2016; Jansen and Stoyan, 2000; Lobo-Guerrero and Vallejo, 2006a; Nakata et al., 2001b; Drlik, 1987; Lee, 1992; Lim et al., 2004; McDowell, 2002; McDowell and Amon, 2000; McDowell et al., 1996; Rozenblat et al., 2011; Shao et al., 2020; Zhong et al., 2014). These observations are generally explained by the fact that large particles have more and bigger flaws than small particles (Alonso et al., 2012; Lade et al., 1996; Drlik, 1987; Zhong et al., 2014; Frossard et al., 2012; Hardin, 1985; Liu et al., 1998). Recently, the X-ray microtomography ( $\mu$ CT) has been used for the analysis of the crushing tests. For instance, Zhao et al. (2015) confirmed that the initial particle morphology, heterogeneity and mineralogy were three important factors in the identification of failure patterns. Moreover, Guida et al. (Guida et al., 2018) confirmed that the particles with high internal porosity had a propensity to be broken down in the one-dimensional compression tests. However, the effects of the particle size on the breakage characteristics and mechanical behaviour of rockfill materials still need a deep understanding at a microscopic level.

On the other hand, with the recent development in the theoretic and computational

techniques, the theoretical analysis and numerical simulation become more provocative and comprehensive approaches to study the particle size effects on the breakage characteristics and mechanical behaviour of granular materials. Theoretical research indicates that the particle breakage strength of some granular materials (e.g., sand and railway ballast) follows the Weibull distribution (Huang et al., 2020; Zhou et al., 2016; Lim et al., 2004; McDowell, 2002; McDowell and Amon, 2000; Ergenzinger et al., 2012; McDowell, 2001; Ovalle et al., 2014). In practice, the parameters of Weibull distribution can be determined by using the breakage strength of particles obtained from single-particle crushing tests. After that, the Weibull model can be used to predict the particle strength distributions observed in the laboratory tests or in the numerical simulations.

According to the numerical research, the discrete element method (DEM) has been widely used to simulate the particle crushing tests and study the mechanical behaviour of granular materials. The crushing grain is simulated by a bonded particle model (BPM) (Wang and Yan, 2013; Ergenzinger et al., 2012; Cil and Alshibli, 2015; Duriez et al., 2016; Li, 2013; Lim, 2004; Potyondy and Cundall, 2004; Scholtès and Donzé, 2013), in which it is represented as an agglomerate of bonded balls. The sample failure is modelled as the bond breakage within the agglomerate. As a result, the BPM is capable of reproducing the brittle behaviour of rock materials when the breakage occurs along the maximum stress zones. In the literature, several bonded particle models (BPM) have been used to analyse the crushing and mechanical characteristics of rock-like materials (Wang and Yan, 2013; Ergenzinger et al., 2012; Cil and Alshibli, 2015; Duriez et al., 2016; Lim, 2004; Scholtès and Donzé, 2013).

With respect to the bonded particle models, the population balance model (PBM) is more popular in DEM modelling of crushable granular materials. In PBM, the particle crushing is realized by the replacing the broken particles with several small fragments. With a computational economy (Weerasekara et al., 2013), it is capable of reproducing a relatively realistic particle size distribution compared to the BPM (de Bono and McDowell, 2016b). To correctly capture the breakage mechanics of granular materials, two most important issues in PBM are a breakage criterion for the detection of particle breakage and a particle spawning criterion for the fragment replacement modes (Ciantia et al., 2015; de Bono and McDowell, 2016a; Zheng and Tannant, 2018). The currently used breakage criteria can be divided into two categories: maximum contact force criteria (Aström and Herrmann, 1998; Ciantia et al., 2015; Couroyer et al., 2000; Elghezal et al., 2013; Hanley et al., 2015; Lobo-Guerrero and Vallejo, 2005a; Lobo-Guerrero et al., 2006; Marketos and Bolton, 2009) and stress tensor criteria (Ben-Nun and Einav, 2010; Esnault and Roux,



2013; McDowell and de Bono, 2013; Tsoungui et al., 1999; Zhou et al., 2020, 2016). The macro-mechanical behaviours of crushable granular materials can be reproduced by using these breakage criteria, with a fractal emerging in the particle size distribution (PSD). The maximum contact force criteria emphasizes the role of stress concentration in particle breakage, while the stress tensor criteria are proposed by considering the stress state of studied materials, e.g., octahedral shear strength (McDowell and de Bono, 2013). However, the effect of coordination number on the particle behaviour still needs further understanding. Moreover, most of the previous works focus on the sand and ballast materials, not on the rockfill materials. Therefore, there is still a lack of comprehension in the micro-mechanisms of the particle size effects on the crushing and mechanical characteristics of rockfill materials.

The objective of the present study is to analyse the influence of particle size on the crushing and mechanical behaviour of rockfill materials via a series of experimental tests and numerical simulations. Therefore, the thesis is composed of six chapters.

Chapter I is the general introduction of the thesis. Chapter II reviews the research works performed on the crushing and mechanical behaviour of rockfill materials, including the general introduction of rockfill materials, laboratory study of particle size effects, general introduction of discrete element method (DEM) and study of particle breakage. Chapter III mainly focuses on the experimental investigation of size effects on rockfill materials by using three types of laboratory tests, i.e., single-particle crushing, dry density and triaxial tests. Chapter IV focuses on the particle size effects on particle strength via a series of DEM simulations of single-particle crushing tests. Chapter V investigates the effect of coordination number on the particle strength and deformation behaviour of rockfill materials. A new breakage criterion is proposed and implemented in YADE. The oedometer tests performed with different particle sizes have been simulated and analysed. At last, chapter VI lists the main conclusions and some perspectives for the thesis.

# Chapter II

## Literature review

### 1 Rockfill and particle size effect

Rockfill is a coarse grained and free-draining natural material, which consists primarily of angular to sub-angular particles obtained by crushing parent rock or rounded/sub-rounded particles collected from riverbeds. Therefore, they are characterized as the coarse angular or rounded particles in the absence of pore pressure ([Gupta, 2016](#)). The mechanical behaviour of rockfill materials (RFM) are affected by a lot of factors, such as mineral composition, particle size, particle shape, gradation, relative density, stress history and loading conditions ([Varadarajan et al., 2003](#); [Honkanadavar and Sharma, 2014](#)).

In practice, the in-situ properties of rockfill materials used in a rockfill dam is firstly estimated by using a series of laboratory tests and measurements. In the laboratory, the samples are studied under similar conditions (compaction, saturation, and consolidation, etc.) as those in the dam. After that, during the exploration phase, the obtained results are verified by examining the samples taken from the dam after compaction. In order to get the reliable experiment results of rockfill materials, it is necessary to guarantee the laboratory conditions very close to the in-situ ones.

Nowadays, the maximum diameter of rockfill particles used in the field may be up to 1.2 m ([Varadarajan et al., 2006, 2003](#); [Honkanadavar and Sharma, 2014](#)), and the grain weight may be more than 2 tons. As a result, it is almost impossible to realize the laboratory conditions as those in the dam. Until now, no laboratory in the world is capable of studying a rockfill sample with the maximum particle diameter of 1 m. This impossibility is due to the following phenomena. In the triaxial compression tests, the sample diameter is at least six to ten times larger than the maximum particle diameter to avoid sampling scale problems ([1956](#)). In China, the required minimum value for the ratio of sample diameter

to the maximum particle diameter is 5 (CS, 1999). In addition, the height of the triaxial specimen is at least 2 to 2.5 times of its diameter in order to eliminate the influence of the cap and base friction (Bishop and Green, 1965). Therefore, if the maximum particle size in a rockfill dam is 0.6 m, the dimension of laboratory sample is 3 m in diameter and 6 m in height. Therefore, two types of tests are generally performed in order to analyse the physical properties and mechanical characteristics of rockfill materials: in-situ tests and laboratory tests.

For the in-situ tests, the direct shear tests are largely used by the researchers and engineers (Oyanguren et al., 2008; Liu, 2009; Xu et al., 2011; Wang and Arson, 2016) due to the ease in the sample preparation and loading. In the in-situ direct shear test, the compaction and consolidation of sample are very close to the in-situ conditions. The material characteristics obtained by this test are useful to verify the dam design. However, the size of shear box (usually 1.2 m  $\times$  1.2 m in square (Oyanguren et al., 2008; Liu, 2009)) is still too small with respect to the particle size. Furthermore, it can not study the rockfill materials under complex loading conditions.

On the other hand, the direct way to study the particle size effect of RFM is to develop super large-scale triaxial test equipments. Since 1960s, super large-scale triaxial test apparatus with diameter ranging from 1000 to 1200 mm have been developed successively in Mexico (Marsal, 1967), US (Marachi, 1969), Japan (Fukushima and Kitajima, 1998), France (Hu et al., 2011) and China (Kong et al., 2019). The maximum particle size  $d_M$  of samples can be closer to that of in-situ engineering conditions. However, many problems are encountered in practice with the increase of the specimen diameter, such as sample preparation, rubber membrane customization, measure and loading devices design, etc. These inconveniences lead to an increasing expense in laboratory preparation and testing. As a result, few related reports are available in the literature. Therefore, several scaling techniques have been developed to prepare the sample: the scalping technique (Zeller and Wullimann, 1957), the parallel gradation technique (Lowe, 1964), the quadratic grain size distribution technique (Fumagalli, 1969), the replacement technique (Frost, 1973), and the hybrid method (CS, 1999). After scaling, the maximum particle size is reduced (Stoeber, 2012). Fumagalli (1969) proposed that a laboratory gradation scaled from the field gradation should have similar grain size curves, void ratio and particle shape. Fig. II.1 shows a typical particle size distribution (PSD) curve and several scaled PSD curves obtained by using different scaling techniques. The prototype is the field gradation while  $d_M$  is the maximum particle size used in laboratory, and the particle fraction with diameter less than 5 mm is the fine fraction. In the scalping technique (Zeller and Wullimann,

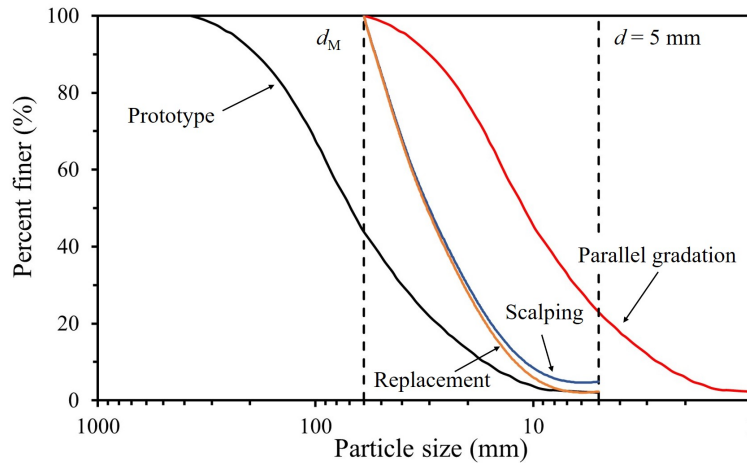


**Figure II .1:** Prototype and scaled particle size distributions of rockfill materials

1957), all the particles greater than  $d_M$  are discarded. All the fractions less than  $d_M$  are scaled-up by a constant factor. In the parallel gradation technique (Lowe, 1964), the prototype curve is translated rightward by a constant factor, such that the maximum particle size is reduced to  $d_M$ . Further caution is necessary to ensure if these fine fractions still represent the hardness, strength, and shape of studied materials (Fumagalli, 1970). Considering the influence of fine fraction on the properties of RFM, Frost (1973) introduced the replacement technique. The replacement method consists of replacing the oversize fraction by an amount of finer. In general, each scaling technique has its own method to take into account the field grading. For the scalping and replacement techniques, the fine fractions are kept constant, but the shapes of PSD curves are no longer similar to the prototype. The parallel gradation technique appears to be the most accurate method for the scaled gradations, but the increased fine components also induce some problems, such as drainage. And this technique also assumes constant mechanical properties, such as modulus of elasticity, particle surface roughness, particle shape, particle strength and plasticity, throughout the material (Marachi et al., 1969).

Even though scaling techniques have been applied widely in laboratory test and many research works have been performed on the scaled grain size distributions (Alonso et al., 2012), the particle size effect on the properties of RFM is not fully understood and needs to be further investigated. It is a very difficult task because many factors (aggregate density, particle shape, roundness, surface texture, strength, etc.) may be changed (Marachi, 1969, pg. 137; Frossard et al., 2012; Rodriguez et al., 2012; Zhong et al., 2014; Zou et al., 2018) when the field gradation is scaled. And these factors make it very difficult to find a reliable relationship between the scaled and field results.

## 2 Laboratory study

Strength and deformation properties of RFM depend on many factors which may be grouped in intrinsic and extrinsic ones. Mineralogy, surface hardness, shape and size of particles are intrinsic factors, while the placement conditions, compaction degrees and confining pressures are extrinsic ones (das Neves, 1991, pg. 20).

As RFM is a coarse-grained and free draining material, it can be considered as the coarse particles with the absence of pore-pressure. Due to the coarseness of particles and their interlocked state, RFM can not be experimentally tested as soils. As a result, laboratory specimens should be scaled down or re-constructed by compaction (das Neves, 1991, pg. 35). The sample must be of small size with respect to the prototype and the influence of boundary conditions. In view of this, the availability of extending the laboratory results to the in-situ behaviour of rockfill materials is still an open question and needs to be discussed. Therefore, many efforts have been performed by different researchers to eliminate the difference between scaled and prototype samples.

### 2.1 Scaling techniques used for rockfill materials

In order to get a satisfactory estimation of RFM property, the laboratory tests should be performed under the laboratory conditions as close as possible to these of the rockfill dams. As the size of RFM in a rockfill dam may be up to one meter in size, the tri-axial/oedometer sample should be more than 5 m in diameter in order to guarantee the accuracy of the laboratory results. In view of this, testing of a field grading of RFM is not possible in most cases. Therefore, scaling techniques have been developed to evaluate the in-situ properties of RFM. In practice, different techniques are used (Fig. II .1): Scalping technique (Zeller and Wullimann, 1957), parallel gradation technique (Lowe, 1964), quadratic grain size distribution technique (Fumagalli, 1969) and replacement technique (Frost, 1973). They will be briefly introduced in the following.

#### 2.1.1 Scalping technique

In scalping technique (Zeller and Wullimann, 1957) (Fig. II .1), all particles greater than the maximum particle size  $d_M$  will be replaced by small fractions. Meanwhile, the fine fractions with particle size less than  $d_M$  are all scaled-up with a constant factor. However, the similitude between in-situ and scale gradations is no longer satisfied as the shape of the particle size distribution (PSD) curve has been changed. In addition, laboratory specimens contain an excessive portion of fines compared with in-situ gradation.

Therefore, Das Neves (1991) proposed that it may be necessary to scalp the particles from two extremities of the PSD curve if the drainage problems are encountered. However, good drainage conditions in laboratory triaxial tests not only depend on the measure of fine content, but also the rate of axial displacement during loading process.

### 2.1.2 Parallel gradation technique

The parallel gradation technique, proposed by Lowe (1964), is known as a more realistic way to scale in-situ gradation. This method have been used to scale the rockfill materials, which were used in the construction of Shihmen Dam in Taiwan. The maximum particle size used in dam shell was 305 mm (12 inches) while the diameter of triaxial shear equipment was only 152 mm (6 inches). The tested samples were made with the coarse fraction of shell material, in which the size of each particle was one eighth size of the corresponding particle in the prototype in-situ material. Consequently, the in-situ gradation curve was arrived by rightward shifting the PSD curve of the tested material, as shown in Fig. II .1. A factor of one eight leads to the ratio of specimen diameter to the maximum particle size (SSR) to be 4, which is under the recommended minimum value of 6 proposed by Holtz and Gibbs (1956).

### 2.1.3 Quadratic grain size distribution technique

Fumagalli (1969) proposed a scaling technique by using the quadratic grain size distribution curves:

$$P = 100\sqrt{\frac{d}{d_M}} \quad (\text{II .1})$$

where  $P$  is the passing percentage by weight for a given nominal particle diameter  $d$ , and  $d_M$  is the maximum particle size for the modelled gradation. In the Eq. (II .1), it is assumed that the PSD curves can be mathematically defined in quadratic form. However, this assumption limits the applicability of Eq. (II .1) to the well-graded geomaterials.

### 2.1.4 Replacement technique

The disproportionate quantity of fine fractions in a scaled gradation may affect not only the strength parameters, such as internal friction angle  $\varphi$  (Park and Santamarina, 2017), but also the drainage conditions (das Neves, 1991). This phenomenon will have an important effect on the results of triaxial tests. In order to avoid the dramatic increase of fine fractions observed in scaling techniques (e.g., scalping and parallel scaled techniques), Frost (1973) proposed a replacement technique (Fig. II .1), in which the oversize fraction

was replaced by an amount of finer, but still coarse fraction ( $5 \text{ mm} < d < d_M$ ). The replacement technique includes the weight replacement, cross-sectional area replacement, surface replacement and volume replacement. The weight replacement is the mostly used one. On the other hand, the densities of the oversize and fine fractions are considered differently in the volume replacement technique. The replacement technique can limit the quantity of fine fractions in the scaled gradation and guarantee the drainage condition in laboratory test similar to the field one. However, the shape of the PSD curves is not similar to the prototype.

From the above, each scaling technique has its own merit and demerit. The parallel scaled gradation curve has the same shape as the field one, but the percentage of fine fractions increases significantly. The high percentage of fine fractions decreases the permeability of RFM, and then excessive pore pressure may be developed in the material. This phenomenon alters the effective shear strength of RFM (Indraratna et al., 1993). By using replacement technique, the scaled gradation curve can effectively limit the quantity of fine fractions in a given range, but the curve shape has been changed a lot. It should be noted that in China Standard (1999), a hybrid scaling technique is also widely used for the scaled samples in laboratory test. Actually, it is a combination of the parallel gradation and replacement techniques. In this technique, the prototype is firstly scaled with the parallel one, but the percentage of fine fractions ( $d < 5 \text{ mm}$ ) should not exceed 30%. Then, the oversized fractions will be scaled further with the replacement method. The hybrid scaling technique has both the advantages of the parallel gradation and replacement techniques. In the present study, the hybrid scaling technique has been used.

In conclusion, the scaling choices depend strongly on the type of rock and the field grading (das Neves, 1991; Le Pen et al., 2013). For hard rock and narrow grading, the parallel technique is suitable. For broader gradings with more fines, the scalping or replacement method may be the better one to evite the problem of more excessive fines. For easily crushable rock which degrades during compaction, the choice of scaling method is unimportant.

## 2.2 Laboratory compaction test

### 2.2.1 Effect of density on the strength of soil sample

The density characterizes the solid matter and inner pores of RFM, and then provide a good picture of the material (das Neves, 1991, pg. 15, 55). In general, the sample failure can be characterized by using the maximum deviatoric stress (maximum principal stress difference), whose value is related to the compression strength of specimen.

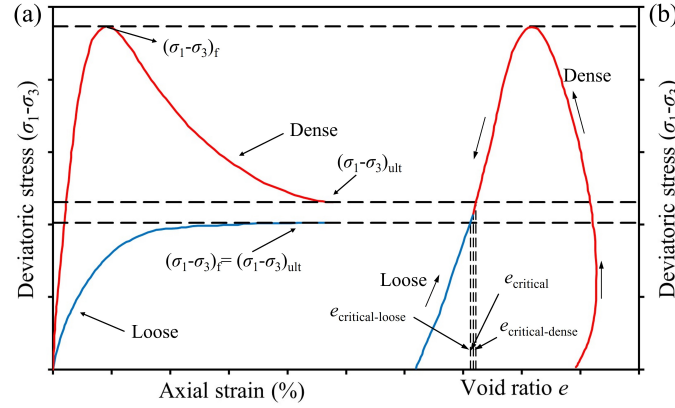


**Figure II .2:** Drained triaxial tests on the loose and dense specimens of a typical sand: (a) stress-strain curves; (b) void ratio changes during shear (after [Holtz et al., 1981](#), pg. 507)

The influence of density on the strength of granular materials (sand) is showed in Fig. II .2. Typical stress-strain curves of loose and dense sands are shown in Fig. II .2a, while the corresponding stress versus void ratio curves are presented in Fig. II .2b. Under low confining pressures, the initial density has a major effect on the shear resistance of granular material. When loose granular material (sand) is loaded, the deviatoric stress ( $\sigma_1 - \sigma_3$ ) increases progressively to its peak value and then keeps constant. Meanwhile, with the increase of applied stress, the void ratio  $e$  (ratio of the volume of voids to the volume of solid particles) decreases from  $e_{\text{loose}}$  to  $e_{cl}$  ( $e$  critical-loose), which is very close to the critical void ratio  $e_{\text{critical}}$  ([Casagrande, 1936](#)), when continuous deformation occurs with no changes in deviatoric stress. On the other hand, under low confining pressures, dense sand exhibits a peak strength, followed by strain softening. In the softening phase, the deviatoric stress decreases to a limit value, which is very close to  $(\sigma_1 - \sigma_3)_{\text{ult}}$  for loose sand.

The  $(\sigma_1 - \sigma_3)$ - $e$  curves exhibits a decrease of volumetric strain at the beginning of test. After that, the studied material expands up to the void ratio at failure  $e_{cd}$  and is very close to  $e_{cl}$ . Theoretically, both two values should be equal to the critical void ratio  $e_{\text{critical}}$ . Similarly, the same evolution tendency is observed in  $(\sigma_1 - \sigma_3)_{\text{ult}}$ . The eventual differences observed in experimental data are usually related to the difficulties in precise measurement of critical void ratio as well as the non-uniform stress distributions in the test specimens. These difficulties are accentuated under very high confining pressures ([Holtz et al., 1981](#)).

In practice, the strength of soil specimens is evaluated via the void ratio, compactive effort or the relative density. However, in the case of different types of soil or one type



with different grain sizes, these characteristics may be inaccurate and lead to conflicting conclusions concerning the effects of grain size on the shear strength of soils (Baladi and Wu, 1988).

### 2.2.2 Vibratory compaction tests for RFM

For granular materials, relative density  $D_r$  is always used for evaluating the state of compactness, which is defined by:

$$D_r = \left( \frac{e_{max} - e}{e_{max} - e_{min}} \right) \times 100\% \quad (\text{II .2})$$

where  $e$  is actual void ratio,  $e_{max}$  is the void ratio in the loosest condition, and  $e_{min}$  is the void ratio in the densest condition.

Because of the cohesionless of granular materials (Drnevich et al., 2007), particles simply displace under each hammer drop in impact compaction tests and then rearrange with each successive impact (Pike, 1972; Feng and Vitton, 1999). The application of confinement is needed to get a effective compaction. As the vibration is the most efficient way to provide for reorientation of particles into dense packing (White et al., 1999), vibratory tests have been developed in order to effectively compact granular soils. Two vibratory methods are generally used in the laboratory: vibrating table tests and vibrating hammer compaction tests.

**2.2.2.1 Vibrating table tests** In order to guarantee the granular particles in the loosest state the minimum dry unit weight (or  $e_{max}$ ) is determined by depositing the soil carefully in a given container (ASTM, 2016b; CS, 2006). On the other hand, to obtain the maximum dry unit weight (or  $e_{min}$ ), a soil-filled mold is fastened by a vertically vibrating table, while a surcharge is applied on the surface of the soil (ASTM, 2016a; CS, 2006). The mold is vibrated for a given amount of time, which depends on the frequency of vibrations. The compaction states of studied materials in vibrating table tests vary with the type of soil, water content, time of compaction, amplitude of vibration, surcharge, and mold size, etc...

However, some difficulties exist in the vibrating table tests, such as the failure to maintain calibration, wearing out of parts, sensitivity of electrical fluctuations and different sources of vibration (EM, 1988; ASTM, 2016a), etc... Moreover, the vibrating tables are usually expensive and non-portable. As a result, the vibrating table tests are not popularly used in the laboratory and the vibrating hammer compaction tests are proposed later (Drnevich et al., 2007).

**2.2.2.2 Vibrating hammer compaction tests** The typical vibrating hammer compaction tests apparatus usually includes a cylindrical mold and a vibrating hammer (Pike, 1972; Forssblad, 1981; Parsons et al., 1992; Head et al., 2006; Prochaska and Drnevich, 2005). The tamper foot of vibrating hammer always has the same diameter as the inner one of mold (ASTM, 2020b). The maximum dry unit weight can be determined by vibrating the soil in the mold with the vibrating hammer.

The compaction mechanism of vibrating hammer is identical to that of vibrating table tests: the soil is compacted by applying a fixed nominal pressure and vertical vibrations. As a vibrating table is capable of simultaneously applying a static pressure on the top of soil and vibrating the sample from the bottom, the compaction mechanism of vibrating hammer is more representative of field compaction than the vibrating table (Drnevich et al., 2007, pg. 28).

### 2.2.3 Study the influence of particle size on the density of rockfill materials

As rockfill materials are generally obtained from rock quarry or river bed, a wide range of particle sizes is observed. Hence, large-scale impact compaction tests (Holtz and Lowitz, 1958; Hsu and Saxena, 1991; Yi et al., 2015; Yang et al., 2018) have been developed. The advantage of this approach is that the gradation of test samples is very close to the prototype. Unfortunately, more compactive efforts are needed to guarantee the work on the soils in large-scale tests. As the large molds provide more test space, more handling difficulties exist during the tests (Walsh et al., 1997). Therefore, the vibratory compaction tests with conventional sizes (called small-scale tests) are largely used in the literature. Anyhow, the large-scale compaction test can be used to verify the results obtained by small-scale tests.

In the small-scale tests, the maximum particle size is defined for the preparation of the tested sample (Walsh et al., 1997). As a result, large particles in RFM should be scaled down by using the scaling techniques. The in-situ prototype gradation will be modified to the scaled one for laboratory tests. The experimental results of laboratory tests are then calibrated to predict the in-situ characteristics of RFM (Walker and Holtz, 1953; Hsu and Saxena, 1991; Omar et al., 2003; Ham et al., 2010). However, when the gravel contents exceed 40%, the dry densities of RFM are significantly overestimated (Ham et al., 2010).

In order to avoid this overestimation, Pike (1972) proposed that the density of well graded granular materials was usually higher than a poorly graded one. In general, when the shape of modelled gradation curve is similar to the prototype, the density of RFM tends to increase with the increase of the maximum particle size (Tombs, 1969, pg. 149;

Charles, 1973, pg. 171; Selig and Roner, 1987; Verdugo and de la Hoz, 2007; Kh and Mirghasemi, 2009; Stoeber, 2012, pg. 142). As aforementioned, the densities of packing and the shear strength of graded aggregates are inter-dependent (Maqbool and Koseki, 2010). As the strength index measured in laboratory tests will be applicable to the field situation, the density of tested samples should be identical/close to the in-situ density. As a result, the compaction test is very important in the identification of RFM properties.

## 2.3 Laboratory shear test

### 2.3.1 General introduction to laboratory shear tests

The shear strength of soil systems is usually expressed by the Coulomb equation:

$$\tau_f = \sigma \tan \varphi + c \quad (\text{II .3})$$

where  $\tau_f$  = shear strength,  $\sigma$  = normal stress on the shear plane,  $\varphi$  = angle of internal friction, and  $c$  = cohesion. Shear strength parameters  $\varphi$  and  $c$  can be determined in the laboratory or in the field, as mentioned in section 1. In the laboratory, the direct shear and triaxial tests are largely used.

### 2.3.2 Study the influence of particle size in shear tests

In laboratory, the sample size is described by the sample-size ratio (SSR), which is equal to the ratio of the specimen diameter to the maximum particle size  $d_M$  (Holtz and Gibbs, 1956; Marachi, 1969; Stoeber, 2012). Holtz and Gibbs (1956), and Leslie (1969) indicated that if the specimen was sufficiently larger than the maximum particle size, the strength of RFM was independent on the size of the maximum particle. Marachi (1969) concluded that if the proportion of maximum size particles was 30% or less, the test results were independent on the specimen when the sample-size ratio was equal to 6.

For direct shear tests, Lewis (1955) showed that the width of the shear box must be at least  $30 \sim 40$  times greater than  $d_M$ . Jewell & Wroth (1987) recommended an SSR of  $50 \sim 300$  to reduce the boundary effect. Rathee (1981) adopted a  $300 \text{ mm} \times 300 \text{ mm}$  shear box for granular soils, and concluded that no particle size effect on the shear strength was observed when SSR was in the range of  $10 \sim 12$ . Cerato & Lutenegger (2006) tested five different sands with three different sizes of shear boxes, and proposed that the internal friction angle could be determined with an SSR of 50 or greater.

For uniaxial compression tests, Fumagalli (1969) recommended the SSR of 5 or greater for the well graded soils, and a value much greater (probably in the order of 20) for

uniformly graded soils. Table II .1 gives the sizes of laboratory specimens used in Britain, China, and US. The standards in these countries suggest that an SSR of  $5 \sim 6$  for granular materials used in triaxial tests.

**Table II .1:** Specimen size used in laboratory tests

Country <sup>a</sup>	Compaction test			Direct shear test			Triaxial test <sup>b</sup>		
	Diameter (mm)	Height (mm)	SSR	Diameter (mm)	Height (mm)	SSR	Diameter (mm)	Height (mm)	SSR
Britain*	150	No data	4	305	150	15	150	300	5
China**	300	340	5	300	300	$8 \sim 12$	$200 \sim 500$	$(2 \sim 2.5)D$	5
US***	279	231	No data	600	410	10	150	$(2 \sim 2.5)D$	6

<sup>a</sup> \*after [Institution, 1990](#), pg. 7; [Head et al., 2006](#); [Head et al., 2011](#); \*\*after [CS, 1999](#); [CS, 2006](#); \*\*\*after [Drnevich et al., 2007](#); [Kim, 2007](#); [Fox, 2011](#); [ASTM, 2011](#); [ASTM, 2020a](#).

<sup>b</sup>  $D$  = diameter of specimen

On the other hand, some super large-scale triaxial devices were also developed despite the difficulties in preparing, compacting and sealing a large size specimen. Table II .2 summarizes some super large-scale triaxial devices developed in the past decades. The specimen diameter varies from 914 mm to 1200 mm, with a maximum size of particle  $d_M$  up to 300 mm. The tested gradation is close to the prototype. However, due to the huge cost in testing and maintaining the apparatus, the super large-scale triaxial device is still rarely used in the world. At present, only the super large-scale devices in Japan, France and China are still in use ([Kong et al., 2019](#)).

**Table II .2:** Super large-scale triaxial test device

Location	Country	Maximum confining pressure (MPa)	Specimen diameter (mm)	Specimen height (mm)	Maximum particle size (mm)	SSR	Source
University of Mexico	Mexico	2.45	1130	2500	203	5.6	Marsal ( <a href="#">1967</a> )
University of California, Berkeley	US	5.17	914	2286	152	6.0	Marachi ( <a href="#">1969</a> )
Fujita Corporation	Japan	2.45	1200	2400	300	4.0	Fukushima & Kitajima ( <a href="#">1998</a> )
École Centrale Nantes/University of Nantes	France	1.00	1000	1500	160	6.3	Hu et al. ( <a href="#">2011</a> )
Dalian University of Technology	China	3.00	1000	2000	200	5.0	Kong et al. ( <a href="#">2019</a> )

The particle size effect on the mechanical behaviour of granular materials has been

widely studied: the denser the soil, the higher its dilatancy; the higher the degree of interlocking, the higher the angle of interlocking (Baladi and Wu, 1988). The studied granular materials include sand, sand-gravel mixtures, and coarse-grain soil. However, the obtained results is not consistent with each other. Concerning the effects of grain size on the properties of cohesionless soils, conflicting findings and opinions are summarized as following.

1. No pronounced particle size effects on shear strength (Bishop, 1948; Vallerga et al., 1957; Selig and Roner, 1987; Indraratna et al., 1993; Sharma et al., 1994; Verdugo and de la Hoz, 2007; Hu et al., 2011).

2. The shear strength decreases as the maximum particle size increases (Zeller and Wullimann, 1957; Leslie, 1963; Marsal, 1967; Marachi, 1969; Baladi and Wu, 1988; Stoeber, 2012; Nguyen et al., 2016).

3. The shear strength increases as the maximum particle size increases (Holtz and Gibbs, 1956; Lewis et al., 1955; Tombs, 1969; Charles, 1973; Donaghe and Torrey III, 1985; Baladi and Wu, 1988; Fakhimi et al., 2008; Salimi et al., 2008; Tabibnejad et al., 2015).

4. The shear strength decreases with the increase of the maximum particle size for the quarried RFM, while it increases with increasing the maximum particle size for alluvial RFM (Varadarajan et al., 2006, 2003; Vasistha et al., 2013; Honkanadavar and Sharma, 2016).

The divergence in the experimental observations is due to the adopted compaction method/state (Baladi and Wu, 1988), the particle shape and the sample dimension, etc...Tables II .3 and II .4 summarize the particle size effects on the properties of granular materials. For instance, with a constant relative density, shear strength of granular materials increases with the increase of the maximum particle size  $d_M$ . On the contrary, with a constant void ratio, it is observed that the shear strength diminishes with the increase of  $d_M$ .

**Table II .3:** Summary of the effects of grain size on cohesionless soil

Source	Test type <sup>a</sup>	Particle shape	$d_M$ (mm)	Scaling technique	Uniformity of the test material	SSR	Compaction standard <sup>b</sup>	Conclusion on shear strength <sup>c</sup>	Conclusion on tangent modulus <sup>c</sup>
Bishop (1948)	D	No data	31.8	No data	Uniformly graded	9.6 ~ 521.9	$n$	1	No data
Holtz & Gibbs (1956)	T	Angular/rounded	76.2	No data	Varied	No data	$D_r$	3	No data
Lewis (1955)	D	Angular	6.4	No data	Uniformly graded	No data	$D_r$	3	No data
Vallerga et al. (1957)	T	Sub-rounded/angular	4.8	No data	Uniformly graded	15.0 ~ 474.1	$e$	1	No data
Zeller & Wullimann (1957)	T	No data	100.0	Scalping	Well graded	5.0	$n$	2	No data
Leslie (1963)	T	Sub-rounded	76.2	Parallel	Well graded	No data	$e$	2	No data
Marasali (1967)	T	Angular/rounded	203.2	No data	Well graded	5.6	$n$	2	No data
Marachi (1969)	T	Angular/rounded	152.4	Parallel	Well graded	6.0	$e$	2	2
Tombs (1969)	T	Angular	76.2	Parallel	Well graded	4.0	$D_r$	3	1
Charles (1973)	T	Angular	76.0	Parallel	Well graded	3.9 ~ 10.5	$D_r$	3	No data
Donaghe & Torrey (1985)	T	No data	76.2	Replacement	Well graded	5.0	$D_r$	3	No data
Selig & Roner (1987)	T	Angular	38.1	Parallel	Varied	5.3 ~ 10.6	$e$	1	No data
Baladi & Wu (1988)	T	Rounded sub-rounded	9.7	Parallel	Well graded	7.8 ~ 152.0	$D_r$	3	No data
Baladi & Wu (1988)	T	Rounded/sub-rounded	9.7	Parallel	Well graded	7.8 ~ 152.0	$e$	2	No data
Indraratna et al. (1993)	T	Angular	38.0	Parallel	Well graded	7.9 ~ 12.0	$n$	1	1
Sharma et al. (1994)	T	No data	80.0	Parallel	Well graded	4.8 ~ 15.2	$D_r$	1	3
Varadarajan et al. (2003, 2006)	T	Angular/rounded	80.0	Parallel	Well graded	4.8 ~ 15.2	$D_r$	4	4
Verdugo & de la Hoz (2007)	T	Angular/rounded	30.0	Parallel	Varied	5.0	$D_r$	1	1
Fakhimi & Hosseinpour (2008)	D	Rounded	19.0	Scalping	Well graded	3.2 ~ 9.1	$e$	3	1

**Table II .4:** Summary of the effects of grain size on cohesionless soil (continued)

Source	Test type <sup>a</sup>	Particle shape	$d_M$ (mm)	Scaling technique	Uniformity of the test material	SSR	Compaction standard <sup>b</sup>	Conclusion on shear strength <sup>c</sup>	Conclusion on tangent modulus <sup>c</sup>
Salimi et al. (2008)	D	Angular/rounded	25.0	No data	No data	3.0	$D_r$	3	1
Hu et al. (2011)	T	Sub-angular	160.0	Parallel	Uniformly graded	5.6 ~ 6.25	$e$	1	1
Stober (2012)	T	Angular	25.0	Parallel	Well graded	6.0	$D_r$	2	2
Vasistha et al. (2013)	T	Angular/rounded	5.6	Parallel	Well graded	8.9 ~ 42.3	$D_r$	4	No data
Tabibnejad et al. (2015)	T	Sub-rounded sub-angular	150.0	Replacement	Varied	5.3 ~ 10.5	$e$	3	1
Honkanadavar & Sharma (2016)	T	Angular rounded	80.0	Parallel	Well graded	4.8 ~ 80.2	$D_r$	4	No data
Nguyen et al. (2016)	T	Angular	19.0	Replacement	Well graded	5.3 ~ 7.9	$D_r$	2	2

<sup>a</sup>  $D$  = direct shear test,  $T$  = triaxial test<sup>b</sup>  $n$  = porosity,  $D_r$  = relative density,  $e$  = void ratio<sup>c</sup> 1 = no particle size effect, 2 = strength/tangent modulus diminishes with the increase of  $d_M$ , 3 = strength/tangent modulus increases with the increase of  $d_M$ , 4 = strength/tangent diminishes with the increase of  $d_M$  for quarried RFM but increases with the increase of  $d_M$  for alluvial RFM

### 3 Numerical analysis

#### 3.1 General introduction of DEM model

As an alternative to the continuum modelling, the discrete element method (DEM), also called the distinct element method, directly simulates the interactions between thousands of spherical particles by using physical, well-understood parameters such as particle size, stiffness, and coefficient of friction. DEM has been widely accepted as an effective method to analyse engineering problems in granular and discontinuous materials, especially in granular flows, powder mechanics, rock mechanics and comminution (Weerasekara et al., 2013). As the discrete element method is computationally intensive, the duration of numerical simulation or the number of particles are limited.

The numerical techniques adopted in DEM can be generally divided into two categories (Duran, 2000; Zhu et al., 2007; Luding, 2008; Berger and Hrenya, 2014): hard sphere approach and soft sphere approach. In the hard sphere approach, no interpenetra-

tion or deformation of spheres are taken into account in the numerical simulation. The instantaneous collisions are processed by sequence. As the contact forces between particles are not explicitly considered, the hard sphere method is more suitable to solve the rapid granular flows. Inversely, the soft sphere method allows the deformations (overlaps) between contacting particles. Moreover, the deformations are used to calculate elastic, plastic, and frictional forces between particles while the motion of particles is described by the Newton's laws. The key feature of soft sphere method is capable of handling multiple particle contacts. Therefore, the soft sphere approach will be adopted in the present work.

### 3.1.1 Numerical implementation

The soft sphere approach was firstly used by Cundall & Strack (1979). By using an explicit finite-difference scheme, the DEM calculation alternates between the application of the Newton's second law on particles and a force-displacement law at the contacts. The Newton's second law is used to determine the motion of each particle resulted from the contact and body forces acting upon it, while the force-displacement law is used to update the contact forces arising from the relative motion at each contact (Sitharam and Nimbkar, 2000). The different steps involved in DEM simulations are shown in Fig. II .3. The initial step is to input the system geometry, material property, system state and boundary conditions. After that, with setting the loop, the simulation progresses as a transient or dynamic analysis during a specified number of time increments. The contacting particles are identified at each time step. The contact forces at the contact points are then calculated based on the given constitutive laws (contact models). The transitional and rotational accelerations of the particles can be calculated by solving the dynamic equilibrium equations. The displacement and rotation of the particle over the current timestep are then determined by the leapfrog scheme. Finally, the particle position and orientation can be updated with these incremental displacement and rotation. This simulation loop will be repeated at the next time step when some conditions are met.

### 3.1.2 Governing equations

By using a Lagrangian method, all particles in DEM are tracked by explicitly solving their trajectories (Kloss et al., 2012). The force balance for the particle with index  $i$  is given by



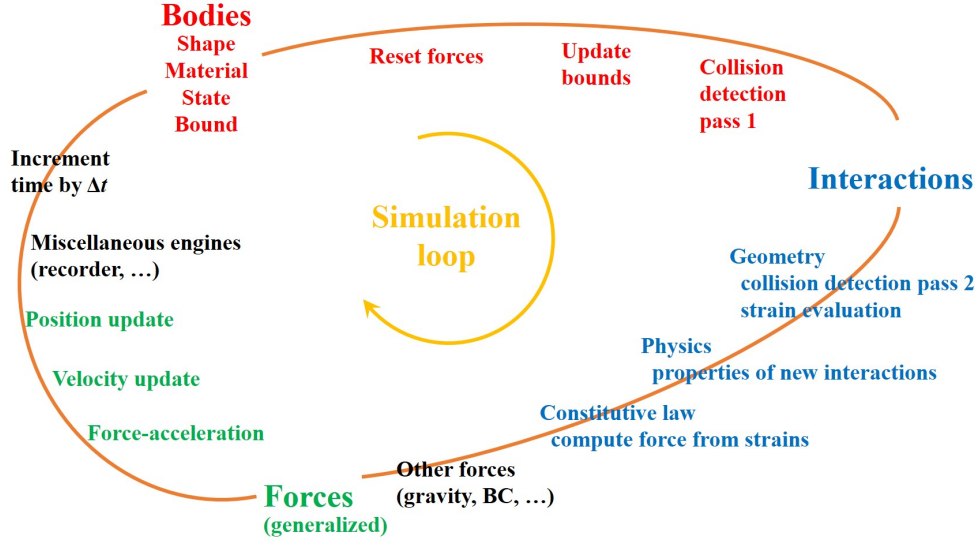


**Figure II .3:** Typical simulation loop in DEM; each step begins at body-centered bit at 11 o'clock, continues with interaction bit, force application bit, miscellanea and ends with time update (after [Smilauer et al., 2020](#))

$$\begin{aligned}
 m_i \ddot{u}_i &= F_{i,n} + F_{i,t} + F_{i,f} + F_{i,b} \\
 I_i \frac{dw_i}{dt} &= \sum M_i
 \end{aligned}
 \tag{II .4}$$

where  $F_{i,n}$  = the normal contact force,  $F_{i,t}$  = the tangential contact force,  $F_{i,f}$  = the force may be exerted by the surrounding fluid phase, which will not be discussed in this research,  $F_{i,b}$  = other body forces like gravity.  $\sum M_i$  = the total moment applied on the particle. The translational and rotational acceleration  $\ddot{u}_i$  and  $\dot{w}_i$  can be calculated from the above two equations. By using the integration with time step, the incremental displacement and rotation can be obtained and then used to update the particle positions.

### 3.1.3 Contact models

The contacts of particle-particle or of particle-boundary will mutually affect each other. The stress-strain, or force-displacement relationship of granular materials can be described by using contact models (Fig. II .4). Several commonly used contact models are briefly introduced below ([O'Sullivan, 2011](#); [Otsubo, 2016](#); [Teixeira, 2009](#); [Zhao, 2019](#)).

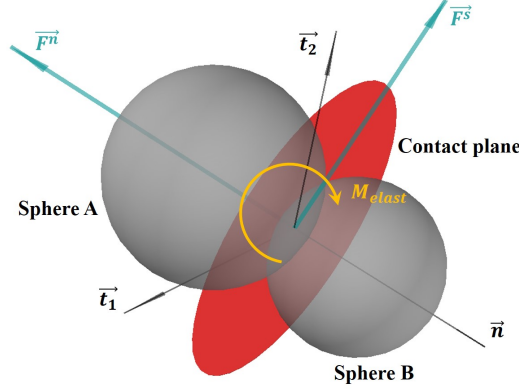


**Figure II .4:** Interaction between two spherical discrete elements with its normal  $\vec{F}^n$ , shear  $\vec{F}^s$  and moment  $M_{elast}$  components (after [Kozicki and Donze, 2008](#))

**3.1.3.1 Normal contact models** The normal component of the elastic contact force  $\vec{F}^n$  can be obtained from the spring model. In this model, it is assumed that the elastic force is proportional to the penetration (overlap)  $u^n$  between two elements (particle-particle, particle-boundary).

$$\vec{F}^n = k^n u^n \vec{n} \quad (\text{II .5})$$

where  $\vec{n}$  is the normal contact vector,  $k^n$  is the normal contact stiffness.

- **Linear spring model (Hooke's law)** is the simplest contact model, in which  $k^n$  is constant and depends on the properties of material. The stiffness is given by

$$k^n = \frac{k_1^n k_2^n}{k_1^n + k_2^n} \quad (\text{II .6})$$

where  $k_1^n, k_2^n$  are the normal contact stiffnesses for two elements in contact.

- **Hertz nonlinear spring model** is based on the theoretical analysis of the deformation of smooth, elastic sphere in frictional contact. According to the Hertzian contact theory, the stiffness can be given by

$$\begin{aligned} k^n &= \frac{4}{3} E \sqrt{r} \\ E &= \left( \frac{1 - \nu_1^2}{E_1} + \frac{1 - \nu_2^2}{E_2} \right)^{-1} \\ r &= \left( \frac{1}{r_1} + \frac{1}{r_2} \right)^{-1} \end{aligned} \quad (\text{II .7})$$

where  $E_1, E_2, \nu_1, \nu_2, r_1, r_2$  are respectively Young's moduli, Poisson's ratios and radii of the two elements in contact.

- **Normal viscous damping** can be added for further energy dissipation in a contact model. The viscous damping normal force can be computed from

$$\begin{aligned} \vec{F}_d^n &= C_n \vec{\delta}_n \\ \vec{\delta}_n &= ((\vec{v}_1 - \vec{v}_2) \cdot \vec{n}) \cdot \vec{n} \end{aligned} \quad (\text{II .8})$$

where  $\vec{\delta}_n$  is the normal component of the relative velocity between two elements in contact. The normal damping coefficient  $C_n$  can be evaluated from the critical damping coefficient  $C_{cr}$  (Thornton, 2015)

$$C_n = \beta_n C_{cr} = 2\beta_n \sqrt{\frac{m_1 m_2 k^n}{m_1 + m_2}} \quad (\text{II .9})$$

where  $\beta_n$  is the normal critical damping ratio,  $m_1$  and  $m_2$  are the masses of two contacting elements.

**3.1.3.2 Tangential contact models** Like the normal contact force, the tangential (shear) elastic contact force increment  $\Delta \vec{F}_s$  can also be assumed to be proportional to the incremental tangential displacement  $\Delta \vec{u}_s$ . The shear force  $\vec{F}_s$  is then obtained by summing up the increments  $\Delta \vec{F}_s$ .

$$\begin{aligned} \Delta \vec{F}_s &= -k^s \Delta \vec{u}_s \\ \vec{F}_s &= \sum \Delta \vec{F}_s \end{aligned} \quad (\text{II .10})$$

where  $k^s$  is the tangential contact stiffness.

To produce the behaviour of non-cohesive geomaterials, a Mohr-Coulomb criterion is used

$$\begin{aligned} |\vec{F}^s| &\leq \mu |\vec{F}^n| \\ \mu &= \min(\mu_1, \mu_2) \end{aligned} \quad (\text{II .11})$$

where  $\mu_1$  and  $\mu_2$  are the friction coefficients of two contacting elements.

- **Linear tangential model** assumes the tangential contact stiffness is constant and can be obtained by

$$k^s = \frac{k_1^s k_2^s}{k_1^s + k_2^s} \quad (\text{II .12})$$

where  $k_1^s$ ,  $k_2^s$  are the tangential contact stiffnesses for two elements in contact.

- **Mindlin-Deresiewicz tangential model** (Mindlin, 1953) indicates that tangential

contact stiffness should depend on the current normal and tangential forces, the loading history, etc. The tangential stiffness under the loading condition can be given by

$$\begin{aligned} k^s &= \frac{dF^s}{du^s} = 8Ga(1 - \frac{F^s}{\mu F^n})^{\frac{1}{3}} \\ G &= (\frac{2-\nu_1}{G_1} + \frac{2-\nu_2}{G_2})^{-1} \\ a &= \sqrt{ru^n} \end{aligned} \quad (\text{II .13})$$

where  $G_1, G_2$  are shear moduli of the two elements in contact,  $a$  is the radius of the circular contact area.

- **Shear viscous damping** is like the normal one, and the calculation can be obtained by

$$\begin{aligned} \vec{F}_d^s &= C_s \vec{\delta}_s \\ C_s &= \beta_s C_{cr} = 2\beta_s \sqrt{\frac{m_1 m_2 k^s}{m_1 + m_2}} \end{aligned} \quad (\text{II .14})$$

where  $C_s$  is the tangential damping coefficient,  $\vec{\delta}_s$  is the tangential component of the relative velocity,  $\beta_s$  is the shear critical damping ratio.

The linear contact model is commonly used due to its ease of implementation. However, the non-linearity can not be captured from two interacting elastic spheres. Moreover, in the case of particles with various sizes, the non-linearity needs to be scaled with respect to the material elastic modulus (Yan and Dong, 2011; de Bono, 2013, pg. 103). Although the Hertz-Mindlin contact model is only applicable to spheres and is more computationally demanding than the linear model, it is closer to the realistic behaviour of material. In addition, the variation of contact stiffness with particle sizes is also taken into account in the Hertz-Mindlin contact model to describe the non-linear stiffness of two interacting spheres (Yan and Dong, 2011; de Bono, 2013, pg. 104).

**3.1.3.3 Rolling resistance models** Particle rotation plays an important role on the deformation micro-mechanism of granular materials (Ni et al., 2000; Cheng and Minh, 2009). Assuming spherical particles, a rolling resistance can be added to describe the roughness of grains. The moment resulted from the rolling resistance model is different from the moments provided by the parallel bonds, in which it is assumed that the particles are cemented (Zhao, 2019)

- **Iwashita-Oda model** (Iwashita and Oda, 1998) is firstly proposed to simulate the microstructure of shear band, considering the effect of rolling resistance at contacts in 2D. An additional set composed of an elastic spring, a dash pot, a non-tension joint, and a slider are installed at each contact. When particles rotates with each other, the moment transferred by this model can be given by

$$M^r = -k^r \theta^r - C_r \frac{d\theta^r}{dt} \quad (\text{II .15})$$

where  $k^r$  is the rolling stiffness,  $\theta^r$  is the relative rotation,  $C_r$  is the rotational viscous damping. The limiting value of  $M^r$  is given by  $\eta F^n$ , where  $\eta$  is the coefficient of rolling friction. In YADE, the Iwashita-Oda model has been implemented in 3D form by Belheine et al (2009).

- **Jiang model** (Jiang et al., 2009, 2005) is proposed based on the Iwashita-Oda model (Iwashita and Oda, 1998, 2000), in which the shape parameter  $\delta$  is introduced to reflect the effect of particle shape and the angle of internal friction. The contact width  $B$  is then given by  $B = \delta \cdot r$ . The grain contact is continuously distributed with normal/tangential basic element (BE). In the BE, the rolling contact is characterized by the stiffness parameter  $K_m$ , which is dependent on  $k^n$ , the shape parameter  $\delta$  and the common radius  $r$ . The resultant normal force  $F^n$  is given by

$$F^n = \int_{-B/2}^{B/2} [k^n(u^n + \theta^r z) + C_n(\dot{\theta}^r z + \dot{u}^n)] dz \quad (\text{II .16})$$

where  $z$  is the length of the BE. The resultant couple moment  $M$  by the continuously distributed normal BE is expressed as

$$M = \int_{-B/2}^{B/2} [k^n(u^n + \theta^r z) + C_n(\dot{\theta}^r z + \dot{u}^n)] z dz \quad (\text{II .17})$$

Jiang et al. (2009) improved the previous model by introducing the second parameter  $N$ , which is related to the roughness of the contact. Unfortunately, Jiang model is only available in 2D conditions.

**3.1.3.4 Bond models** The particles can be bonded in DEM by introducing a tensile and shear strength in the normal and tangential direction. Once the bond is formed at a contact, it will continue to exist until the bond is broken.

- **Linear bond model** (McDowell and Harireche, 2002) can be envisaged as a pair of

spring with constant normal and shear stiffnesses acting at the contact point. The two springs have specified tensile and shear strengths. The contact bond breaks when contact force exceed the tensile or shear strengths. It should be noted that in the linear bond model, the bond is still in an infinitesimal point and the contact plane cannot resist relative rotation. As a result, the bonded particles cannot slip but they can roll over each other when no rolling resistance or no moment exists.

- **Parallel bond model** (Potyondy and Cundall, 2004) can be envisioned as a set of elastic springs uniformly distributed over a rectangular cross section in 2D and a circular cross section in 3D lying on the contact plane and centred at the contact point. Different from the linear bond model, both force and moment can be transmitted in the parallel bonds. The total force  $\bar{F}_i$  and moment  $\bar{M}_i$  carried by the parallel bond can be resolved into normal and shear components with respect to the contact plane:

$$\begin{aligned}\bar{F}_i &= \bar{F}^n n_i + \bar{F}^s t_i \\ \bar{M}_i &= \bar{M}^n n_i + \bar{M}^s t_i\end{aligned}\tag{II .18}$$

where  $\bar{F}^n$ ,  $\bar{F}^s$  and  $\bar{M}^n$ ,  $\bar{M}^s$  denote the axial and shear directed forces and moments, respectively, and  $n_i$  and  $t_i$  are the unit vectors that define the contact plane. The incremental force and moment are given by

$$\begin{aligned}\Delta \bar{F}^n &= \bar{k}^n A \Delta u^n \\ \Delta \bar{F}^s &= -\bar{k}^s A \Delta u^s \\ \Delta \bar{M}^n &= -\bar{k}^s J \Delta \theta^n \\ \Delta \bar{M}^s &= -\bar{k}^n I \Delta \theta^s\end{aligned}\tag{II .19}$$

where  $A$ ,  $I$ ,  $J$  are the area, moment of inertia and polar moment of inertia of the parallel bond cross section,  $\bar{k}^n$  and  $\bar{k}^s$  are respectively the normal and shear stiffness

per unit area of the parallel bond. The parameters  $A$ ,  $I$ ,  $J$  are given by

$$\begin{aligned} A &= \begin{cases} 2\bar{R}t, t = 1 & 2D \\ \pi\bar{R}^2, & 3D \end{cases} \\ I &= \begin{cases} \frac{2}{3}\bar{R}^3t, t = 1 & 2D \\ \frac{1}{4}\pi\bar{R}^4, & 3D \end{cases} \\ J &= \begin{cases} 0 & 2D \\ \frac{1}{2}\pi\bar{R}^4, & 3D \end{cases} \end{aligned} \quad (\text{II .20})$$

where  $\bar{R}$  is parallel bond radius. The radius of parallel bond circular can be defined as

$$\bar{R} = \bar{\lambda} \min(r_1, r_2) \quad (\text{II .21})$$

where  $\lambda$  is the bond radius multiplier.

### 3.1.4 Particle packing

The response of granular materials is sensitive to the particle packing (material fabric), i.e., the topology of the material inner structure (Boutt and McPherson, 2002; Sakaguchi and Murakami, 2002; de Bono, 2013). For a deep understanding of the complex behaviour of granular materials, it is necessary to define the internal structure and describe its evolution during deformation (Thornton and Barnes, 1986). Fabric can be quantified by using either scalar parameters or directional parameters (Fonseca et al., 2013). The scalar measures of fabric include density and coordination number, etc... On the other hand, directional fabric can be measured by force chain network, fabric tensor (the contact normal orientation, the particle orientation, branch vector), polar histogram, etc... These internal variables are capable of providing the qualitative and quantitative descriptions of macroscopic mechanical behavior of granular materials at the particle scale (Thornton, 2000; O'Sullivan, 2011).

**3.1.4.1 Packing density** The relation between the volume of solids and the volume of voids is a basic measure of fabric. The void ratio  $e$  is defined as the ratio of the volume of voids  $V_v$  to the volume of solids  $V_s$ :

$$e = \frac{V_v}{V_s} \quad (\text{II .22})$$

**3.1.4.2 Coordination number** The coordination number  $CN$  is the number of contacts on one particle. In practice, the average coordination number  $Z$  is used as another scalar metric to quantify the contact density in a particle assembly. The average coordination number is defined as the average number of contacts per particle, and it can be given as

$$Z = 2 \frac{N_c}{N_p} \quad (\text{II .23})$$

where  $N_c$  is the number of contacts in the system; and  $N_p$  is the number of particles. Considering the particles that do not transmit contact forces through the material, Thornton (2000) proposed a mechanical average coordination number:

$$Z_m = \frac{2N_c - N_p^1}{N_p - N_p^0 - N_p^1} \quad (\text{II .24})$$

where  $N_p^0$  and  $N_p^1$  are the number of particles with no or only one contact, respectively.

As the average coordination number  $Z$  is a measure of the packing density, it is related to the specimen void ratio  $e$  (Sitharam et al., 2002; Agnolin and Roux, 2007). Therefore, some researchers (Oda, 1977; Santamarina and Cascante, 1996; Hasan and Alshibli, 2010) have proposed empirical equations to joint the  $Z$  and  $e$ . However, the  $Z$  and  $e$  cannot be related via a simple one-one function (Barreto and O’Sullivan, 2012) because the relationship  $Z$  and  $e$  also depends on the particle geometry, particle size distribution, surface properties, degree of anisotropy in contact orientations, and friction coefficient (Rothenburg and Kruyt, 2004; O’Sullivan, 2011; Barreto and O’Sullivan, 2012).

**3.1.4.3 Contact force distribution** The macroscopic behaviour of granular materials is governed by the micromechanics acting at the particle scale (Zhou, 2011). When subjected to external loadings, the force propagation in granular media can only be achieved via the interparticle contacts to establish a continuous and stable path. However, force propagation can be rather ramified in granular systems, and the contact forces between particles are heterogeneously distributed within the granular assembly (Antony et al., 2015; Hurley et al., 2016). Extensive experimental and theoretical effort has been devoted to the study of force network in dense granular materials, suggesting that forces in particle assembly are transmitted along chainlike particle groups referred to as “force chains”.

The concept of “force chains” comes from photoelastic tests (Drescher and De Jong, 1972; Oda et al., 1982; Behringer et al., 1999; Geng et al., 2003; Antony et al., 2015), in which the force chains can be visualized through stress-induced birefringence within assemblies of photoelastic disks. It has been seen that: (1) The minority of particles



carry the majority of loading and form a “strong network”; (2) The number of particles in strong network decreases exponentially with increasing contact force magnitude (Radjai et al., 1996, 1998; Thornton and Antony, 2000; Peters et al., 2005; Antony et al., 2015; Hurley et al., 2016).

Despite the numerous investigations on force chains, no generally acceptable parameters can be used to quantify the distribution of them (Peters et al., 2005; Muthuswamy and Tordesillas, 2006). The force chains is commonly analysed via a line diagram with, in which their thickness or color of represents the magnitude of the contact forces.

### 3.1.5 DEM codes

Since the first DEM program BALL developed by Cundall & Strack (1979), various DEM codes have emerged in the last few decades. Some of them have been launched as commercial software. The wide usage of DEM and the development of DEM codes are commensurate with the advance in computational power (Cundall, 2001; Hanley et al., 2011).

#### 3.1.5.1 Commercial software

- **PFC 2D & PFC 3D** (Particle Flow Code in 2 dimensions and 3 dimensions) are the most prevalent codes to date (Itasca, 2015). Since the release of the first version in 1994, PFC has been successfully used in many academic institutions and private companies around the world. The research works focus on the behaviour of soil and rock at the laboratory scale and different types of engineering projects, for instance: slope stability and rockfall hazard mitigation, hydraulic fracturing and soil-tool interactions, etc... The FISH scripting and Python scripting languages enable the users to access monitor, and control nearly every model and solution parameter. Besides, the users can also add their own contact models by C++ Plug-in.
- **UDEC & 3DEC** (Universal Discrete Element Code in 2 dimensions and 3 dimensions) simulate the response of discontinuous media (such as jointed rock mass) subjected to either static or dynamic loading (Itasca, 2007). The discontinuous medium is represented as an assemblage of discrete blocks. Individual blocks behave as either rigid or deformable material. Deformable blocks are subdivided into a mesh of finite difference elements, and each element responds according to a prescribed linear or nonlinear stress-strain law. By a Lagrangian calculation scheme, 3DEC is well-suited to model the large movements and deformations of a blocky system.

- **EDEM** can form an accurate representation of particle shape by importing CAD models of real particles ([Solutions, 2010](#)). EDEM can be extended to simulate particle-particle, particle-fluid, particle-structure using external models by using user defined libraries programmed in C++.

### 3.1.5.2 Open-source and non-commercial packages

- **YADE** (Yet Another Dynamic Engine) can handle various different numerical models (Discrete Element Method, Lattice Geometrical Model, Finite Element Method, etc.) within a single package, which makes it as a common research platform and allows the model coupling ([Kozicki and Donze, 2008, 2009](#)). Moreover, the visualization and input/output methods have already been developed, indicating that the researchers can focus strictly on the formulas. Its computation parts are written in C++, allowing independent implementation of new algorithms and interfaces. Python can also be used for rapid and concise scene construction, simulation control, post-processing and debugging.
- **BALL & TRUBAL** are 2D and 3D DEM codes developed by Cundall ([1988; 1971](#)) in Fortran, and now they are maintained by Thornton ([2000; 2015](#)).
- **LIGGGHTS** (LAMMPS Improved for General Granular and Granular Heat Transfer Simulations) ([Kloss and Goniva, 2011; Kloss et al., 2012](#)) is based on LAMMPS (Large-Scale Atomic/Molecular Massively Parallel Simulator), a successful open source Molecular Dynamics code. As LAMMPS, LIGGGHTS runs on single processors or in parallel using message-passing techniques and a spatial-decomposition of the simulation domain.
- **ESys-Particle** ([Weatherley et al., 2014](#)) is designed to develop the parallel supercomputers, clusters or multi-core PCs running a Linux-based operating system. The C++ simulation engine implements spatial domain decomposition via the Message Passing Interface (MPI). A Python wrapper API provides flexibility in the design of numerical models, specification of modelling parameters, etc.

Because the kernel of the commercial code remains a black box for the end-user, a commercial software limits one's ability to improve/modify the existing code-base. The promise of open-source code is better quality, high reliability, more flexibility and low cost, etc... In this thesis, YADE will be used as the main DEM tool to study the particle size effect of RFM.

### 3.2 DEM study of granular materials

In the past two decades, with the rapid development of DEM codes and the improvement of computer performance, granular materials (sand, RFM, etc.) can be investigated in particle scale (Shao et al., 2009). By calibrating the parameters of contact models, the laboratory test can be reproduced by DEM simulations (Zhou et al., 2013; Kong et al., 2019). Anyway, DEM provides a new way to investigate the mechanical behaviour of granular materials.

#### 3.2.1 DEM study of grading effects

Due to the limitation of computational time in DEM, the finer part in a granular material is usually removed (Shao et al., 2020). This deletion will obviously lead to the difference between experimental and numerical results (Kh and Mirghasemi, 2009).

The DEM samples can be prepared with an inter-particle friction coefficient, which varies from 1 and 0. Kong et al. (2000) performed a 3D deposition test with fine and coarse mixtures. The obtained results indicated that with the increase of fine content, the density dropped at the beginning and then increased to a steady value. This density decrease can be explained by using the “particle bridging” theory, in which the fine particles form the bridges to restrain the subsequent motion.

The recent research works performed on the grading effects are summarized in the Table II .5. Different conclusions have been obtained and can be classified in three categories:

1. No pronounced grading effect on the mechanical behaviour of granular materials (Wood and Maeda, 2008),
2. The strength/initial tangent modulus augments with a high compressibility (low dilatancy) when gradation is widened, or content of coarse fraction is high (Sitharam, 2003; Latha and Sitharam, 2008; Cheng and Minh, 2009),
3. The strength/initial tangent modulus decreases with a low compressibility (high dilatancy) when gradation is widened, or content of coarse fraction is high (Sitharam and Nimbkar, 2000; Yan and Dong, 2011; Liu et al., 2013).

The difference among these research works is related to different factors: the used density standard, the particle number (Zhou et al., 2000; Kuhn and Bagi, 2009) and the particle breakage (Latha and Sitharam, 2008; Kh and Mirghasemi, 2009), etc...

**Table II .5:** Summary of the grading effect on granular materials by DEM

Source	test-type <sup>a</sup>	Particle shape	$d_M$ (mm)	Gradation scheme	Particle number	Density Control <sup>b</sup>	Boundary <sup>c</sup>	Strength <sup>d</sup>	Initial tangent moduli <sup>d</sup>	Volumetric strain <sup>d</sup>	Particle breakage
Sitharam & Nimbkar (2000)	B	Disc	110	Keeping same $d_m$	1000	$D_r$	R	2	2	5	No
Sitharam (2003)	B	Disc	50	Well graded /monosized	1000	$e$	R	3	-	-	No
Latha & Sitharam (2008)	T	Sphere	100	Keeping same $d_m/d_M$	1000	$D_r$	P	3	2	-	No
Wood & Maeda (2008)	B	Disc	100	Keeping same $d_M$	4000	$D_r$	R	1	1	1	No
Cheng & Minh (2009)	2D-D	Cluster with 3 discs	No data	Keeping same $d_m, d_M$ but different coarse fraction	192 ~ 382	$e$	R	3	1	4	No
Evans et al. (2009)	B	Clump with 2 discs	15	Well graded /monosized	-	$D_r$	R	1	3	5	No
Yan & Dong (2011)	T	Sphere	6	Well graded /monosized	4500 ~ 10000	$e$	R	2	2	5	No
Liu et al. (2013)	T	Sphere	80	Keeping same $d_M$	2277 ~ 8317	$e$	R	2	2	5	No

<sup>a</sup> B = biaxial loading test, T= triaxial compression test, 2D-D = 2-dimensional direct shear test<sup>b</sup>  $D_r$  = relative density,  $e$  = void ratio<sup>c</sup> R = rigid boundary, P = periodic boundary

<sup>d</sup> 1 = no pronounced effect, 2 = strength/initial tangent modulus diminishes when gradation is widened, or content of coarse fraction is higher, 3 = strength/initial tangent moduli augments when gradation is widened, or content of coarse fraction is higher, 4 = low compressibility and high dilatancy when gradation is widened, or content of coarse fraction is higher, 5 = high compressibility and low dilatancy when gradation is widened, or content of coarse fraction is higher

### 3.2.2 DEM study of particle size effect

Particle breakage is not considered in many numerical simulations of RFM and then induces the difference between experimental and numerical results (Latha and Sitharam, 2008; Kh and Mirghasemi, 2009).

The number of particles used in a DEM simulation should be at least several thousands to obtain a more realistic and stable results (Corriveau et al., 1997; Zhou et al., 2000; Kuhn and Bagi, 2009). Corriveau et al. (1997) recommended that a sufficiently large number of particles should be used in the DEM simulations in order to obtain a proper aggregate behaviour and a good accuracy for the yield stresses. The representative volume element (RVE) (Yan and Dong, 2011; Wang and Arson, 2016) is used in DEM to study the mechanical behavior of granular assemblage. In a RVE, the boundary effect on the sample and the natural inhomogeneity of granular material are considered (Fu and Dekelbab, 2003; Muthuswamy and Tordesillas, 2006; Cheung and O’Sullivan, 2008; Kuhn and Bagi, 2009; Marketos and Bolton, 2010; Wang and Gutierrez, 2010; Scholtès and Donzé, 2013). Wang & Gutierrez (2010) presented that in the 2D DEM model of a direct shear test, a minimum value of 60 for  $L/d_M$ , a minimum value of 40 for  $H/d_M$ , and a range of 1.5 to 2 for  $L/H$  were needed to get satisfactory results.  $L$  and  $H$  were shear box length and height, respectively.

In the DEM simulation, the boundary effect problems can be resolved by using periodic boundaries (Zhang et al., 1997; Cundall, 1988; Kuhn, 1999; Makse et al., 2000; Thornton, 2000; Sitharam et al., 2002; Rothenburg and Kruyt, 2004; Marketos and Bolton, 2010; Ng and Zhou, 2016; Liu et al., 2020), in which a more uniform particle fabric is applied throughout the assembly. In addition, in order to guarantee the high computational efficiency, small numbers of particles are needed to get the representative results. However, if the number of particles included in the periodic cell is too small, the results may not be incapable of representing the general material behaviour (Barreto and O’Sullivan, 2012). Therefore, Kuhn & Bagi (2009) recommended that at least a few thousand particles were required to get a realistic microband patterning. Hence, caution should be taken in the choice of the size of periodic cell. When the periodic simulation results are compared with the laboratory data, more care also should be taken due to the negotiation of the stress homogeneity in periodic cell simulations (Cheung and O’Sullivan, 2008).

According to the influence of particle sizes on the mechanical characteristics of granular materials, a summary of DEM simulations is given in Table II .6. It is noticed that some results are contradictory, especially in the initial tangent moduli and obtained deformation. As mentioned in section 3.2.1, this difference is related to many factors, such as density

standard, particle number, boundary condition, particle shape, particle breakage, etc. Therefore, further DEM simulations are still needed to investigate the influence of particle size effects on the mechanical characteristics of RFM.

**Table II .6:** Summary of particle size effect study on granular materials by DEM

Source	test type <sup>a</sup>	Particle shape	$d_{max}$ (mm)	Scale technique	Particle number	Density Control <sup>b</sup>	Boundary <sup>c</sup>	Strength <sup>d</sup>	Initial tangent modulus <sup>d</sup>	Volumetric strain <sup>d</sup>	Particle breakage	S S R
Ni et al. (2000)	3D-D	Cluster with 2 balls	1.8	Parallel	5000 ~ 50000	$n$	R	1	-	4	No	> 3 3.3
Sitharam & Nimbkar (2000)	B	Disc	150	Parallel	1000	$D_r$	R	1	1	1	No	-
Latha & Sitharam (2008)	T	Sphere	100	Parallel	1000	$D_r$	P	1	2	5	No	-
Latha & Sitharam (2008)	T	Sphere	100	Uniform particle	1000	$D_r$	P	1	2	5	No	-
Kh & Mirghasemi (2009)	2D-D	Ellipse	38	Parallel/scalping	650	$n$	R	3	-	-	No	-
Zhou et al. (2016)	T	Sphere	60	Parallel	4505	$n$	R	1	3	5	Yes	5.0

<sup>a</sup> 3D-D = 3-dimensional direct shear test, B = biaxial compression test, 2D-D = 2-dimensional direct shear test, T = triaxial compression test

<sup>b</sup>  $D_r$  = relative density,  $n$  = porosity

<sup>c</sup> R = rigid boundary, P = periodic boundary

<sup>d</sup> 1 = no pronounced effect, 2 = strength/initial tangent modulus decreases with particle size, 3 = strength/initial tangent moduli increases with particle size, 4 = low compressibility and high dilatancy with particle size, 5 = high compressibility and low dilatancy with particle size

## 4 Particle breakage in RFM

The particle breakage plays a dominant role in the investigation of material properties and mechanical behaviour of RFM (Lade et al., 1996; Deluzarche and Cambou, 2006; Brzesowsky et al., 2011; Kh et al., 2011; Wang and Yan, 2013; Alonso et al., 2012; Stoeber, 2012; de Bono, 2013; Cil and Alshibli, 2012, 2014a; Zhao et al., 2015; Huang et al., 2020), for instance, the volumetric strains (Lee and Farhoomand, 1967; Yamamuro and Lade, 1996; McDowell and Bolton, 1998; Luzzani and MR, 2002). Moreover, some scholars have shown that particle breakage has a strong effect on the internal friction angle (Varadarajan et al., 2003; Coop et al., 2004; Tarantino and Hyde, 2005; Kh et al., 2011) and on the

permeability (Lade et al., 1996). Therefore, the crushing of particle should be considered in the study of particle size effects on the mechanical characteristics of RFM (Marsal, 1969).

## 4.1 Single particle strength

### 4.1.1 Single-particle crushing test

The crushing characteristic of individual particles are required to identify the mechanical behaviour of granular materials (Nakata et al., 1999). Particle strength is defined as the ability to withstand an applied force and energy input up to a certain limit of failure or breakage. Due to the presence of pores, defects such as micro cracks or confined air bubbles and impurities, the strength of particles is not uniform and therefore should be described by a statistical distribution function (Rozenblat et al., 2011).

Under compression, the failure of a spherical granular particle is characterized by a tensile failure (Darvell, 1990; Shipway and Hutchings, 1993; McDowell and Bolton, 1998; Altuhafi and Coop, 2011; Cil and Alshibli, 2012; Cheshomi and Sheshde, 2013). According to Griffith criterion (Griffith, 1920), failure occurs when the stress intensity factor  $K$  reaches the fracture toughness of mode I,  $K_{Ic}$ . Consequently, the ‘tensile strength’ of rock grains can be indirectly measured by diametrical compression between flat platens. In addition, this test can also be used to calibrate DEM modelling of crushable particles (Zhao et al., 2015). The tensile strength also depends on the particle shape (Cheshomi and Sheshde, 2013). However, a big divergence is observed in the obtained values of crushing force even the particle size and shape are very similar and these samples are tested by the same equipment (Singh, 2017).

In view of this, a series of research work (Kalman and Goder, 1998; Subero-Couroyer et al., 2003; Portnikov et al., 2013; Portnikov et al., 2013) has been performed to find a particle number, which is sufficient for the identification of material strength. Sullivan & Lauzon (1986) proposed that less than 20 particles were not recommended for the probability prediction of both numerical simulations and experimental data. Based on the statistics analysis, McDowell (2001) concluded that for a Weibull modulus of 3 or greater, 30 particles are adequate. Therefore, 20 ~ 30 particles are generally used to measure the single particle tensile strength of a given size (Nakata et al., 1999; McDowell and Amon, 2000; McDowell, 2002; McDowell and Humphreys, 2002; Lim, 2004; Lim et al., 2004; Ham et al., 2010; Yoshimoto et al., 2012; Cheshomi and Sheshde, 2013; Huang et al., 2014; Huang et al., 2020).

Based on the research work performed on the Leighton Buzzard sand, oolitic limestone

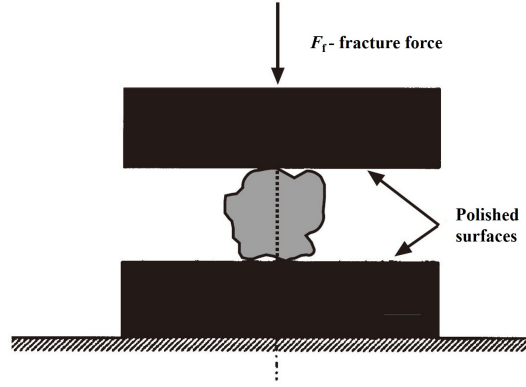


**Figure II .5:** Particle tensile strength test set-up (after Lee, 1992)

and carboniferous limestone, Lee (1992) proposed the tensile strength within the particle, which can be defined as :

$$\sigma_f = \frac{F_f}{d^2} \quad (\text{II .25})$$

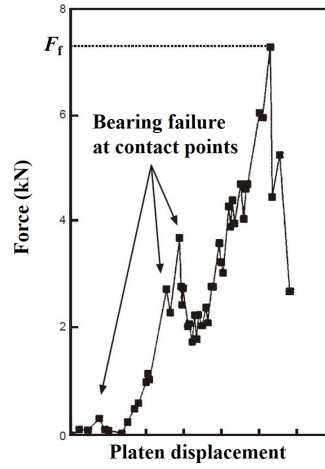
where  $d$  is the diameter of particle (defined as the initial distance between the platens before compression (Jaeger, 1967; Nakata et al., 1999, 2001b; Zhong et al., 2014; de Bono and McDowell, 2016a), or the distance between the platens at failure moment (McDowell and Amon, 2000; McDowell and Humphreys, 2002; Lim, 2004; Lim et al., 2004; Huang et al., 2020)(Fig. II .5). McDowell & Amon (2000) preferred to use the particle size at failure as  $d$ . Inspired by the works of Jaeger (1967) and Shipway & Hutchings (1993),  $F_f$  is the diametrical force. This definition is consistent with the definition of tensile strength of concrete in the Brazilian test.

Fig. II .6 illustrates a typical plot of platen force  $F$  as a function of the platen displacement  $\delta$ . It can be seen that there are some initial peaks (bearing failure at contact points), which correspond to the fracturing of asperities and the rounding of the particle (Ham et al., 2010). The initial small peaks are then followed by a large peak corresponds to the maximum load, combing with a catastrophic failure as the particle is split into two or more major pieces and the loading drops dramatically. By using the Eq. (II .25), Lee (1992) found that for a given size and mineralogy, the tensile strength of particles follows a statistical distribution. Moreover, the average strength was a function of the average particle size  $d$ , as shown in Fig. II .7. The data can be described by the relation

$$\sigma_f \propto d^b \quad (\text{II .26})$$

This relationship can be quantified more rigorously using the Weibull distribution (Weibull,





**Figure II .6:** Typical load-deflection plot (after Lee, 1992)

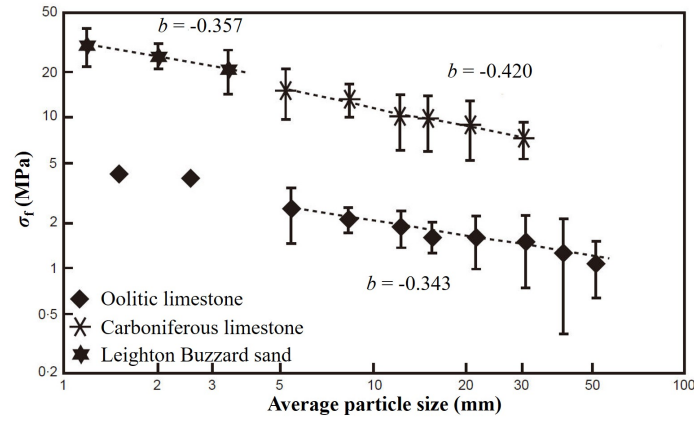


**Figure II .7:** Mean tensile strength as a function of particle size (after Lee, 1992)

1951).

#### 4.1.2 Weibull statistical distribution

Weibull (1951) statistical distribution theory can be used to describe the variations of the strength of brittle materials, e.g. ceramics (Billam, 1972; Sullivan and Lauzon, 1986). Nakata et al. (1999) and McDowell & Amon (2000) confirmed that for sand particles with a given size distribution, the distribution of measured tensile strength followed the Weibull distribution. Lim et al. (2004) showed that the tensile strength of railway ballast also followed the Weibull distribution. Zhao et al. (2015) confirmed that sand particle fracture was a brittle fracture by using a  $\mu$ CT scanning of loading particles.

The simplest form of Weibull (1951) statistics is based on a “weakest link” model

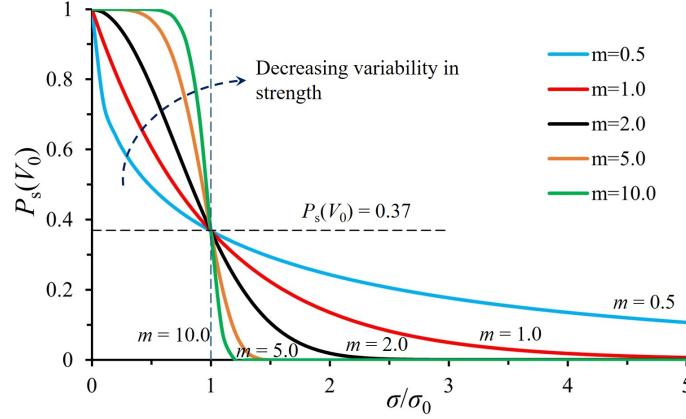


**Figure II .8:** A plot of a Weibull distribution of strength

(Brzesowsky et al., 2011). The model proposes that the whole sample may fail due to the crushing of one element within it. The survival probability  $P_s(V_0)$  for an element of volume  $V_0$  to survive under a uniform tensile stress  $\sigma$  is given by the following relationship:

$$P_s(V_0) = \exp\left[-\left(\frac{\sigma}{\sigma_0}\right)^m\right] \quad (\text{II .27})$$

where  $\sigma_0$  is the tensile strength at which 37% of the total number of tested blocks (of volume  $V_0$ ) survive, and  $m$  is the Weibull modulus. The Weibull modulus  $m$  increases with decreasing variability in strength, as shown in Fig. II .8. All the samples survive when  $\sigma = 0$  and  $P_s(V_0) = 1$ . As  $\sigma$  increases, more and more samples fail and  $P_s(V_0)$  decreases. For large stresses  $\sigma \rightarrow \infty$ , all the samples will fail as  $P_s(V_0) \rightarrow 0$ . The tensile stresses at failure for each set of tests are ranked in ascending order to estimate the survival probability  $P_s$  for each tensile stress at failure. The  $P_s$  is calculated using the mean rank position:  $P_s = 1 - \frac{i}{N+1}$  where  $i$  is the  $i$  th ranked sample from a total of  $N$  (Sullivan and Lauzon, 1986; Wang and Yan, 2013; Shao et al., 2020; Lim et al., 2004).

For a large sample of volume  $V = nV_0$ , the survival probability of the sample is  $\{P_s(V_0)\}^n$ . Thus, the survival probability of a volume  $V$  can be given by:

$$P_s(V) = \left[\exp\left[-\left(\frac{\sigma}{\sigma_0}\right)^m\right]\right]^{\frac{V}{V_0}} = \exp\left[-\frac{V}{V_0}\left(\frac{\sigma}{\sigma_0}\right)^m\right] = \exp\left[-\left(\frac{\sigma}{\sigma_{0v}}\right)^m\right] \quad (\text{II .28})$$

where  $\sigma_{0v}$  is the tensile strength for specimen with volume  $V$  such that 37 % of the tested specimens survive. Using Eq. (II .28) and assuming that the particles are similar in geometry, McDowell & Bolton (1998) gave the survival probability of a particle of size  $d$

under diametral compression as

$$P_s(d) = \exp\left[-\left(\frac{d}{d_0}\right)^3 \left(\frac{\sigma}{\sigma_0}\right)^m\right] \quad (\text{II .29})$$

where  $\sigma$  is the tensile strength of the particle and can be calculated by Eq. (II .25), and  $\sigma_0$  is the value at which 37 % of the tested particles survive. McDowell & Amon (2000) justified the previous Eq. (II .29) mathematically on the assumption that all loading geometries are similar, and the contact area is negligible. It should be noted that Eq. (II .29) also assumes that the material is homogeneous and isotropic (Lim et al., 2004). Eqs. (II .28) and (II .29) shows that the strength of particle  $\sigma_0$  is a function of size. From Eq. (II .29), the characteristic stress  $\sigma_{0d}$  for the particles with  $d$  can be written as:

$$\begin{aligned} \sigma_{0d} &= (\sigma_0 d_0^{3/m}) d^{-3/m} \\ \sigma_{0d} &\propto d^{-3/m} \end{aligned} \quad (\text{II .30})$$

The form of the two previous equations is similar to that of the Eq. (II .26). The Weibull modulus  $m$  can be determined from linear fitting of the plot of  $\ln(\ln(1/P_s))$  against  $\ln \sigma$ .  $\sigma_0$  is the value when  $\ln(\ln(1/P_s)) = 0$  (de Bono, 2013; Zhou et al., 2016). All particle sizes for a given soil type reveal the similar values of Weibull modulus  $m$  (McDowell and Amon, 2000). Plotting the 37% strength  $\sigma_{0d}$  as a function of particle size  $d$  at failure on a double logarithmic graph confirmed the relationship given in Eq. (II .30), as shown in Fig. II .7.

Due to the presence of flaws or weak zones, nature materials such as rock aggregates, often fail at their weakest points (Lobo-Guerrero and Vallejo, 2006a). Although the strength of natural materials exhibits an important variation, the variability of their tensile strength can be described by using an unique value of Weibull modulus  $m$  (Nakata et al., 1999; McDowell, 2002; Lobo-Guerrero and Vallejo, 2006a; Ovalle et al., 2014; Zhou et al., 2016). Experiment data shows that the glass particles ranging from 4.36 to 24.70 mm have an  $m$  between 4.24 and 5.66 (Huang et al., 2014). McDowell & Bolton (1998) proposed that the values of  $m$  for soils to be in the range of 5 to 10. Based on the series of single-particle crushing tests of quartz particles and feldspar particles of Aio sand, Nakata et al. (1999) found  $m$  were respectively 4.2 and 1.8 for quartz and feldspar particles, respectively. McDowell & Amon (2000) tested Quiou sand (a very weak limestone material) in five categories of nominal particle size (1, 2, 4, 8 and 16 mm diameter) and obtained a value of  $m$  1.5. Ovalle et al. (2014) analysed two kinds of rock aggregates, and found that four size fractions of the calcareous rockfill have the Weibull modulus of 1.55, 2.14,

2.51 and 2.52, whereas three size fractions of the quartzite shale rockfill have an  $m$  of 1.53, 1.25, and 1.82, respectively. Zhou et al. (2016) tested a series of cylindrical sandstones, and obtained an  $m$  of 4.29, 5.00, 4.73 and 4.11 for four diameters of samples. Additionally, the Weibull modulus of sands and ballasts with different sizes varies slightly with the mineral composition (McDowell and Amon, 2000; Nakata et al., 2001b; Lim et al., 2004). Therefore,  $m$  is taken as a material constant. However, for some materials with the complex inner microstructure,  $m$  may be a function of particle sizes (Jansen and Stoyan, 2000; McDowell and Humphreys, 2002).

When the RFM is immersed in water, the particle sliding, rearrangement and breakage will be reinforced due to the lubrication effect of water, and then leads to a sudden external deformation (Xu et al., 2009), called wetting deformation (Shao et al., 2020). Studies have shown that the RFM can be wetted by penetrating water, which leads to significant dam settlement during the initial impoundment process (Zhou et al., 2011; Mahinroosta et al., 2015). Hence, some scholars investigated the single particle strength under wet conditions. Ham et al. (2010) performed single particle crushing test on decomposed granite soils and silica sand under both dry and wet conditions, and test results showed that the presence of water led to a reduction in initial crushing strength and an increase in strength variability. Shao et al. (2020) tested a moderately weathered basalt RFM, and founded that the particle strength and stiffness decreased with the increase of water content and particle size.

#### 4.1.3 Size-hardening law

Individual particle crushing test results indicate that for natural particles such as sand, railway ballast and rock aggregate, the yield strength increases with the decreasing median particle size (Drlik, 1987; Lee, 1992; McDowell et al., 1996; Nakata et al., 1999, 2001b; Jansen and Stoyan, 2000; McDowell and Amon, 2000; McDowell, 2002; Lim et al., 2004; Lobo-Guerrero and Vallejo, 2006a; Rozenblat et al., 2011; Wang and Yan, 2013; de Bono, 2013, pg. 89; Zhong et al., 2014; Zhou et al., 2016; Shao et al., 2020).

The size effect on the strength of natural particles can be described by equation (II.26) (following Lee, 1992),  $\sigma_0 \propto d^b$ , as mentioned in section 4.1.1. The  $b$  is the slope of the line of best fit on a plot of  $\log(\sigma_0)$  against  $\log(d)$  (Lim et al., 2004). In addition, the size effect is material dependent, namely, different values of  $b$  for different materials (Lim et al., 2004). Furthermore, the value of  $b$  is not always consistent with the  $-3/m$  (II.30), (McDowell and Amon, 2000; Nakata et al., 1999; Jansen and Stoyan, 2000; Lim et al., 2004; Huang et al., 2014), due to the distribution of flaws and the possibility of no geometric similarity of the

particles (Nakata et al., 1999). Lim et al. (2004) analyzed this phenomenon and given three possible reasons for this observation: (1) a minimum strength in the particles due to the grinding process in the quarry, (2) heterogeneity and anisotropy of the particle, (3) the occurrence of surface fracture (abrasion) (Tsoungui et al., 1999) rather than bulk fracture in the particle. The experimental size-hardening law can be implemented in the numerical modelling concerning the fracture and fragmentation of brittle materials (Huang et al., 2014). Care should be taken when apply the Weibull statistics of fracture to describe the size effect on strength in soil and rock particles under tensile conditions (McDowell and Amon, 2000).

If a given rock mass is assumed to contain a cracks network, the larger the particle under consideration, the higher the probability of having large cracks within the particle (Hardin, 1985; Drlik, 1987; Lade et al., 1996; Liu et al., 1998; Alonso et al., 2012; Frossard et al., 2012; Zhong et al., 2014). In other words, the sizes of particle and of maximum crack are related to each other (Fig. II .9). In fact, small particles are generally obtained from large particles, along these defects. As the breakdown process continues, there are fewer defects in the subdivided particles (Lade et al., 1996). Moreover, according to Fukumoto & Hara (1998), small grains had a high mean crushing strength because they were formed by the breakage at the boundary between different equivalent minerals until they were composed of a single mineral. As a result, small particles have a strong and homogeneous internal structure. In addition, by using a series of DEM simulation of single-particle crushing test, Wang & Arson (2016) concluded that the size effects on particle strength were more likely attributed to the size and number of flaws, rather than to the size of the particle itself.

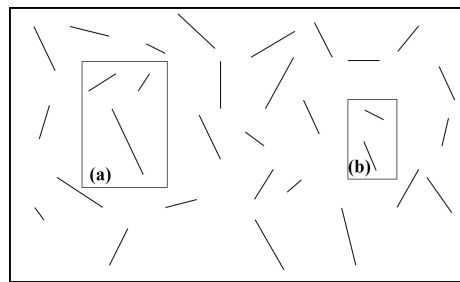


**Figure II .9:** Different specimens coming from same material: (a) large specimen with low tensile strength (contains large and more flaws); (b) small specimen with high tensile strength (after Lobo-Guerrero and Vallejo, 2006a)

Some scholars also investigated the angularity changing law for the particle breakage. Based on a 2D laser image analysis on the uniformly graded samples after one-dimensional

compression test, Altuhafi & Coop (2011) found that the finer particles created by breakage were less spherical and convex, and they had lower aspect ratio than the original particles. Zhao et al. (2015) also found that the sphericity, convexity, and aspect ratio tended to decrease during the particle fracture process by using a  $\mu$ CT scanning. On the other hand, Takei et al. (2001) compared the flatness ratio and elongation ratio of particles before and after crushing tests. They have observed that those ratios became larger after the crushing, indicating that the particles became more spherical. Le Pen et al. (2013) proposed a new measurement technique to evaluate the roundness and demonstrated that the difference of form and roundness among different sizes of particle was slight.

It should be noted that the effect of particle size on the particle strength is not always consistent with the Weibull model, especially for some artificial particles (e.g. granulated coal ash (Yoshimoto et al., 2012)).

#### 4.1.4 DEM simulation of single particle crushing

The single-particle crushing test has been largely simulated in the past two decades (Wang and Yan, 2013). The single particle is always constructed with small elementary particles bonded together. There are several agglomerate generation algorithms available in the literature (Huang et al., 2020). To create an isotropic and spherical agglomerate, the centripetal gravity field is the most used one in some literatures (Thornton et al., 1996; Liu et al., 1999; Liu and Yuan, 2000; Moreno et al., 2003; Thornton et al., 2004). In this method, the particles were randomly generated in a prescribed spherical space, and then a centripetal gravity field was imposed to bring the particles together. The cohesion and friction effects were then introduced to all the particles once the number of interparticle contacts no longer increased (Moreno et al., 2003). On the other hand, some other methods include generating an agglomerate in a spherical shell or an actual-shaped boundary and then expanding and bonding the sub-particles (Wang and Yan, 2013; Cil and Alshibli, 2012; Fu et al., 2017; Huang et al., 2020).

To reproduce the flaws in the agglomerates and to achieve the statistical analysis of tensile strength obtained in the lab test, several strategies are adopted. One is the removal of a certain percentage of elementary balls (McDowell and Harireche, 2002; Wang and Yan, 2013; Wang and Arson, 2016). The others tried to attribute random bond strength on different agglomerate by using a normal distribution function (Cil and Alshibli, 2012), or adopt an uneven radius for the elementary balls (Cil and Alshibli, 2012; Huang et al., 2020).

According to the number of elementary balls, Ergenzinger et al. (2012) concluded that

700  $\sim$  1000 element balls were necessary to get a reliably understanding of the crushing phenomena of rock grains. Wang & Arson (2016) used a cluster contained 11,000 rigid balls for single-particle crushing tests. Huang et al. (2020) adopted more than 2000 elementary balls to form an agglomerate for single particle crushing.

After the sample with flaws has been made, it is installed between two rigid walls while the top platen moves downward until the agglomerate is crushed. The loading rate is sufficiently low to ensure quasi-static conditions and avoid dynamic responses (McDowell and Harireche, 2002; Thornton et al., 2004; Hanley et al., 2011; Wang and Arson, 2016; Huang et al., 2020). Loading velocities ranging from  $1.67\text{e-}4$  to  $1.28$  m/s are used in the simulations (Thornton et al., 2004; Hanley et al., 2011; Cil and Alshibli, 2012), considering both the algorithm stability and the simulation time. To compare with the experimental results, at least 30 samples are crushed in the simulations (McDowell and Harireche, 2002; Wang and Yan, 2013; Huang et al., 2020).

Generally, the crushing of single particle can be qualitatively reproduced by the numerical simulation. The simulation data agrees well with the Weibull distribution in section 4.1.2, and the tensile strength decreases with increasing particle size, which can be observed in both DEM and experimental results (see section 4.1.3) (Wang and Yan, 2013; Huang et al., 2020).

## 4.2 Experimental study of particle breakage

Particle breakage are frequently observed in rockfill dams (Kh et al., 2011), even at relatively low pressures (Lade et al., 1996). Numerous laboratory studies (Marsal, 1967; Lade and Yamamuro, 1996; Lade et al., 1996), have shown that many engineering properties of granular materials, such as strength, deformation, pore pressure distribution and permeability are greatly influenced by the particle breakage (Lade and Yamamuro, 1996; Lade et al., 1996).

It is widely accepted that the crushing of particle is influenced by the particle size distribution, the particle shape, the mineralogy, the strength of the grains, the density, the water condition of studied material, the effective stress path, and most importantly the effective stress state (Hardin, 1985; Nakata et al., 1999; Ham et al., 2010; Wang and Yan, 2013; de Bono, 2013; Shao et al., 2020). The particle shape has also an important effect on the crushing of grain (Ueda et al., 2013). Hagerty et al (1993) discovered that angular particles crushed more strongly with respected to the spherical particles, particularly at low level of imposed vertical stresses in one-dimensional compression tests.

The impact of particle breakage is accentuated under the high level of applied stress

(Lade et al., 1996). Lade et al. (1996) found that in triaxial extension tests, less particles are broken with respect to the triaxial compression test. Particle crushing induces the irreversible volume contraction in one-dimensional and isotropic compression and decreases the volumetric dilation in the triaxial shear test under high confining pressures (Hardin, 1985). In addition, particle breakage also has a strong effect on the internal friction angle of material. However, contradictory conclusions are also found in the previous works: some scholars found particle breakage increased the internal friction angle (Corriveau et al., 1997; Ueng and Chen, 2000; Tarantino and Hyde, 2005), some concluded that the particle crushing reduced the internal friction angle (Varadarajan et al., 2003; Kh et al., 2011; Ovalle et al., 2014), and the others found there was no effect on the mobilized strength (Coop et al., 2004). This discrepancy may be due to the difference in the test conditions, such as particle gradation, particle size and loading conditions, etc... In conclusion, particle breakage contributes to the shear strength of studied material in two ways: (1) a reduction of dilatancy in drained condition or an increase of pore pressure in undrained condition, and then resulting in a low shear strength; (2) an increase of energy consumption during shearing deformation, resulting in high shear strength (Ueng and Chen, 2000).

To sum up, particle breakage increases with (Lee and Farhoomand, 1967; Hardin, 1985; Hagerty et al., 1993; Lade et al., 1996; Ueng and Chen, 2000; Nakata et al., 2001a; Yoshimoto et al., 2012): (1) increasing uniformity of the particle size distribution, (2) increasing grain size of uniform granular materials, (3) increasing particle angularity, (4) increasing mean effective stress, (5) increasing initial density, (6) decreasing particle strength and (7) decreasing water content. These observation are due to the following phenomena (Lade et al., 1996): (1) the possibility of particle crushing increases as the particle size increases, which is due to the fact that large particles contain more flaws or defects, (2) increasing the particle angularity increases the possibility of particle breakage because stresses can concentrate along their narrow dimension at angular contact points, (3) well-graded granular materials do not break down as easily as uniform soils because more particles surrounding each particle in a well-graded soils, which leads to the decrease of average contact stresses.

#### 4.2.1 Measurement of particle breakage

To evaluate the particle breakage, several methods have been proposed (Miura et al., 1979; Ham et al., 2010) and can be classed in two groups (Stoeber, 2012): (1) quantification of particle breakage, and (2) incorporation of particle breakage into a conceptual framework.



To quantify particle breakage, some research works are based on the single particle size, while others are based on the changes in the overall particle size distribution (Lade et al., 1996). Lee & Farhoomand (1967) adopted the “relative crushing”  $D_{15i}/D_{15a}$  to quantify the degree of particle breakage, where  $D_{15i}$  and  $D_{15a}$  were the initial 15% size of tested material and the 15% size after testing. The lower limit of this ratio is unity and there is no upper limit. Marsal (1967) proposed the “particle breakage  $B_g$ ” which was calculated by using the difference of the grain size distributions between before and after testing. The Marsal’s index varies from zero to a theoretical upper limit of 100%. Hardin (1985) defined a relative breakage  $B_r$ , which was given by  $B_t/B_p$ . The breakage potential  $B_p$  was the area enclosed by the line defining the upper limit of the size in the PSD curve and the PSD curve, and the total breakage  $B_t$  was the variation of of the PSD curve before and after testing. The relative breakage  $B_r$  varies from zero and unity (i.e. the theoretical upper limit of unity).

On the other hand, Lade et al. (1996) proposed a particle breakage as  $B_{10} = 1 - D_{10f}/D_{10i}$ , where  $D_{10f}$  and  $D_{10i}$  were the 10% of the effective grain size in the final and initial gradation. The lower limit of  $B_{10}$  is zero when there is no particle breakage, and the upper limit is unity at infinite particle breakage. Nakata et al. (1999) proposed a simple particle breakage  $B_f$ ,  $B_f = R/100$ . After all the particles were tested,  $R$  was the percentage of particles smaller than the minimum particle size in the original sand. By introducing the initial and ultimate grain size distributions, Einav (2007) modified the Harin’s breakage index  $B_r$ . The modified  $B_r$  was the ratio of area  $B_t$  to  $B_p$ , where  $B_t$  was the area enclosed by the initial and the current grain size distributions and  $B_p$  was the area enclosed by the initial and ultimate grain size distributions. Generally, the ultimate particle size distribution was assumed to be a fractal distribution given by  $F_u(d) = (d/d_M)^{3-D}$ , where  $d$ ,  $d_M$  and  $D$  were the particle size, maximum particle size, and fractal dimension, respectively.

#### 4.2.2 Particle size effect on particle breakage

As aforementioned, for the natural particles (e.g., sand, railway ballast and rock aggregate), their yield strength decreases with increasing particle size. Consequently, it can be inferred that for a granular material with uniform particles, the particle breakage should augment with the increasing particle size, which has been verified by the laboratory test (Lade et al., 1996). Hu et al. (2011) investigated a calcareous RFM by large triaxial tests. For the samples with the same density, the samples containing bigger particles exhibited a more important amount of particle breakage. Ovalle et al. (2014) also performed large

triaxial test on two kinds of RFM with two gradations scaled by parallel gradation technique, and the test results showed that the particle breakage index  $B_g$  proposed by Marsal (1967) increased with increasing particle size.

For granular materials with non-uniform particles, the particle crushing can be studied in two cases. If the particles size distribution (PSD) curves of the granular materials tested in the laboratory tests are obtained by using a parallel scalping technique, the in-situ PSD curve of studied materials is similar to that of laboratory. The results obtained with uniform particles can be applied. If the PSD curves are different, in other words, the particle packings are different and the results would be different. For a granular material, the survival probability of particle are influenced by two issues: particle size and coordination number (McDowell and Bolton, 1998; Nakata et al., 2001b; McDowell and Humphreys, 2002; Wood and Maeda, 2008). Jaeger (1967) showed that for circular particles under combinations of surface forces, the maximum tensile stress created in a particle decreases as the coordination number increases. The probability of particle breakage increases with increasing particle size and decreasing coordination number. In practice, small particles are statistically stronger and have small number of contacts. When sufficient small particles are positioned around a large particle, a high value of coordination number is observed in the large particle. As a result, the particle breakage depends on the combined effects of particle size and coordination number (Nakata et al., 1999).

### 4.3 DEM study of particle breakage

In DEM, particle breakage can be studied via two alternative models (de Bono, 2013; Li, 2013): bonded particle model (BPM) (Potyondy and Cundall, 2004) and population balance model (PBM) (Cleary et al., 2011; Zhou et al., 2016). The two models will be presented in the following.

#### 4.3.1 Bonded particle model (BPM)

The bonded particle model (BPM) was developed by Potyondy & Cundall (2004). The particle is modelled by an assembly of bonded micro-spheres. The crushing of particle is modelled by the bond breakage.

In this approach, the packing method of micro-spheres in the agglomerate is important because it directly determines the fabric structure of the agglomerate (Li, 2013). To realistically reproduce the size effects on the strength, an agglomerate should comprise at least 500 spheres, which would significantly reduce the computational efficiency (Lim, 2004; Lim and McDowell, 2007; de Bono and McDowell, 2014; de Bono et al., 2014; Wang

et al., 2017). In addition, since the agglomerates are porous and have internal voids, the BPM cannot quantitatively simulate the evolution of voids ratio (de Bono and McDowell, 2016a).

#### 4.3.2 Population balance model (PBM)

The population balance model (PBM), is also called the replacement method (de Bono, 2013; Li, 2013; Weerasekara et al., 2013; Singh, 2017). In this method, the collision energy and/or stress are monitored for each particle. When the breakage thresholds are attained, the parent particle is replaced by a collection of progeny particles that are densely packed into the original space of the parent particle (Weerasekara et al., 2013; Singh, 2017). The PBM allows spherical particles to be broken into spherical progeny. An optimal apollonian packing approach (Borkovec et al., 1994; Aharonov and Stephenson, 1998) is always used to specify the progeny size distribution and arrangement. Recently, this method has been extended in order to simulate the breakage of non-spherical particles (Eliás, 2014).

With respect to the bonded particle model, the main advantage of PBM is computational economy (Weerasekara et al., 2013). The most important issues in the application of PBM is the choice of breakage criteria and progeny arrangements (de Bono and McDowell, 2016a; Zhou et al., 2020, 2016; Zheng and Tannant, 2018). The breakage criteria determine which particles should be broken and the progeny arrangements determine the size distribution and positions of the progeny particles.

**4.3.2.1 Particle breakage criterion** Two fracture modes occur in the single particles: tensile fracture and shear fracture (Takei et al., 2001; Refahi et al., 2007; Wood and Maeda, 2008; Ben-Nun and Einav, 2010; Kh et al., 2011; Cil and Alshibli, 2012; Zhou et al., 2015, 2016). The small particles are more likely to be subjected to the tensile fracture loading, while the great number of contacts makes large particles susceptible to be subjected to a shear fracture loading (Wood and Maeda, 2008).

McDowell & de Bono (2014; 2015; 2013) assumed that a particle would break when the octahedral shear stress was greater than or equal to its strength. In their works, only the shear fracture mechanism is considered. On the other hand, some researchers assumed that a particle would break if the characteristic tensile stress exceeded its crushing strength value (see equation (II .25)) (Lobo-Guerrero and Vallejo, 2005a,b,c, 2006b; Marketos and Bolton, 2009). However, the fracture mode depends on the contact conditions. There are two opposing factors for the particle survival: the particle size and the coordination number. Small particles are strong and have few contacts, whereas large grains tend to be

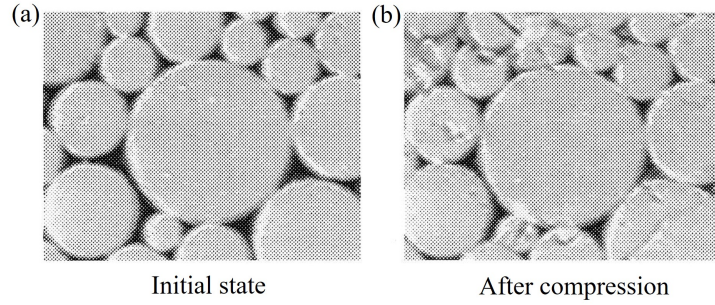


**Figure II .10:** Enlargement of a region of granular material in a two-dimensional packing for uniaxial test: (a) the hydrostatic effect on a large grain surrounded with small grains; (b) despite the increasing external pressure, the large grain fracture becomes impossible because of this hydrostatic effect (Tsoungui et al., 1999)

difficult to break due to the dominating hydrostatic effects created by their large number of contacts (Jaeger, 1967; Tsoungui et al., 1999; McDowell and Bolton, 1998; McDowell and Amon, 2000; Nakata et al., 2001b; McDowell and Humphreys, 2002; Wood and Maeda, 2008; Zhou et al., 2016). As the number of contact points increases, the tensile strength in a particle decreases and the probability of particle survival increases (Nakata et al., 1999; Tsoungui et al., 1999; Wang and Arson, 2016). This phenomenon is called the “shielding effect” (Wang and Arson, 2016) or hydrostatic effect (Tsoungui et al., 1999) (Fig. II .10). When the contact tends to be linear or pointed, the tensile fracture becomes more dominant than the shear fracture, like a Brazilian test (Refahi et al., 2007). Zhou et al. (2016) employed a Mohe-Coulomb model to capture the predominant fracture modes, including both the shear and tensile fractures.

De Bono & McDowell (2016a) gave a comprehensive comparison of several crushing criteria using different crushing stress indexes. They found that the criteria using octahedral shear stress or the stress induced by the maximum normal contact force ( $F_{max}/d^2$ ) are capable of correctly describing the stress-strain behaviour as well as the fractal PSD curve of granular materials.

**4.3.2.2 Fragments spawning** Åström & Herrmann (1998) proposed that a good fracture mode should fulfil three criteria: (1) the number of fragments at each breaking should be kept low so that many breakings can be made in each simulation; (2) the fragments should be chosen so that they can be packed in such a way that the local pressure decreases at a break; (3) the breaking mechanism should mimic the real event.

McDowell & de Bono (2014; 2015; 2013) split a particle into two equally sized fragments and obeyed the mass conservation law. After that, based on the results of single-particle

crushing test, Zhou et al. (2015) modified this fracture mode by using three equally sized fragments. The small particles were placed at the equilateral triangle vertex, and enough overlaps were applied among particles to assure the fragments within the parent particle. The mass conservation law was also obeyed. This fracture mode was further modified by replacing each of the three equally sized fragments with nine small spheres. These nine spheres were “clumped” together and can be released from the clump when the fragment stresses attained the failure criterion (Zhou et al., 2016).

However, experimental results of single-particle crushing test showed that some granular particles (such as orthoclase feldspar and glass bead) shattered into many pieces of different sizes (Takei et al., 2001; Huang et al., 2014), whereas other samples (such as quartzite and limestone) tended to break into two or three main fragments as well as some small pieces (Nakata et al., 1999; Lobo-Guerrero and Vallejo, 2006b; Ham et al., 2010; Cil and Alshibli, 2012; Cheshomi and Sheshde, 2013; Zhong et al., 2014; Zhao et al., 2015; Huang et al., 2020; Shao et al., 2020) (Fig. II .11). In practice, the particle breakage can be classified according to three modes (as shown in Fig. II .12) (Daouadji and Hicher, 2010; Daouadji et al., 2001):

- fracture: a grain breaks into smaller grains of similar sizes,
  
- attrition: a grain breaks into one grain of a slightly smaller size and several much smaller ones,
  
- abrasion: the result is that the granulometry remains almost constant but with a production of fine particles.

Moreover, by a  $\mu$ CT scanning of particles during loading, Zhao et al. (2015) confirmed that the initial particle morphology, heterogeneity, and mineralogy were three important factors, controlling the fracture patterns. In view of this, equally sized fragments could not simulate the real crushing processes of particles (Zhou et al., 2016).

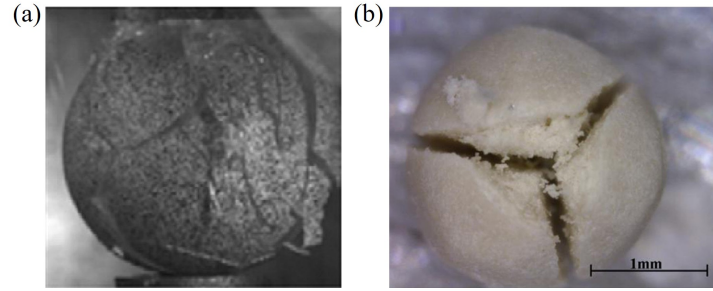


**Figure II .11:** Two typical failure pattern for single particles: (a) glass sphere with  $\Phi 25.03$  mm (after [Huang et al., 2014](#)); (b) limestone sphere  $\Phi 2.00$  mm (after [Cheshomi and Sheshde, 2013](#))

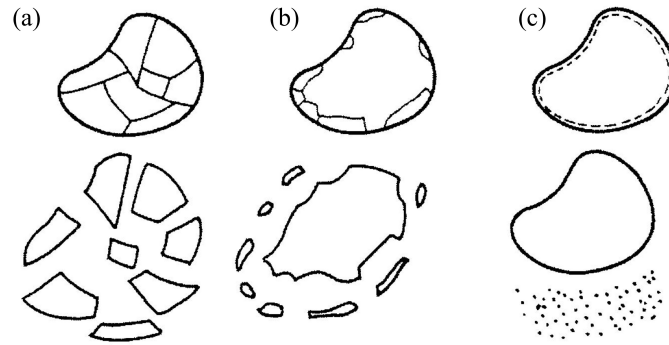


**Figure II .12:** Different modes of grain breakage: (a) fracture; (b) attrition; and (c) abrasion (after [Daouadji and Hicher, 2010](#); [Daouadji et al., 2001](#))

To model the fragmentation of grains, Drlik (1987) used two large discs and two small discs to replace the original disc. Tsoungui et al. (1999) added eight small discs based on the breakage configuration proposed by Drlik. Similarly, Lobo-Guerrero & Vallejo (2005a; 2005b; 2005c; 2006b) assumed a distribution characterized by two large fragments, and they packed 8 fragments into the area of the broken grain. However, the mass was not conserved in this method. Åström & Herrmann (1998) and Tsoungui et al. (1999) allowed a grain to break into 12 fragments with three and four different sizes, respectively.

## 5 Research scope

Based on the previous discussion, the main objective of this thesis is to answer some of the above-mentioned problems. The effects of particle size will be investigated by laboratory tests and DEM simulation to evaluate the crushing of rockfill particles and the mechanical behaviour of rockfill materials (RFM).



## Chapter III

# Experimental study of the particle size effects on the crushing and mechanical behavior of RFM

### 1 Introduction

Rockfill material (RFM) has been widely used in the construction of earth-rockfill dams due to its local availability and cost-effectiveness. The stability and security of rockfill dams requires a good understanding of the mechanical characteristics of RFM. Numerous experimental devices have been performed to study the crushing and mechanical characteristics of rockfill materials ([Marsal, 1967](#); [Marachi, 1969](#); [Marachi et al., 1972](#); [Charles and Watts, 1980](#); [Indraratna et al., 1993](#); [Varadarajan et al., 2003](#); [Xiao et al., 2014a,b](#)). As the used rockfill particles may be larger than 1 m, the particles of studied materials are firstly scaled down to an allowable size for the preparation of laboratory test. The hybrid method ([CS, 1999](#)), which is a method combined the parallel gradation and replacement techniques, is used in the present study. In the laboratory test, the specimen diameter ranges from 15.2 to 500 mm with the maximum particles size  $d_M$  varying from 3.8 to 100 mm. As the loading conditions and material properties of scaled laboratory sample may be different from that of the in-situ one, it is necessary to study the particle size effects on the crushing and mechanical characteristics of rockfill materials and then establish the relationship between the laboratory results and in-situ properties or behavior.

In view of this, some laboratory tests have been conducted on a large variety of rockfill materials to study the influence of particle size on the crushing and mechanical behavior. For instance, according to the mechanical strength, the obtained conclusions were different



or even opposite. Some researchers (Marsal, 1967; Marachi et al., 1972; Kong et al., 2019) found that the mobilized internal friction angle at peak  $\varphi_f$  decreased with increasing  $d_M$ . Inversely, Hu et al. (2011) proposed that the  $\varphi_f$  was less affected by  $d_M$  while Li et al. (2001) found an increase of  $\varphi_f$  with  $d_M$ . For the particle size effects on the deformation behavior of RFM, due to the scatted volumetric strain measurement and the complex influencing factors (such as gradation, density, mineral composition, particle breakage, etc...), few valuable conclusions were obtained. Although numerous research works have been performed on the scaled granular materials, the study of the particle size effects on the mechanical behavior of rockfill materials is still limited and needs a further research.

The main objective of this chapter is to investigate the particle size effects on the crushing of rockfill particles via a series of single-particle crushing tests and on the mechanical behavior of rockfill materials via a series of triaxial tests. The influence of particle size  $d_M$  on dry density, strength-deformation, characteristic stress state, particle breakage is analyzed. In addition, the fractal behavior and particle breakage are discussed.

## 2 Rockfill materials

The studied materials are obtained from the Shuang-Jiang-Kou rockfill material resources field in western China. It belongs to a biotite feldspar granite. The specific gravity of RFM particles is 2.68. The material consists of angular/subangular particles up to 600 mm in size (Fig. III .1, only particles with diameter less than 100 mm are given). The maximum grain size is greater than the limit of the conventional test apparatus in laboratory. Therefore, the RFM should be scaled by the aforementioned scaling techniques.



**Figure III .1:** Shuang-Jiang-Kou rock aggregates in different size fractions

The hybrid method (CS, 1999, 2006) is chosen in the present study. In practice, it is a method combining the parallel gradation and replacement techniques. In this method,

the gradation is firstly scaled parallelly by an appropriate ratio to make sure that the content of finer fraction ( $d < 5$  mm) is less than 30%. Then, if the oversized fraction still remains, it will be replaced proportionally by the coarser fraction ( $5 \text{ mm} < d < d_M$ ). As a result, the scaled gradation has a similar shape to the prototype, and the finer part is also limited.

The particles were dried and sieved to obtain three size categories: 5 ~ 10 mm, 10 ~ 20 mm and 20 ~ 40 mm for single-particle crushing tests. In order to identify the Weibull probability distribution function (Huang et al., 2020; Lim et al., 2004; McDowell, 2001), thirty particles with similar shapes were investigated for each size category, with the average diameters  $d_{av}$  of 7.81, 14.95 and 24.93 mm, respectively. The particle diameter is determined by using the height of grain in its most steady position, indicating that the upper contact is usually a point while the bottom contact is usually a nominal face formed by three points (Zhou et al., 2016; Lim et al., 2004). The value obtained before loading is called the initial diameter  $d_{int}$  while the one obtained at failure, called the diameter at failure  $d_f$ .

According to the dimension of laboratory equipment, six maximum particle sizes  $d_M$  (10, 20, 40, 60, 80 and 100 mm) are selected for triaxial compression tests. The values of  $d_M$  is determined by considering the commonly used sample sizes in laboratory. In practice, the diameter of triaxial samples can be 61.8, 101 and 300 mm while the maximum particle size allowable is 1/5 of the diameter (ASTM, 2020a; CS, 1999, 2006), namely, 10, 20 and 60 mm.

The particle size distribution (PSD) curves for prototype and scaled rockfill materials are given in Fig. III .2. Different curves are classed by letter H and one number. The letter H represents the hybrid method and the number indicates the value of  $d_M$ .

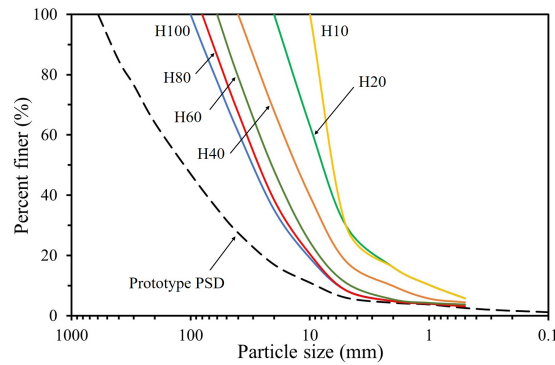


**Figure III .2:** Particle size distribution (PSD) curves for prototype and scaled rockfill materials

In the literature, the sample density is usually characterized by dry density, relative density, or compaction work (Weng et al., 2009; Hu et al., 2011; Honkanadavar and Sharma, 2016). As a granular material, the compaction of rockfill material is related to the relative density (Varadarajan et al., 2006, 2003). In the present study, a dry density corresponding to 90% of relative density is adopted (Table III .1). The minimum dry unit weight (or  $e_M$ ) is obtained by depositing the soil carefully into a given container, corresponding the loosest state of studied materials (ASTM, 2016b; CS, 2006). The maximum dry unit weight (or  $e_m$ ) is determined by using surface vibration compaction tests (ASTM, 2020b; CS, 2006).

Each individual fraction is mixed according to the given PSD to prepare for the laboratory samples. In the dry density test, the specimen is not divided into layers before compaction, while in the triaxial test, it is prepared by compacting the material in five equal layers.

### 3 Single-particle crushing tests

All the samples are compressed by using a universal testing machine, INSTRON model 8031 (Figure III .3). In the laboratory test, the sample is placed in its most steady position between two rigid platens. The bottom platen moves upward with a constant speed (1 mm/min) until the sample is broken into two or more pieces. Both the applied force and the displacement of the bottom platen are recorded during the test.

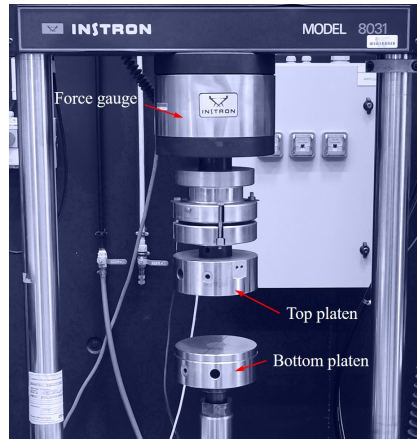


**Figure III .3:** Single-particle crushing device INSTRON

The typical force-displacement curves are given in Fig. III .4 for three different sizes. In general, two types of force-displacement curves are observed. The first type is given in

the Fig. III .4A,C. One observes that the curve is stiff and smooth until the occurrence of an important force drop, indicating a sudden breakage of the particle. The steep drop also indicates the brittle behaviour of the studied RFM particle. The second type is observed in Fig. III .4B,D,E,F. At the beginning, the force-displacement curve exhibits some sawtooth peaks, representing the crushing of the angular edges of the particles. When the force reaches the peak value, it decreases sharply as the main part of the particle is broken up. After that, the force decreases in a zigzag fashion, indicating the crushing of the remaining part of the particle. In the post-peak phase, a residual force is still observed with the increase of displacement (Fig. III .4A,B,C,D,E). This observation is due to the fact that the crushed fragments can still more or less bear the applied force. The obtained force-displacement curves are similar to those for feldspar (Nakata et al., 1999) and sandstone (Xiao et al., 2020). By comparing the peak values of force obtained with different particle sizes, one observes that the peak force  $F_f$  increases with increasing particle size. For instance,  $F_f$  for the No.1 with 5 ~ 10 mm is equal to 0.64 kN, while  $F_f$  for the No.1 with 20 ~ 40 mm rises to 3.39 kN.

The failure patterns of RFM particles are also given in Fig. III .4. The particles are generally broken into two or three major pieces. This failure pattern can also be observed in quartzite and limestone particles (Cil and Alshibli, 2012; Huang et al., 2020; Zhao et al., 2015; Cheshomi and Sheshde, 2013; Nakata et al., 1999; Shao et al., 2020; Zhong et al., 2014; Ham et al., 2010; Lobo-Guerrero and Vallejo, 2006b). However, for the particles of orthoclase feldspar and glass, they are usually shattered into many pieces of different sizes in single-particle crushing tests (Huang et al., 2014; Takei et al., 2001).

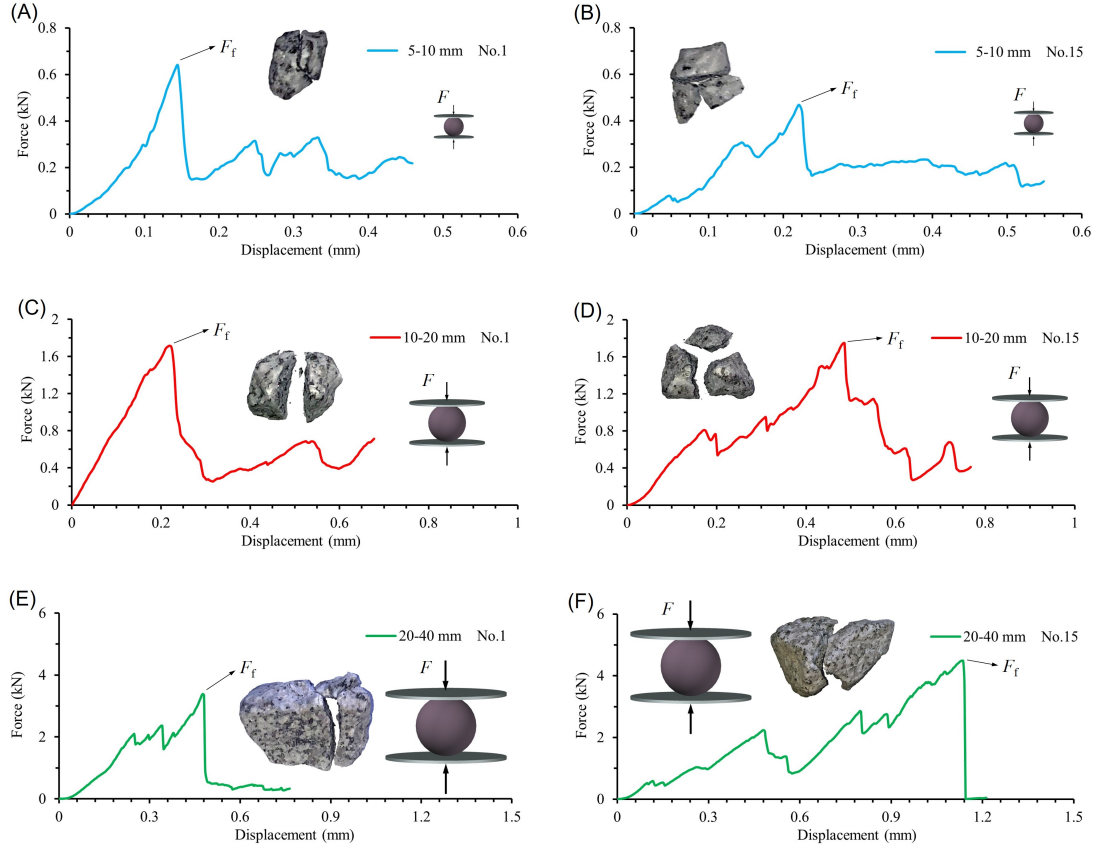


**Figure III.4:** Typical force-displacement curves obtained in single-particle crushing tests with three sizes: (A) 5 ~ 10 mm No.1; (B) 5 ~ 10 mm No.15; (C) 10 ~ 20 mm No.1; (D) 10 ~ 20 mm No.15; (E) 20 ~ 40 mm No.1; (F) 20 ~ 40 mm No.15

## 4 Density and triaxial test programs

### 4.1 Test apparatus

The schematic diagram of the surface vibration test device is given in Fig. III.5a. A steel mold (diameter 303 mm, height 418 mm) is used for measuring the dry density of RFM. The surface vibrator has an exciting force of 4.2 kN with a motor frequency 50 Hz and an amplitude of 2 mm. A steel plate is positioned on the top of the sample to guarantee a uniform distribution of stress on the sample. The plate is 280 mm in diameter and 20 mm in height. The static pressure applied on the samples by the vibration hammer is 14 kPa.

The used large scale triaxial apparatus is located in the key laboratory of ministry of education for geomechanics and embankment engineering, Hohai University, China. The

sample size is 300 mm in diameter and 600 mm in height. Details of the equipment are given in Fig. III .5 (b). The cell is designed to support vertical load up to 1000 kN and confining pressure of 3 MPa.

A double-wall chamber is adopted in the equipment, and the outer and inner volumes are filled simultaneously with water. Therefore, the volume of inner compartment containing the sample can be assumed to be constant during the test. The volume change is measured by using the water change of inner volume. On the other hand, to measure the vertical force, a force gauge is embedded on the top of the piston, and an LVDT is placed outside of the chamber for the vertical displacement.

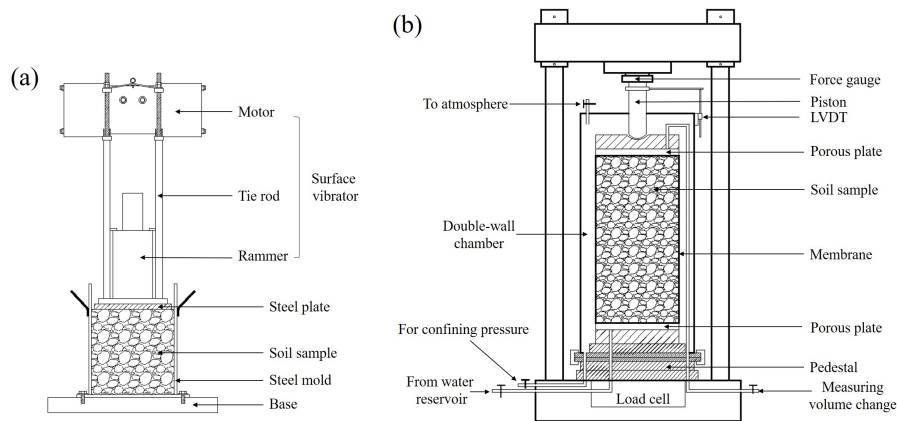


**Figure III .5:** Configuration of laboratory apparatus: (a) surface vibration test device; (b) large scale triaxial device

## 4.2 Test procedure

According to the scaled grading, the quality for each size fraction of RFM is verified by weight. The studied rockfill materials are then deposited carefully into the mold and the loosest state is attained. By measuring the height of sample, the minimum dry density can be identified. After that, a steel plate is placed on the surface of the sample, on which the surface vibrator is placed. The vibration time is 15 mins for the densest state. Thus, the maximum dry density can be determined. Two measurements of dry density are performed for each group.

A brief description of triaxial test procedure is presented in the following. The sample is prepared in five layers in a split mold. Each layer is compacted by a vibrator. Before filling the mold, a membrane is pushed against the mold by a vacuum of 50 kPa. After the sample has been made, it will be covered by another membrane. The sample is applied by a vacuum of 50 kPa to check the air tightness. The double-wall chamber is then filled

with water, and a lateral pressure of 30 kPa is maintained for 15 mins. After that, the sample is saturated by passing water through the base of the triaxial cell and using a top drainage system for removing air voids.

The prepared sample is then subjected to the required consolidation pressure and sheared by applying axial loading with a rate of 1 mm/min. The vertical displacement is measured by an LVDT which is placed outside of the chamber. The vertical force is determined by a force gauge embedded on the top of the piston. The volume change is obtained by measuring the volume of water drained from the sample. All the data is recorded by a computer system at period intervals. The shear procedure is terminated when the axial strain reaches 15%. The range of confining pressures, i.e., 300, 600, 1000 and 1500 kPa, is chosen considering the stress levels in the dam (Table III .1).

**Table III .1:** Dry density of soil samples and confining pressure used in triaxial test

Test-ID	$d_M$ (mm)	$\rho_{dm}$ (g/cm <sup>3</sup> )	$\rho_{dM}$ (g/cm <sup>3</sup> )	$\rho$ (g/cm <sup>3</sup> ) (relative density 0.9)	$\sigma_3$ (kPa)
H10	10	1.478	1.865	1.817	300, 600, 1000, 1500
H20	20	1.554	1.961	1.911	300, 600, 1000, 1500
H40	40	1.566	1.999	1.945	300, 600, 1000, 1500
H60	60	1.583	2.008	1.956	300, 600, 1000, 1500
H80	80	1.584	2.018	1.964	300, 600, 1000, 1500
H100	100	1.624	2.044	1.992	300, 600, 1000, 1500

## 5 Experimental results of density and triaxial tests

### 5.1 Particle size effect on dry density

Fig. III .6 shows the relationship between the dry density  $\rho_d$  and the maximum particle size  $d_M$ . Both the maximum and minimum dry densities increase with the increasing  $d_M$ . The value of  $\rho_d$  increases rapidly with  $d_M$  when  $d_M$  ranges from 10 to 40 mm, and tends to stabilize to a constant value when  $d_M$  exceeds 40 mm. The increase of  $\rho_d$  with increasing  $d_M$  is due to the evolution of gradation: with a wider range of size fractions, the sample with large  $d_M$  is better graded than that with small  $d_M$ . This observation is consistent with the previous laboratory test results (Pike, 1972; Stoeber, 2012; Verdugo and de la Hoz, 2007).

Based on the work of Zhu et al. (2010), the normalized parameter  $\lambda$  can be used to



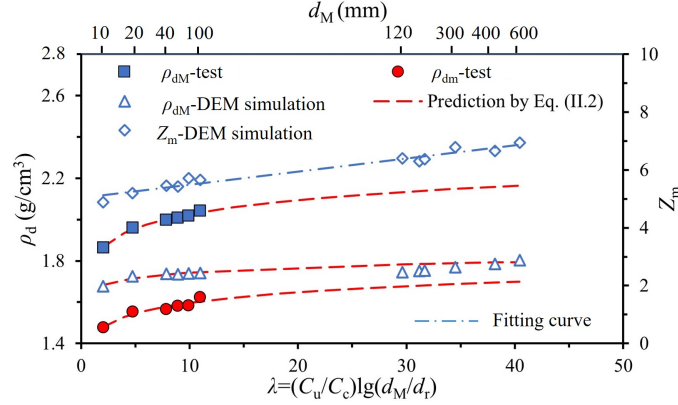


**Figure III .6:** Relationship between the dry density (or average coordination number), normalized parameter  $\lambda$  and maximum particle size  $d_M$

describe the relationship between dry density, gradation and maximum particle size, which can be expressed as

$$\lambda = C_u/C_c \lg(d_M/d_r) \quad (\text{III .1})$$

where  $C_u$  = coefficient of uniformity,  $C_c$  = coefficient of curvature,  $d_r = 1$  mm, i.e., referenced size. The relationship between dry density and  $\lambda$  is given in Fig. III .6. The data points can be well fitted by a logarithmic function:

$$\rho_d = \rho_w(a \ln(\lambda) + b) \quad (\text{III .2})$$

where  $a$  and  $b$  are the sample parameters;  $\rho_w$  = the density of water,  $1 \text{ g/cm}^3$ . In the present study,  $a$  and  $b$  are 0.10 and 1.80, 0.07 and 1.43, for the maximum and minimum dry density, respectively. For the prototype gradation ( $C_u = 19.61$ ,  $C_c = 1.35$ ,  $\lambda = 40.4$ ), the  $\rho_{dM}$  and  $\rho_{dm}$  are estimated to be  $2.164$  and  $1.700 \text{ g/cm}^3$  by Eq. (III .2), increasing  $7.74\%$  and  $7.37\%$  compared to the values of H60 sample, respectively.

The estimated dry density of prototype RFM needs a further verification due to the excessive extrapolation. To verify the prediction of Eq. (III .2), a DEM simulation of dry density test is performed. The particles are generated according to the PSD curves in Fig. III .2. For the samples with  $d_M = 120 \sim 400$  mm, the parallel gradation technique is used for the scaling. The finer fractions (size smaller than 5 mm) are all replaced by the particles with size  $d = 5$  mm. The particles are firstly deposited under gravity and then subjected to a vertical pressure by putting a steel plate on its surface. The steel plate is vibrated along the vertical direction for 1 min according to  $Z(t) = A \sin(\omega t + \varphi_0)$ , where  $A = 2$  mm, amplitude;  $\omega = 100\pi$  (rad/s), frequency;  $\varphi_0 = \pi/2$ , initial phase.



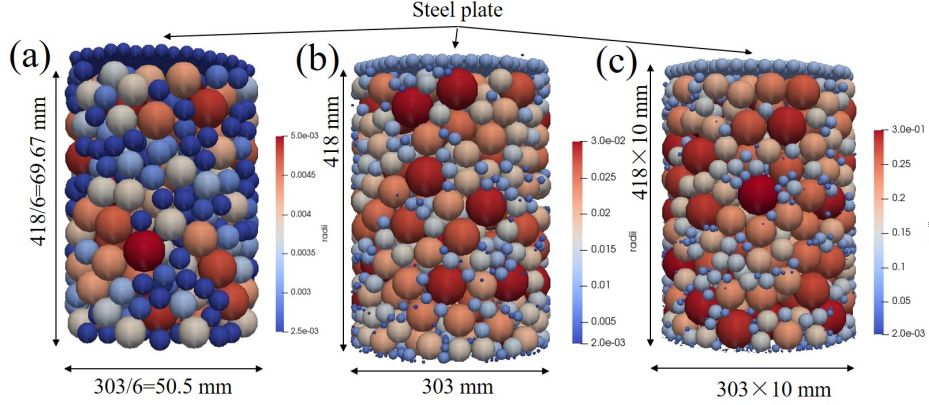


**Figure III .7:** DEM samples with three maximum particle sizes: (a)  $d_M = 10$  mm; (b)  $d_M = 60$  mm; (c)  $d_M = 600$  mm

The sample with  $d_M = 60$  mm is 303 mm in diameter and 418 mm in height. For the rest of samples, their diameter and height are scaled by the factor  $f = d_M/60$  to guarantee the same sample-size ratio (SSR), which is the ratio of the specimen diameter to  $d_M$  (Holtz and Gibbs, 1956; Marachi, 1969; Stoeber, 2012). Note that the amplitude and pressure applied by steel plate are also scaled by the factor  $f$  to make the sample in a dense state. Linear contact model (Cundall and Strack, 1979) in DEM is used with the Young's modulus of 60 MPa and Poisson's ratio of 0.45. The density of particles is 2680 (kg/m<sup>3</sup>). No calibration is made here, and the DEM simulation focuses on the study of correlation between  $\rho_{dM}$  and  $d_M$ . The typical samples with  $d_M = 10, 60$  and 600 mm are given in Fig. III .7. The steel plate is created by a cylindrical hexagonal close packing (HCP) without interaction within it.

In the numerical samples, the  $\rho_{dM}$  increases with increasing  $d_M$ . When  $d_M \leq 20$  mm,  $\rho_{dM}$  increases rapidly with  $d_M$ . This rapid increase of  $\rho_{dM}$  is satisfactorily captured by the numerical simulations. However, the increase rate is lower than that the observed result in the laboratory tests. This difference is related to the neglect of particle breakage in DEM. The fitting curve (dashed line in Fig. III .6) for numerical sample is determined by the results with  $d_M = 10 \sim 100$  mm. Consequently, the predicted dry density of samples with  $d_M = 600$  mm is 1.794 g/cm<sup>3</sup>, which is close to the numerical result (1.804 g/cm<sup>3</sup>).

The coordination number is a scalar variable and used to quantify the contact density in a particulate assembly. The average coordination number  $Z_m$  proposed by (Thornton, 2000) is calculated by

$$Z_m = \frac{2N_c - N_p^1}{N_p - N_p^0 - N_p^1} \quad (\text{III .3})$$

where  $N_c$  is the number of contacts in the system;  $N_p$  is the number of particles;  $N_p^0$  and  $N_p^1$  are the number of particles with no or only one contact, respectively.  $Z_m$  is related to the specimen void ratio  $e$  (Sitharam et al., 2002; Agnolin and Roux, 2007). The increased  $Z_m$  with  $d_M$  (Fig. III .6) confirm again the rise of dry density. Moreover, more contact points within the assembly are also related to a steady fabric in the samples with large  $d_M$ .

## 5.2 Particle size effect on stress-strain-volume relationship

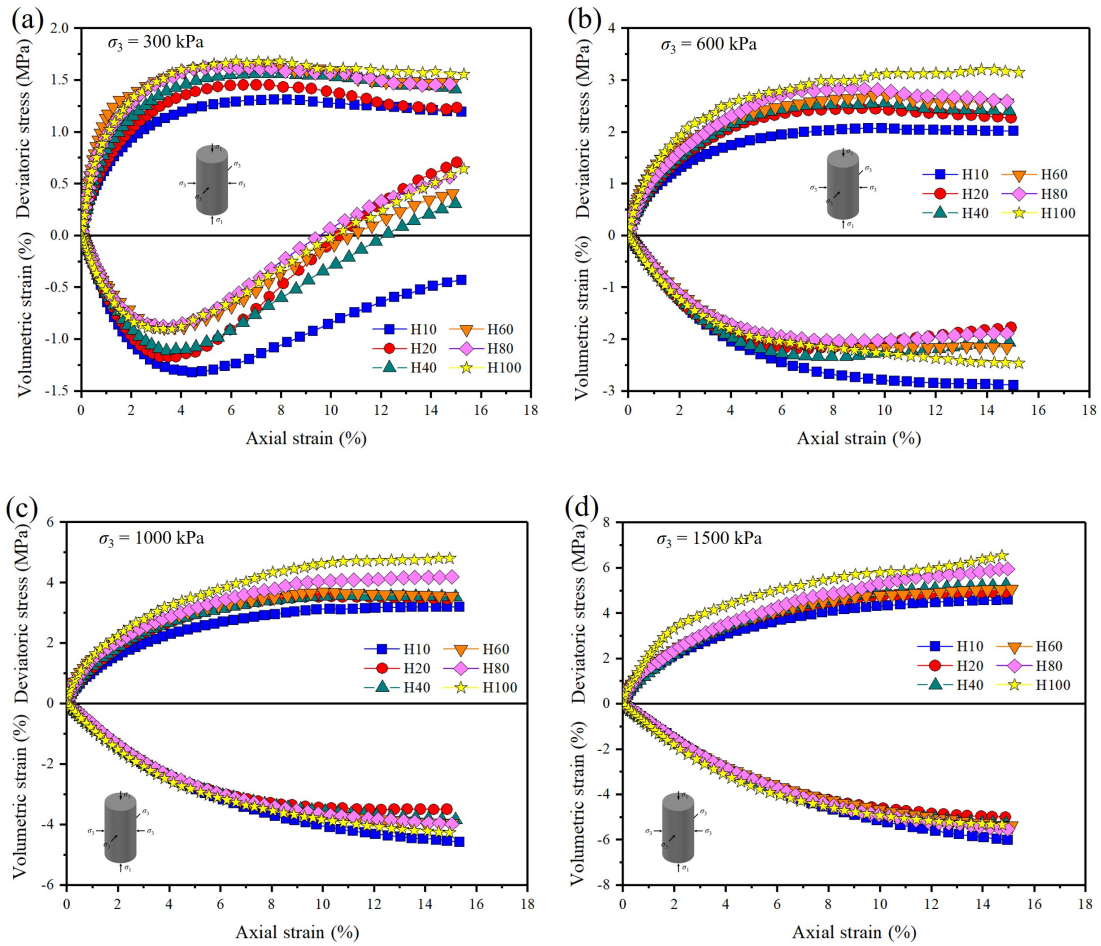


**Figure III .8:** Stress/ volumetric strain-axial strain curves for studied rockfill materials under different confining pressures  $\sigma_3$ : (a) 300 kPa; (b) 600 kPa ; (c) 1000 kPa; (d) 1500 kPa

Fig. III .8 shows the stress-strain relationship of the scaled rockfill materials with six maximum particle sizes  $d_M$ . In general, under low confining pressure (300 kPa), an

important volumetric dilatancy phase and a strain softening phase are observed in all the samples while the samples exhibit a volumetric contraction and a strain hardening phase under high confining pressures (1000 kPa and 1500 kPa). For a given confining pressure  $\sigma_3$ , the deviatoric stress increases with increasing  $d_M$ . On the other hand, no evidence dependence of volumetric strain on the particle size is observed. For instance, H10 exhibits the maximum volumetric strain and the minimum volumetric strain is observed in H20. On the whole, the curves between H20 and H60 is in a relatively narrow band, and the curve shape are similar.

### 5.3 Particle size effect on strength indexes

The relationship between the deviatoric stress at failure  $(\sigma_1 - \sigma_3)_f$  and maximum particle size  $d_M$  is given in Fig. III .9a. The deviatoric stress at failure  $(\sigma_1 - \sigma_3)_f$  increases with increasing  $d_M$ , and the data points can be linearly fitted. According to the fitted lines (dashed lines in Fig. III .9a), it can be inferred that an increase of  $d_M$  by 10 mm could lead to an increase of  $(\sigma_1 - \sigma_3)_f$  by 36.3, 105.0, 156.2 and 194.9 kPa, corresponding to 300, 600, 1000 and 1500 kPa of  $\sigma_3$ , respectively. It can be seen that the slope and intercept of the fitted lines vary with  $\sigma_3$ . Therefore, the relationships between slope, intercept and  $\sigma_3$  are plotted in Fig. III .9b and c, which can also be linearly fitted. Thus,  $(\sigma_1 - \sigma_3)_f$  can be expressed as

$$(\sigma_1 - \sigma_3)_f = \frac{p_a}{100} \left( a_f \frac{d_M}{d_r} + b_f \right) \quad (\text{III .4})$$

where  $a_f$  and  $b_f$  are the material parameters;  $p_a$  = atmospheric pressure, 100 kPa.

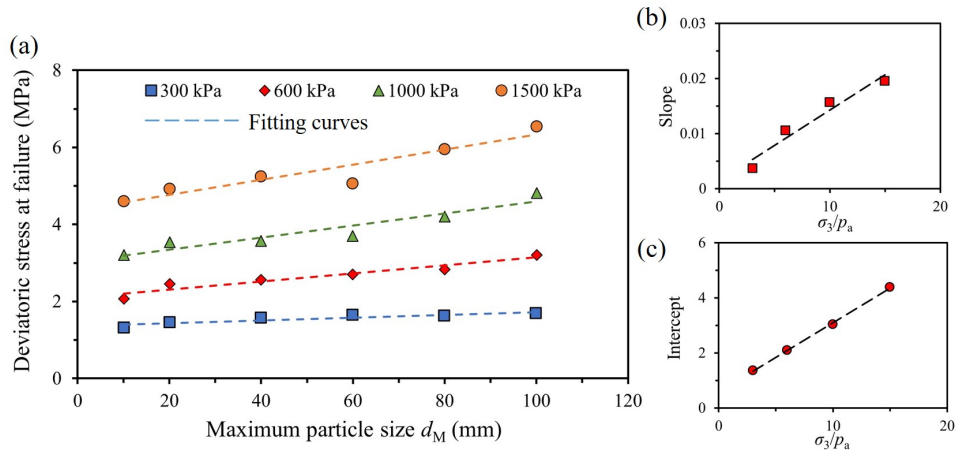


**Figure III .9:** Relation curves related to the deviatoric stress at failure: (a) deviatoric stress at failure  $(\sigma_1 - \sigma_3)_f$  and  $d_M$ ; (b) slope and  $\sigma_3/p_a$ ; (c) intercept and  $\sigma_3/p_a$

Fig. III .10a shows that the deviatoric stress ratio at failure  $(\sigma_1 - \sigma_3)_f/\sigma_3$  decreases with the increase of confining pressure  $\sigma_3$ . Moreover,  $(\sigma_1 - \sigma_3)_f/\sigma_3$  increases with  $d_M$ , and their relationships can also be linearly fitted. It can be obtained that for 300, 600, 1000 and 1500 kPa of  $\sigma_3$ ,  $(\sigma_1 - \sigma_3)_f/\sigma_3$  could increase by 0.12, 0.17, 0.16 and 0.13 with the increment of 10 mm of  $d_M$ .

In triaxial test, the mobilized internal friction angle  $\varphi$  can be calculated as (Marsal, 1967; Varadarajan et al., 2003; Kh et al., 2011):  $\sin \varphi = (\sigma_1 - \sigma_3)/(\sigma_1 + \sigma_3)$ . As shown in Fig. III .10b, under the same confining pressure  $\sigma_3$ , the mobilized internal friction angle at peak  $\varphi_f$  increases with  $d_M$ . For four different values of  $\sigma_3$  (300, 600, 1000 and 1500 kPa),  $\varphi_f$  could increase by  $0.40^\circ$ ,  $0.68^\circ$ ,  $0.68^\circ$  and  $0.61^\circ$  with a  $d_M$  increment of 10 mm.

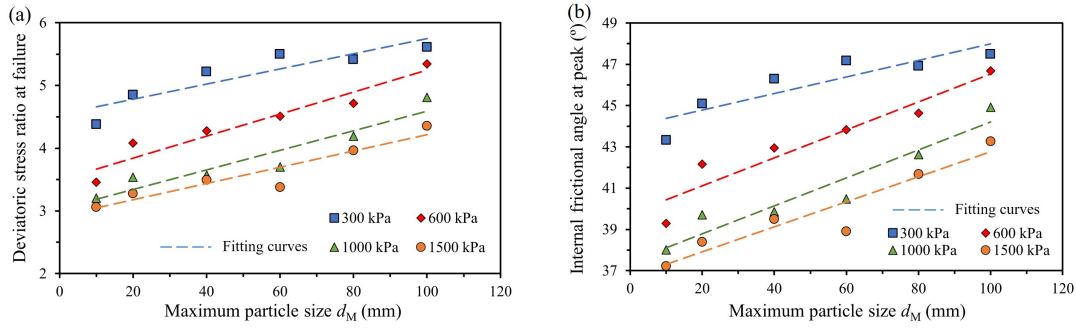


**Figure III .10:** Relationship between (a) deviatoric stress ratio at failure  $(\sigma_1 - \sigma_3)_f/\sigma_3$  and  $d_M$ : (b) mobilized internal friction angle at peak  $\varphi_f$  and  $d_M$

#### 5.4 Particle size effect on deformation indexes

In this section, the secant Young's modulus  $E_1$  and the bulk modulus  $K_1$  are studied.  $E_1$  is determined by using the deviatoric stress  $(\sigma_1 - \sigma_3)$  at 1% axial strain. The  $K_1$  is identified by using the deviatoric stress  $(\sigma_1 - \sigma_3)$  and the volumetric strain  $(\varepsilon_v)$ , i.e.  $K_1 = (\sigma_1 - \sigma_3)/(3\varepsilon_v)$ .

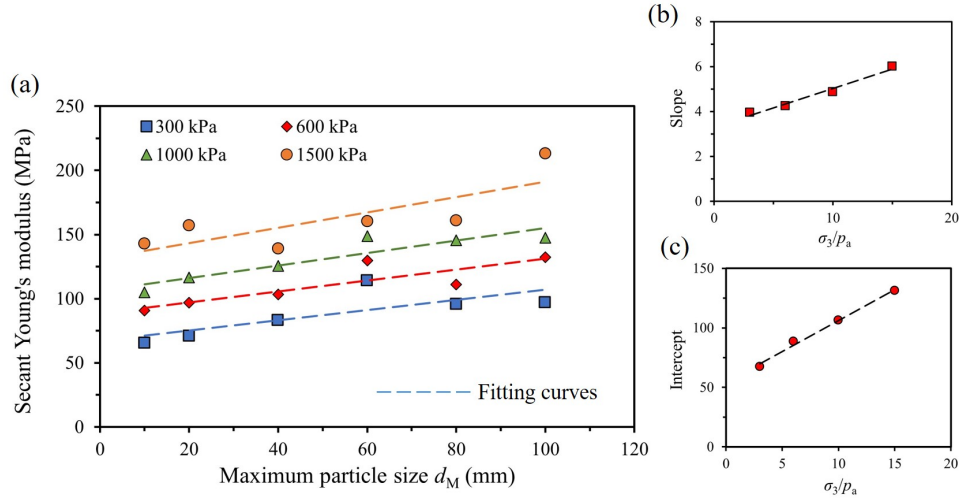


**Figure III .11:** Evolution of secant Young's modulus: (a) secant Young's modulus  $E_1$  and  $d_M$ ; (b) slope and  $\sigma_3/p_a$ ; (c) intercept and  $\sigma_3/p_a$

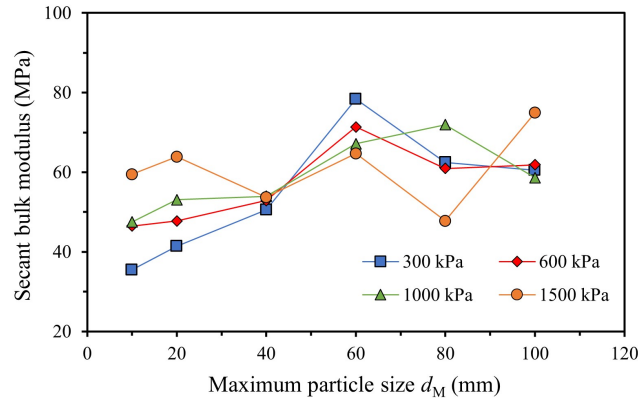


**Figure III .12:** Relationship between bulk modulus  $K_1$  and  $d_M$

As shown in Fig. III .11a, the secant Young's modulus  $E_1$  increases with  $d_M$ , and the data points can be linearly fitted. Based on the fitted line (dashed line in Fig. III .11a), it is observed that  $E_1$  increases by 3.957, 4.243, 4.869 and 6.004 MPa with an increase  $d_M$  of 10 mm, under 300, 600, 1000 and 1500 kPa of  $\sigma_3$ , respectively. The slope and intercept of the fitting lines depends on the applied  $\sigma_3$ , and their relationships are given in Fig. III .9b and c, which can also be linearly fitted. Then,  $E_1$  can be expressed as

$$E_1 = \frac{p_a}{100} \left( a_E \frac{d_M}{d_r} + b_E \right) \quad (\text{III .5})$$

where  $a_E$  and  $b_E$  are the material parameters.

Fig. III .12 presents the relationship between the bulk modulus  $K_1$  and  $d_M$ . No clear

trend is observed in the figures. For instance,  $\sigma_3$  increases with  $K_1$  in tests of H10 and H20, while  $\sigma_3$  decreases with  $K_1$  in the test of H60. This observation is related to the particle breakage. On one hand, the sample under high confining pressures is unlikely to deform due to the less volume of pores. On the other hand, the particle breakage under high confining pressures will cause more irreversible deformation.

### 5.5 Particle size effect on characteristic stress state

When the studied materials deform from volumetric contraction to dilatancy, the critical state is called the phase transition point (Yao et al., 2019), which represents the densest state of rockfill materials. Both the failure strength and phase transition points are two important issues in the study of mechanical behavior of rockfill materials (Liu et al., 2016; Xiao et al., 2016). The stress ratio  $M = q/p$  can be determined by using the mean stress  $p$  and the deviatoric stress  $q$ . Specially, the values of  $p$  and  $q$  are respectively equal to  $(\sigma_1 + 2\sigma_3)/3$  and  $(\sigma_1 - \sigma_3)$  in triaxial tests.

Fig. III .13a shows that the samples have a high value of  $M_f$  under low confining pressure. The stress ratio at failure point  $M_f$  increases with increasing  $d_M$ , and the data can be linearly fitted. Based on the fitted line, it can be estimated that for 300, 600, 1000 and 1500 kPa of  $\sigma_3$ ,  $M_f$  could increase by 0.0017, 0.0290, 0.0290 and 0.0260 with the increment of 10 mm of  $d_M$ .

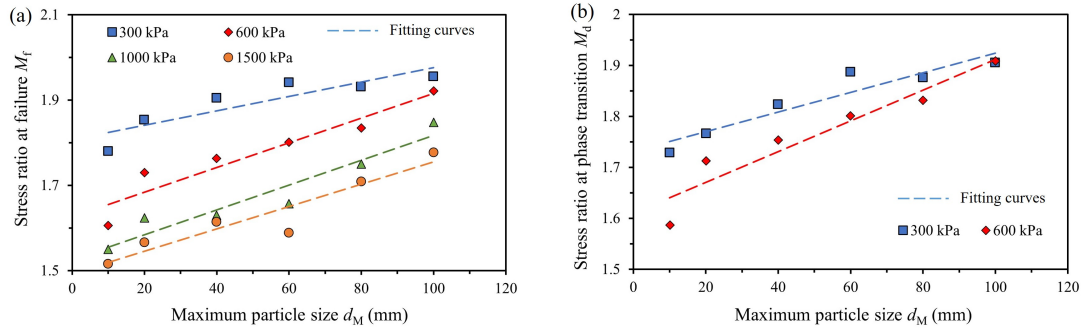


**Figure III .13:** Relation curves related to the characteristic stress state: (a) relationship between  $M_f$  and  $d_M$ ; (b) relationship between  $M_d$  and  $d_M$

The relationship between stress ratio at phase transition (dilatancy stress ratio)  $M_d$  and  $d_M$  is shown in Fig. III .13b. Because dilatancy is only observed under low confining pressures (300 and 600 kPa), the data of  $M_d$  only at these two confining pressures is plotted. It can be seen that  $M_d$  increases with the increase of  $d_M$ .  $M_d$  increases by 0.0019 and 0.0030 with the increment of 10 mm of  $d_M$  for 300 and 600 kPa of  $\sigma_3$ .

## 6 Discussion

### 6.1 Fractal behavior

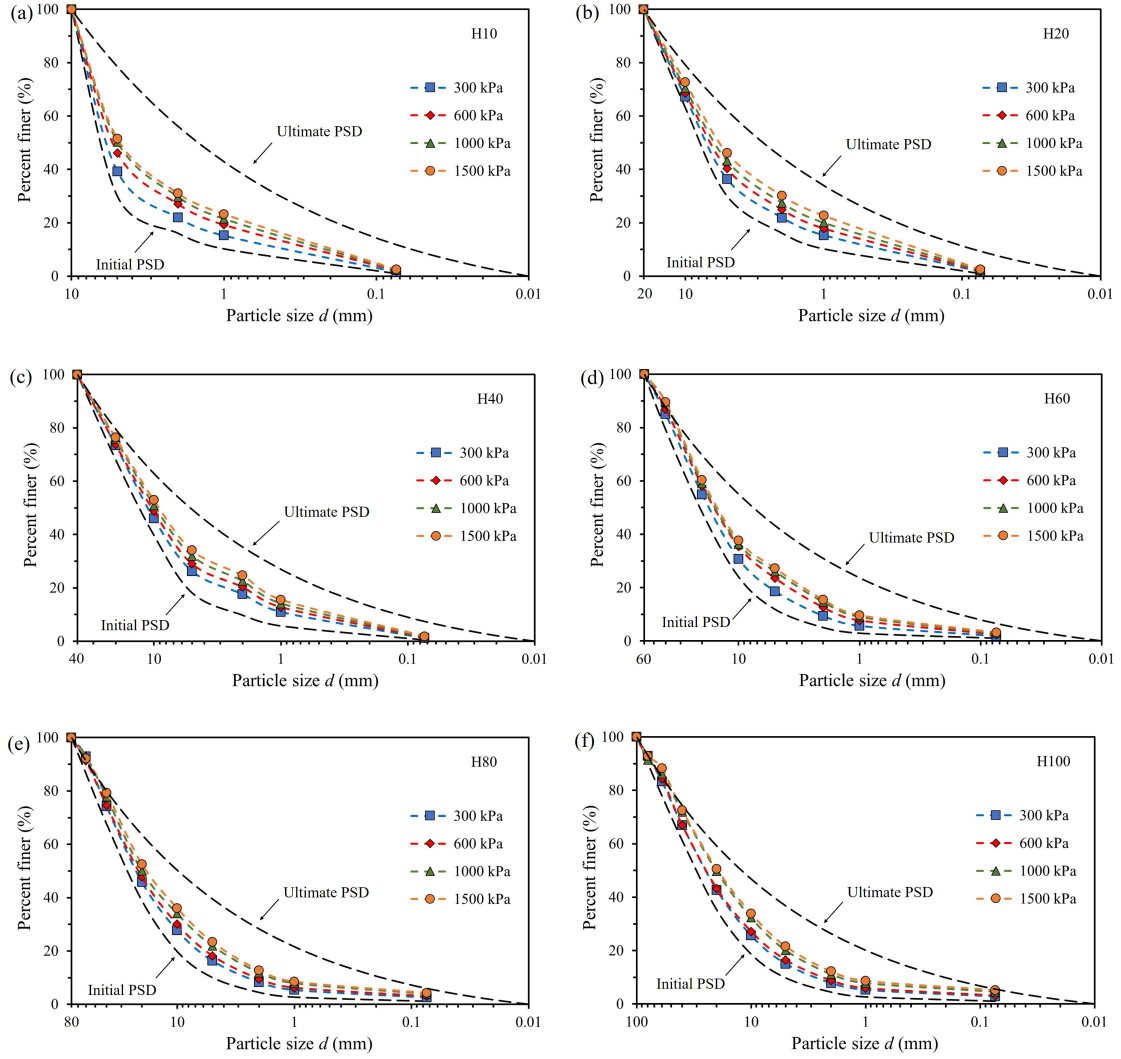
Due to the successive breakage, the particle size evolves progressively towards to the ultimate PSD . For the samples with different  $d_M$ , the final particle size distribution curves obtained under different confining pressures are given in Fig. III .14. The grading curves shift rightward as the confining pressure  $\sigma_3$  increases, indicating that the occurrence of particle crushing increases with  $\sigma_3$ . This observation is consistent with previous laboratory tests (Gupta, 2016; Wang et al., 2021; Xiao et al., 2014b).

Fig. III .15 shows the correlations between the percentage finer and normalized particle size, i.e.,  $d/d_M$ . For a sample with a given  $d_M$ , the initial PSD curves are similar, except for the PSD with  $d_M = 10$  mm (Fig. III .15g). Moreover, for  $\sigma_3 = 1500$  kPa, one observes that the final PSDs with different  $d_M$  are distributed within a narrow band (Fig. III .15h), indicating that the fractal dimension emerges. According to the research works of Tyler & Wheatcraft (1989), the fractal grading can be described as

$$F_u(d) = \left(\frac{d}{d_M}\right)^{3-D} \quad (\text{III .6})$$

where  $F_u(d)$  is the percentage finer,  $d_M$  is the largest particle size and  $D$  is the fractal dimension. The fractal dimension  $D$  is usually in the range of  $2.0 \sim 3.0$  for the granular materials in compression (de Bono and McDowell, 2016b). Inspired by the research works of Xiao et al.(2020) and Wang et al. (2021) ,  $D = 2.7$  can be taken for RFM. By comparing the Figs. III .15g and h, it can be seen that the PSDs evolve towards to the ultimate one in triaxial tests. Additionally, the left-hand section of the final PSDs of  $\sigma_3 = 1500$  kPa ( $d/d_M$  ranges from 1 to 0.6) almost reaches the ultimate PSD line.





**Figure III .14:** Particle size distribution after compression for samples under different confining pressures. (a)  $d_M = 10$  mm; (b)  $d_M = 20$  mm; (c)  $d_M = 40$  mm; (d)  $d_M = 60$  mm; (e)  $d_M = 80$  mm; (f)  $d_M = 100$  mm



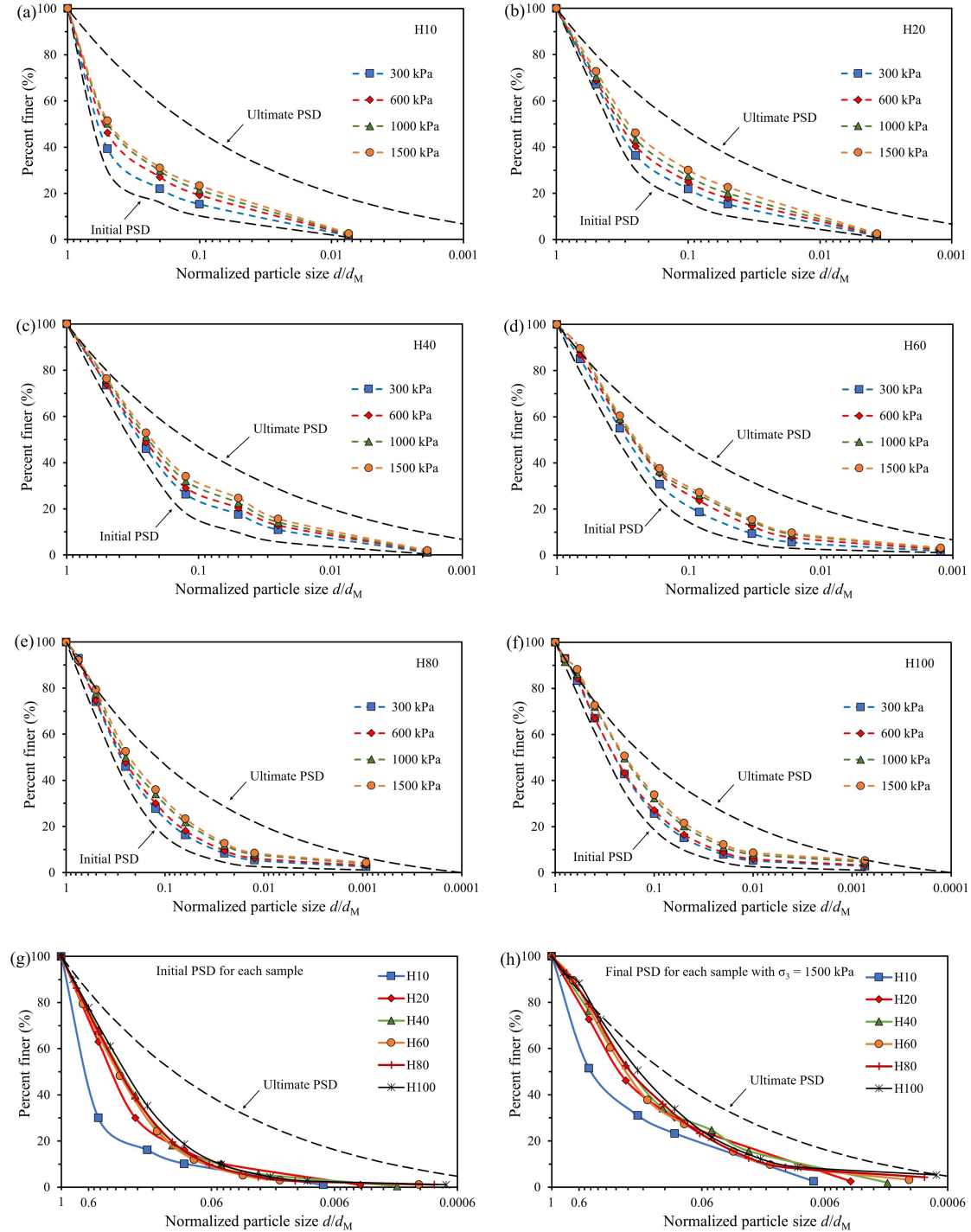


**Figure III .15:** Correlations between the percentage finer and normalized particle size. (a)  $d_M = 10$  mm; (b)  $d_M = 20$  mm; (c)  $d_M = 40$  mm; (d)  $d_M = 60$  mm; (e)  $d_M = 80$  mm; (f)  $d_M = 100$  mm; (g) comparison of initial particle size distributions with different  $d_M$ ; (h) comparison of final particle size distribution with different  $d_M$  under the confining pressure of 1500 kPa

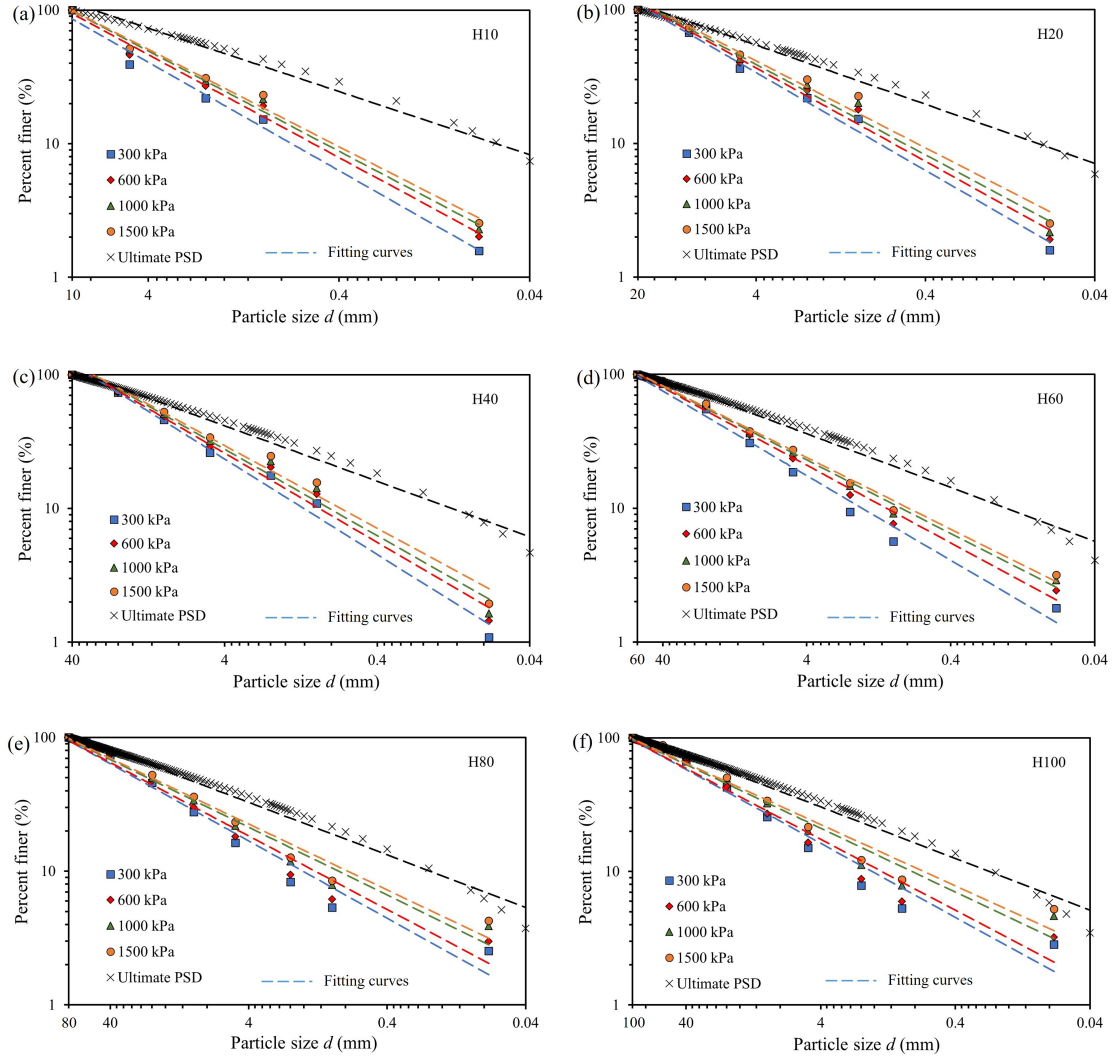


**Figure III .16:** Particle size distribution in the samples under different confining pressures on a double logarithmic plot. (a)  $d_M = 10$  mm; (b)  $d_M = 20$  mm; (c)  $d_M = 40$  mm; (d)  $d_M = 60$  mm; (e)  $d_M = 80$  mm; (f)  $d_M = 100$  mm

The experimental data of Figs. III .14 and III .15 is redrawn with the log-log scales in Figs. III .16 and III .17, respectively. For a given  $d_M$ , the experimental data under different confining pressure can be fitted by using Eq. (III .6). Figs. III .16 and III .17 show that the right-hand sections of the fitted lines shift upward with increasing confining pressures  $\sigma_3$ . This observation is due to the accumulation of finer fractions as  $\sigma_3$  increases. The linear fitting curves in Figs. III .16 and III .17 agree well with the test data, especially under high confining pressures (Fig. III .17h).

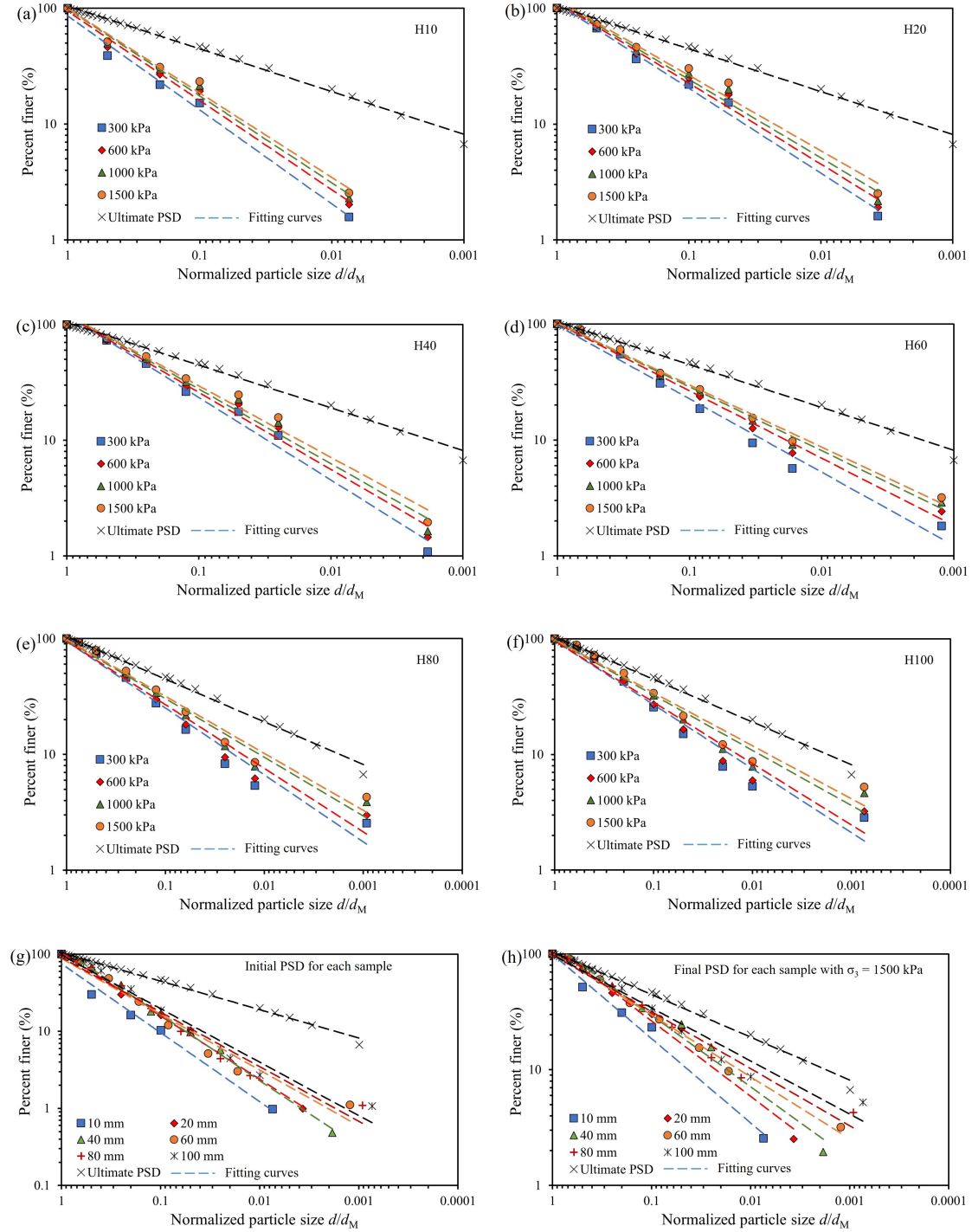


**Figure III.17:** Correlations between the percentage finer and normalized particle size on a double logarithmic plot. (a)  $d_M = 10$  mm; (b)  $d_M = 20$  mm; (c)  $d_M = 40$  mm; (d)  $d_M = 60$  mm; (e)  $d_M = 80$  mm; (f)  $d_M = 100$  mm; (g) comparison of initial particle size distributions for different  $d_M$ ; (h) comparison of final particle size distribution for different  $d_M$  under the confining pressure of 1500 kPa

Figs. III .17g and h show that the slope decreases with increasing  $d_M$  for both initial and final PSDs of  $\sigma_3 = 1500$  kPa, indicating a correlation between  $d_M$  and fractal dimension  $D$ . Hence, the relationship between  $D$  and  $d_M$  is given in Fig. III .18. The experimental data can be linearly fitted and the obtained fitting curves are parallel with each other. For the samples with  $d_M = 10$  mm, the fractal dimension  $D$  ranges from 2.1 to 2.3, which is still far from the ultimate value 2.7. Comparatively, the fractal dimension of samples with  $d_M = 100$  mm is closer to the ultimate value ( $2.3 \sim 2.5$ ).

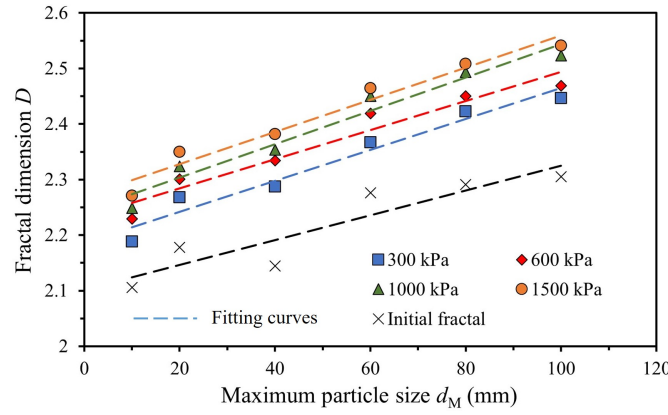


**Figure III .18:** Relationship between the fractal dimension and  $d_M$

## 6.2 Relative particle breakage

In section 6.1, it is confirmed that the particle breakage in triaxial tests leads the PSD curve to fractal one. Laboratory results present that the effects of particle size on the mechanical behavior of studied rockfall material is closely related to the particle breakage (Gupta, 2016; Frossard et al., 2012). Therefore, it is necessary to quantitatively identify the particle breakage. According to the change of the PSD before and after tests, various particle breakage indexes have been proposed (Marsal, 1967; Hardin, 1985; Lade et al., 1996; Einav, 2007). Based on the work of Hardin (1985), the relative breakage index  $B_r$  modified by Einav (2007) and shown in Fig. III .19 is adopted in the present work:

$$B_r = \frac{B_t}{B_p} \quad (\text{III .7})$$

where  $B_t$  is the total breakage, i.e., the area between initial and current PSD, and  $B_p$  is the breakage potential, i.e., the area between initial and ultimate PSD. Xiao et al. (2015)

proposed a simplified equation to calculate the relative breakage index:

$$B_r = \frac{(D_c - D_0)(3 - D_u)}{(D_u - D_0)(3 - D_c)} \quad (\text{III .8})$$

where  $D_0$  is the initial fractal dimension,  $D_c$  is the current fractal dimension and  $D_u$  is the ultimate fractal dimension.

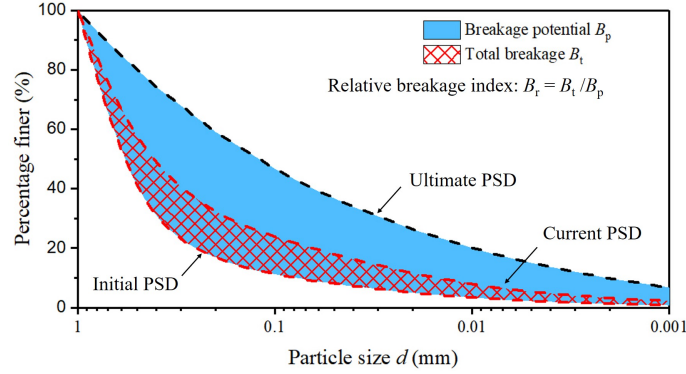


**Figure III .19:** Definition of the relative breakage index

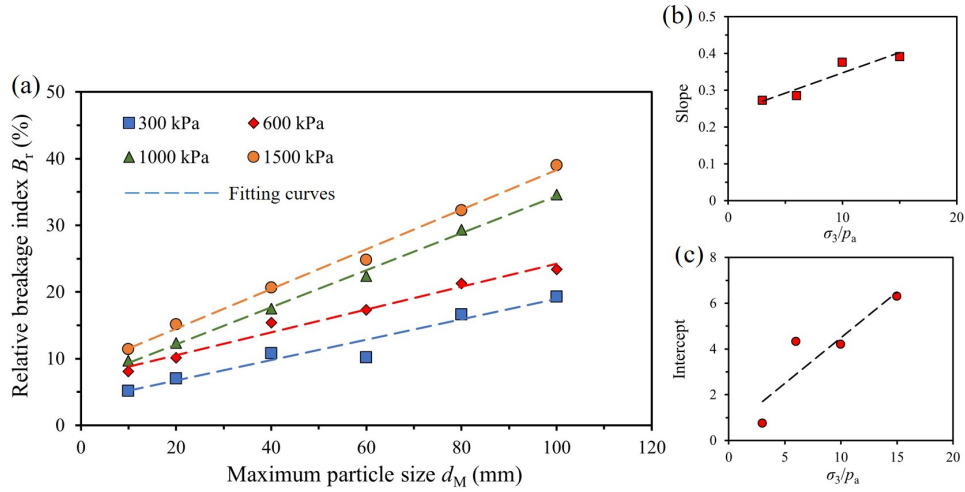


**Figure III .20:** (a) Evolution of relative breakage  $B_r$  in function of  $d_{max}$ ; (b) relationship between slope and  $\sigma_3/p_a$ ; (c) relationship between intercept and  $\sigma_3/p_a$

Fig. III .20a shows the relationship between the relative breakage index  $B_r$  and maximum particle size  $d_M$  on RFM samples under different confining pressures  $\sigma_3$ .  $B_r$  increases with  $d_M$ , and their relationship can be linearly fitted. It can then be estimated that  $B_r$  increase by 2.72%, 2.85%, 3.77% and 3.91% with an increase of 10 mm of  $d_M$ , with the  $\sigma_3 = 300, 600, 1000$  and  $1500$  kPa. Note that the slope and intercept of fitted curves also

vary with  $\sigma_3$ . The relationships between slope, intercept and  $\sigma_3$  are plotted in Fig. III.20b and c, which can also be linearly fitted. Then,  $B_r$  can be expressed as

$$B_r = a_B \frac{d_M}{d_r} + b_B \quad (\text{III .9})$$

where  $a_B$  and  $b_B$  are the material parameters.

## 7 Conclusions

In this chapter, single crushing have been conducted on three groups of particle size while dry density and drained triaxial tests have been conducted on Shuang-Jiang-Kou RFM with six maximum particle sizes  $d_M$ . The effects of particle size on the crushing of particle and mechanical behavior of studied rockfill materials are analyzed. The main conclusions can be summarized as follows:

(1) Single-particle crushing tests show that the breakage of rockfill particles is a brittle failure. The particles are generally broken into 2 or 3 main pieces. The peak force increases with increasing particle size.

(2) Dry density test results show that both the minimum and maximum dry densities of RFM increase with increasing  $d_M$ . An empirical equation considering the gradation and  $d_M$  is proposed to predict the dry density of prototype RFM by introducing a normalized parameter  $\lambda$ . A simple verification of experimental results are also performed via a DEM simulation.

(3) In the triaxial tests, an important difference is observed in the stress-strain curves with different  $d_M$  under low confining pressure (300 kPa). Both the mobilized internal friction angle at peak  $\varphi_f$  and the secant Young's modulus  $E_1$  increase with the increase of  $d_M$ . Moreover, the stress ratio at failure  $M_f$  and at phase transition  $M_d$  increases with increasing  $d_M$ .

(4) Particle size distribution (PSD) presents a fractal behavior in triaxial tests and the fractal dimension of 2.7 can be used to describe the ultimate PSD. The fractal dimension increases with increasing  $d_M$ . Relative breakage index  $B_r$  is used for the identification of particle breakage.  $B_r$  increases with increasing confining pressure and  $d_M$ , and their relationship can be described by a linear line.



## Chapter IV

# Influence of particle size on the breakage characteristics of rockfill particles in single-particle crushing tests

### 1 Introduction

Thanks to their high local availability, low cost and high strength, rockfill materials (RFM) are widely used in the construction of dams. Under the high stress created in rockfill dams, rockfill particles may be broken. The particle breakage induces the settlement and an eventual rearrangement of grains. As a result, it has an important impact on the strength, deformation and hydraulic conductivity of rockfill dams (Alonso et al., 2012; Brzesowsky et al., 2011; Cil and Alshibli, 2012, 2014a; de Bono, 2013; Deluzarche and Cambou, 2006; Huang et al., 2020; Kh et al., 2011; Lade et al., 1996; Stoeber, 2012; Wang and Yan, 2013; Xiao et al., 2015; Zhao et al., 2015). In view of this, the durability of rockfill dams requires a good understanding of breakage characteristics of RFM.

In the present work, the breakage characteristics of rockfill particles with different sizes are investigated via a series of single-particle crushing tests, theoretical analysis and numerical simulations. Single-particle crushing tests are firstly performed (given in chapter III). In order to identify the size effects on the particle strength and breakage of studied material, the obtained results are analysed by using the Weibull model and DEM simulations. The bonded particle model (BPM) parameters in YADE are calibrated



against the force-displacement curve obtained in the laboratory test. The particle breakage strength predicted by the BPM model is then verified by the Buckingham theorem. Finally, single-particle crushing tests with different agglomerate sizes, flaw sizes, flaw numbers and flaw volume ratios are simulated and analysed.

## 2 Weibull statistical analysis of single-particle crushing tests

The failure of brittle materials is quite different from that of ductile ones (Xiao et al., 2020; McDowell and Humphreys, 2002). In addition, due to the presence of pores and internal defects (such as micro cracks, confined air bubbles and impurities), the obtained breakage strengths of particles are so different one from another that a statistical function is necessary to describe the distribution of particle breakage strength (Rozenblat et al., 2011). In 1951, Weibull statistical distribution theory (Weibull, 1951) has been used to describe the variation of the particle breakage strength of brittle materials (Billam, 1972; Sullivan and Lauzon, 1986), e.g., ceramics. Nakata et al. (1999) and McDowell & Amon (2000) confirmed that for the sand particles in a range of sizes, the measured particle breakage strength followed the Weibull distribution. Lim et al. (2004) showed that the breakage strength of railway ballast also followed the Weibull distribution. Recently, some researchers (Huang et al., 2020; Xiao et al., 2020; Zhou et al., 2016) have used the Weibull distribution to describe the breakage strength of rockfill particles. In this section, the breakage strength of rockfill particles obtained in single-particle crushing tests is firstly analysed by the Weibull theory. After that, the particle size effects on the characteristic strength of studied rockfill particles are investigated with the aid of Weibull model.

### 2.1 Weibull distribution for brittle materials

In the Weibull theory (Weibull, 1951), the solid is assumed as a chain consisting of several links. Moreover, the larger size the solid has, the more links it possesses. As a result, high failure probability is observed in the large sample with more links.

The survival probability  $P_s(V_0)$  for a block of material with the volume  $V_0$  under a tensile stress  $\sigma$  can be given by

$$P_s(V_0) = \exp\left[-\left(\frac{\sigma}{\sigma_0}\right)^m\right] \quad (\text{IV .1})$$

where  $\sigma_0$ , called the characteristic strength, is equal to the tensile strength of studied material when 37% of these specimens survive. The Weibull modulus  $m$  characterizes

the variation of obtained results and increases with decreasing the variability of material strength (Fig. IV .1).

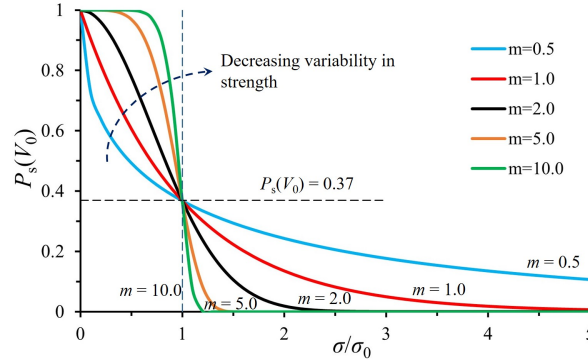


**Figure IV .1:** Survival probability- material strength curves with different values of Weibull modulus  $m$

If the number of tested grain samples is  $N$ , the survival probability  $P_s$  for each sample can be calculated by using the rank of samples arranged by its breakage strength in ascending order  $i$  (Huang et al., 2020; Zhou et al., 2016; Lim et al., 2004):

$$P_s(V_0) = 1 - \frac{i}{N + 1} \quad (\text{IV .2})$$

The Eq. (IV .1) can be rewritten as follows

$$\ln(\ln(1/P_s)) = m \ln \sigma - m \ln \sigma_0 \quad (\text{IV .3})$$

The Weibull modulus  $m$  can be determined by plotting  $\ln(\ln(1/P_s))$  against  $\ln \sigma$ , which is the slope of the fitting line. The characteristic strength  $\sigma_0$  is the value of  $\sigma$  when  $\ln(\ln(1/P_s)) = 0$ .

## 2.2 Validation of Weibull distribution

In the single-particle crushing tests, the tensile stress  $\sigma$  is defined by Jaeger (1967) as

$$\sigma = \frac{F}{d^2} \quad (\text{IV .4})$$

where  $d$  is the distance between two platens during the test and  $F$  is the applied force.

By using Eq. (IV .4), the stress-strain curves of studied particles can be obtained (Fig. IV .2). Note that the particle breakage strength  $\sigma_f$  is the peak stress, which represents the global failure of grain. The value of  $\sigma_f$  generally increases with decreasing particle

size. For instance, in Fig. IV .2A,  $\sigma_f$  of the No.1 particle drops from 11.81 MPa to 5.63 MPa with the increase of  $d_{int}$  from 5 ~ 10mm to 20 ~ 40mm.  $\sigma_f$  of the No.15 particle in Fig. IV .2B drops from 9.39 MPa to 5.26 MPa with the increase of  $d_{int}$  from 5 ~ 10mm to 20 ~ 40mm.

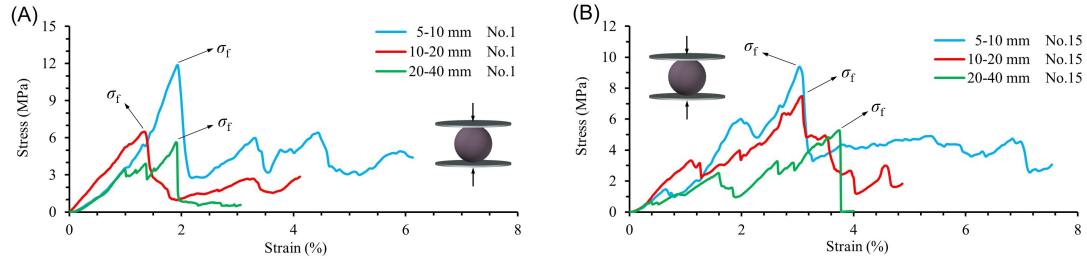


**Figure IV .2:** Typical stress-strain curves of single-particle crushing tests obtained with three size categories of samples: (A) Particle No.1; (B) particle No.15

The survival probability distributions for three size classes of samples are given in Fig. IV .3. The coefficient  $R^2$  of 0.95 ~ 0.99 demonstrates that the obtained test data follows satisfactorily the Weibull statistical distribution. The obtained values of Weibull modulus  $m$  are very close to each other:  $m = 3.53$  for the particles of 5 ~ 10 mm,  $m = 3.89$  for the particles of 10 ~ 20 mm and  $m = 2.43$  for the particles of 20 ~ 40 mm. The mean value of 3.29 can be adopted for the studied material. This value of  $m$  is coherent with the previous results obtained for railway ballast particles (Lim et al., 2004) and rockfill particles (Huang et al., 2020; Xiao et al., 2020; Zhou et al., 2016).

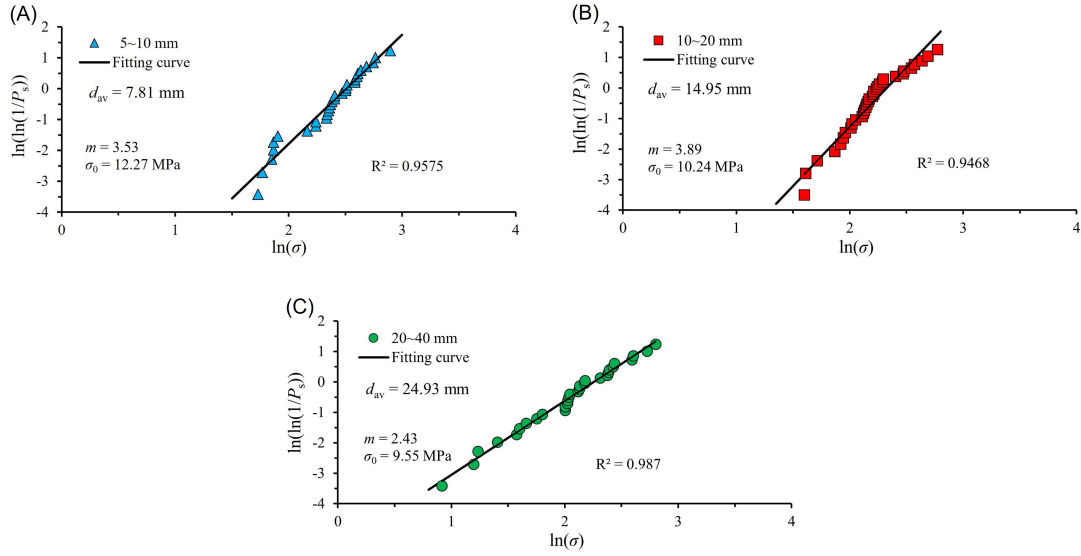


**Figure IV .3:** Weibull distribution plots for single-particle crushing tests of three size categories: (A) 5 ~ 10 mm; (B) 10 ~ 20 mm; (C) 20 ~ 40 mm

The survival probability at a given tensile stress level is given in Fig. IV .4A. An increase of survival probability is generally observed when the particle size decreases. Moreover, the characteristic strength  $\sigma_0$  decreases with increasing particle size (Fig. IV .3). For instance,  $\sigma_0$  decreases from 12.27 MPa to 9.55 MPa when  $d_{av}$  increases from 7.81 mm to 24.93 mm. These observations are related to the size effects on the breakage strength of rockfill particles, which will be discussed in section 2.3. On the other hand, the survival probability  $P_s$  versus the normalized tensile stress  $\sigma_f/\sigma_0$  curves are given in Fig. IV .4B. Three curves are found in a narrow band, indicating that the normalized single-particle strength is independent of particle size. A constant Weibull modulus  $m$  can then be applied for the studied rockfill particles. As a result,  $m$  can be considered as a material parameter, describing the strength distribution (Nakata et al., 1999; Zhou et al., 2016; Lobo-Guerrero and Vallejo, 2006a; McDowell, 2002; Ovalle et al., 2014).

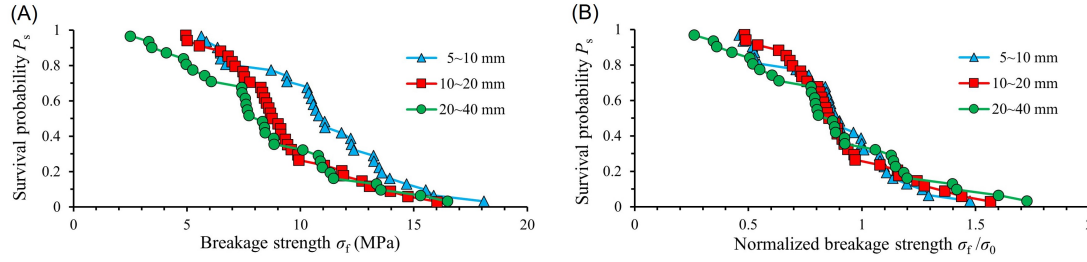


**Figure IV .4:** Comparison of the survival probability at a given tensile strength for three groups of particles. (A) breakage strength; (B) normalized tensile strength

### 2.3 Particle size effects on the tensile strength of studied rockfill materials

The obtained experimental results exhibit that the characteristic strength  $\sigma_0$  decreases with the increase of particle size (Fig. IV .3). In practice, similar results have been gotten in some natural particles, e.g., sand, railway ballast and rock aggregate (de Bono, 2013; Wang and Yan, 2013; Nakata et al., 1999; Zhou et al., 2016; Jansen and Stoyan, 2000; Lobo-Guerrero and Vallejo, 2006a; Nakata et al., 2001b; Drlik, 1987; Lee, 1992; Lim et al., 2004; McDowell, 2002; McDowell and Amon, 2000; Rozenblat et al., 2011; Shao et al., 2020; Zhong et al., 2014).

To describe the dependence of the characteristic strength  $\sigma_0$  on the particle size  $d$ , Lee (1992) proposed the following relation

$$\sigma_0 = k\sigma_{ref}\left(\frac{d}{d_{ref}}\right)^b \quad (\text{IV .5})$$

where  $\sigma_{ref}$  is the characteristic (tensile) strength of the referenced particle with a given size  $d_{ref}$ ;  $b$  controls the particle size effects on the tensile strength and is typically a negative number in the order of -1 to -0.1 (Wang and Arson, 2016);  $k$  and  $b$  are the fitting parameters, which describe the size-hardening law (Lim et al., 2004). According to the particle size  $d$ , two values are generally adopted in the literature: the initial particle size  $d_{int}$  (Zhou et al., 2016; Nakata et al., 2001b) and the particle size at failure  $d_f$  (Lim et al., 2004). By using the Eq. (IV .5), the relationship between  $\sigma_0$  and the particle size is shown in Fig. IV .5A. Two series of calculation have been performed by using  $d_{int}$  and  $d_f$ , respectively. It can be seen that two fitting curves are almost the same (Fig. IV .5A). Consequently, both  $d_{int}$  and  $d_f$  are capable of describing the particle size effects on the characteristic strength of studied rockfill particles. In the present work,  $d_{int}$  is used in the present work.

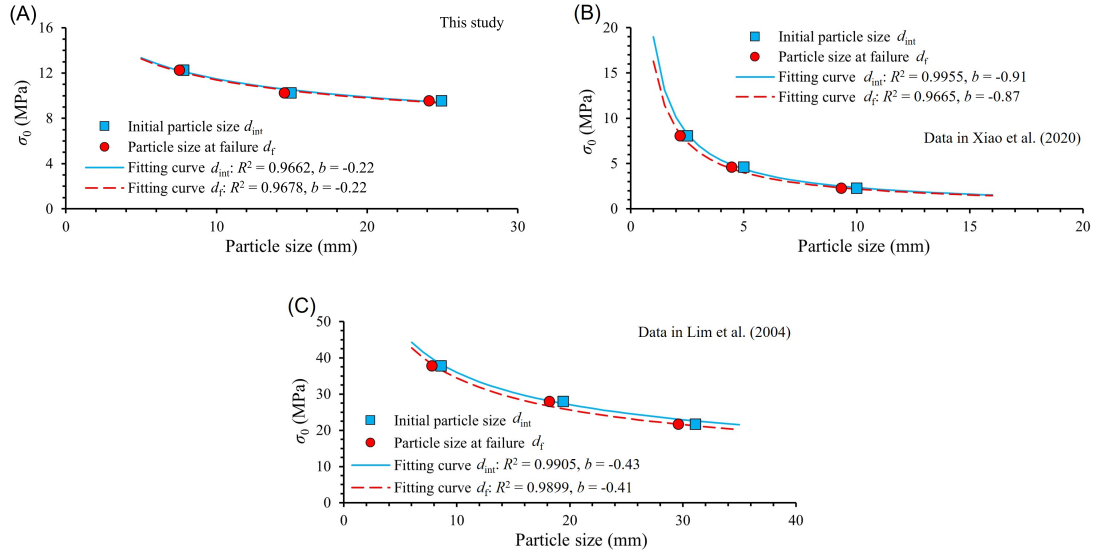


**Figure IV .5:** Evolution of the characteristic strength  $\sigma_0$  in function of the initial particle size  $d_{int}$ /the particle size at failure  $d_f$ . (A) Rockfill materials studied in the present work; (B) sandstone studied in Xiao et al. (2020); (C) ballast studied in Lim et al. (2004)

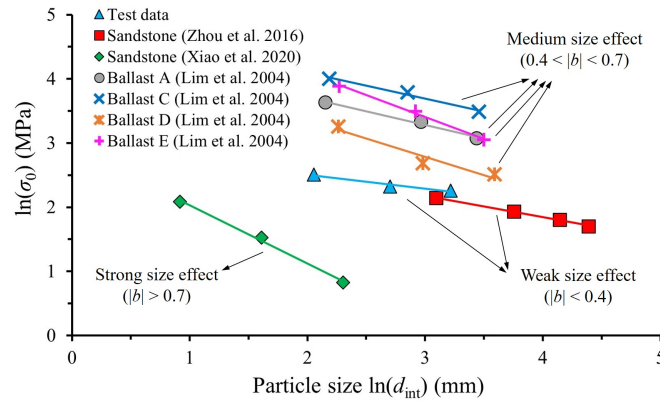


**Figure IV .6:** Comparison of the particle size effects on characteristic strength between studied rockfill materials and other rock materials presented in the literature

In order to get a general vision on the particle size effects on characteristic strength of studied rockfill particles, the experimental results of two other types of rocks found in the literature are also presented in Fig. IV .5B,C. By comparing the fitting curves presented in Fig. IV .5, it can be found that the dependence of characteristic strength on the particle size is not the same. Three different values of  $b$  are determined for three types of rock particles. For instance, for the studied rockfill particles (Fig. IV .5A), the value of  $b = -0.22$  is obtained and a weak size effect is observed. On the other hand, the

sandstone (Fig. IV .5B) exhibits a strong size effect with  $b = -0.91$ , and the ballast (Fig. IV .5C) has a medium size effect with  $b = -0.43$ . More test data in the literature fitted by Eq. (IV .5) is plotted in Fig. IV .6. The slope of each fitted line represents the value of the size effect parameter  $b$ . The obtained value of  $b$  for studied RFM is similar to that for the RFM analysed by Zhou et al (2016). According to the absolute values of  $b$ , the rock particles can be roughly divided into three groups: weak size effect ( $|b| < 0.4$ ), medium size effect ( $0.4 < |b| < 0.7$ ) and strong size effect ( $|b| > 0.7$ ).

In order to describe the particle size effects of geomaterials with the Weibull distribution, McDowell & Amon (2000) proposed that  $\sigma_0$  is a function of the particle size  $d$  as

$$\sigma_0 \propto d^{-3/m} \quad (\text{IV .6})$$

Eq. (IV .6) is applied in the rockfill particles with two conditions: all the particles have the similar shape and the particle failure is caused by the tensile stress. This function has been verified by the experimental tests of Quiou sand (McDowell and Amon, 2000). However, Lim et al. (2004) found that the size effect parameter  $b$  for the ballasts was less than  $-3/m$ . They explained that this difference was due to the heterogeneity and anisotropy structure of the studied material. Moreover, they found that the particle breakage was dominated by the surface fracture, not the bulk fracture. Therefore, Lim et al. (2004) developed the following equation

$$\sigma_0 \propto d^{-2/m} \quad (\text{IV .7})$$

For the particles presented in Fig. IV .6, the obtained values of  $b$ ,  $m$ ,  $-3/m$  and  $-2/m$  are summarized in Table IV .1. By comparing the values of  $b$  and  $-3/m$ , a big difference is observed in most cases, except the sandstone used by Xiao et al (2020). This phenomenon confirms again that the failure of particle is not essentially controlled by the bulk fracture. On the other hand, the values of  $-2/m$  are closer to the values of  $b$  with respected to the values of  $-3/m$ . However, for the syenogranite studied in the present work and the ballast D (Lim et al., 2004), the values of  $b$  and  $-2/m$  are quite different from each other. This difference is related to several phenomena: the distribution of flaws, the non-similarity of particle shape (Nakata et al., 1999), or the heterogeneity, the anisotropy, and the variation of mineral proportion of the particles (Lim et al., 2004). In conclusion, when the values of  $b$  can not be determined directly,  $-2/m$  is more reasonable for the estimation of  $b$  and the size-hardening law of rockfill particles can then be analysed by the Eq. (IV .5).

The previous experimental results exhibit that the particle breakage strength of studied

**Table IV .1:** Theoretical analysis of particle size effects on the characteristic strength of different materials

Material	Average $m$	$b$	$-3/m$	$-2/m$
Syenogranite (test data)	3.29	-0.22	-0.91	-0.61
Sandstone (Xiao et al. (2020))	3.24	-0.91	-0.93	-0.62
Sandstone (Zhou et al. (2016))	4.53	-0.34	-0.66	-0.44
Ballast A (Lim et al. (2004))	3.42	-0.43	-0.88	-0.58
Ballast C (Lim et al. (2004))	3.09	-0.40	-0.97	-0.65
Ballast D (Lim et al. (2004))	2.06	-0.57	-1.46	-0.97
Ballast E (Lim et al. (2004))	3.25	-0.68	-0.92	-0.62

RFM decreases with increasing particle size (Fig. IV .2). This observation is generally explained by the fact that large particles have more and bigger flaws than small particles (Alonso et al., 2012; Lade et al., 1996; Drlik, 1987; Zhong et al., 2014; Frossard et al., 2012; Hardin, 1985; Liu et al., 1998). In other words, the number and size of flaws in one particle is proportional to its size (Fig. IV .7). In practice, such as sand and rockfill, small particles are generally gotten by breaking large particles along their internal defects (Fig. IV .7). As a result, there are few and small flaws in the small particles (Lade et al., 1996). Moreover, the small particles, created by the boundary breakage, may be composed of one single mineral and exhibit a strong, homogeneous internal structure (Fukumoto and Hara, 1998). In conclusion, the combination of few and small flaws and a more homogeneous structure results in the high strength of small particles. Although this conclusion has been partially verified by  $\mu$ CT scanning and few DEM simulations (Zhao et al., 2015; Wang and Arson, 2016), the microscopic origins of particle size effects on the breakage characteristics of RFM are still under research. In the following, several possible issues of particle size effects will be analysed via a series of DEM simulations.



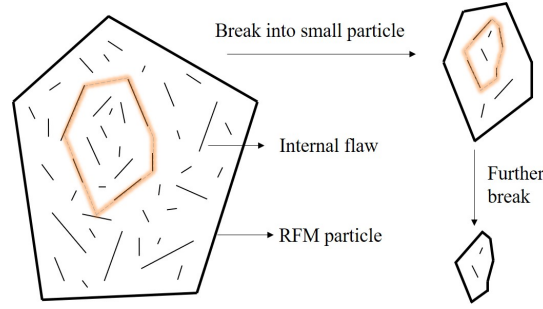


**Figure IV .7:** Different samples collected from the same parent material

### 3 DEM modelling of particle size effects

#### 3.1 Constitutive model used in Yade

In the numerical simulation, the crushable particle is represented as a spherical agglomerate of bonded and hexagonally packed particles ("balls"). The balls are equally sized and non breakable. Agglomerate crushing is modelled as bond breakage. According to two rigid platens, used in the crushing test, they are made up of rigid "facet" units. The simulations are performed with YADE, an open source framework for numerical models using the discrete element method (DEM) (Kozicki and Donze, 2008, 2009). In YADE, rigid "balls" and rigid "facets" are allowed to overlap with a contact area which is negligible with respect to the ball size. Two models are used in the simulations: a linear contact model and a bond model.

The relationship between the force and the relative displacement is given as

$$\begin{aligned}\vec{F}^n &= k^n u^n \vec{n} \\ \vec{F}^s &= \sum \Delta \vec{F}^s \\ \Delta \vec{F}^s &= -k^s \Delta \vec{u}^s\end{aligned}\tag{IV .8}$$

where  $\vec{F}^n$ ,  $\vec{F}^s$  and  $\Delta \vec{F}^s$  are respectively the normal contact force, tangential (shear) contact force and tangential contact force increment;  $k^n$  and  $k^s$  are respectively the normal and tangential contact stiffnesses;  $u^n$  and  $\vec{n}$  denote respectively the normal overlap between two balls in contact and the normal contact vector;  $\Delta \vec{u}^s$  is the tangential component of the increment of contact displacement. As the contact stiffness is dependent on the ball size, the model's prediction is independent of its resolution as long as the sample has enough balls and can be regarded as a representative elementary volume (REV) of granular material. The contact stiffnesses  $k^n$  and  $k^s$  of the  $i$ th ball with radius  $R_i$  can be

given as follows

$$\begin{aligned} k_i^n &= 2ER_i \\ k_i^s &= \nu k_i^n \end{aligned} \quad (\text{IV .9})$$

where  $E$  is the nominal Young's modulus and  $\nu$  is the nominal Poisson's ratio. It should be noted that these two parameters cannot be determined directly by using the macro properties of studied material.

The linear contact model is used to govern the contact-interaction between facets and balls. A Mohr-Coulomb criterion is adopted in the linear spring model

$$\begin{aligned} |\vec{F}^s| &\leq \mu |\vec{F}^n| \\ \mu &= \min(\mu_1, \mu_2) \end{aligned} \quad (\text{IV .10})$$

where  $\mu_1$  and  $\mu_2$  are the friction coefficients of two balls in contact.

The jointed cohesive frictional particle model (JCFPM) ([Duriez et al., 2016](#); [Scholtès and Donzé, 2013](#)) is used as the bond model. The JCFPM is an elastic contact law with cohesion joints for fractured rock modelling, which is similar to other contact models for rock ([Potyondy and Cundall, 2004](#); [Wang et al., 2017](#); [Wang and Tonon, 2010](#)). This model is capable of describing not only the macroscopic behaviour of rock, but also the brittle failure of rock. The core of JCFPM is the introduction of an interaction range coefficient  $\gamma_{int}$  to determine the ball interlocking (Fig. IV .8). In fact, the bond can be created between each pair of balls A and B when Eq. (IV .11) is fulfilled

$$D_{AB}^0 \leq \gamma_{int}(R_A + R_B) \quad (\text{IV .11})$$

where  $D_{AB}^0$  is the initial distance between the two centroids of balls A and B,  $R_A$  and  $R_B$  are the radii of two balls, respectively. By using different values of  $\gamma_{int}$ , the interlocking range of bonded balls can be adjusted to simulate various types of rocks ([Scholtès and Donzé, 2013](#)). If  $\gamma_{int} > 1$ , inter-ball bonds can be created between neighbouring particles which are not directly in contact. Even without any introduction of explicit rolling resistance in JCFPM, the increasing of inter-ball locking implicitly induces the increase of the loading moment and internal friction. One must note that  $\gamma_{int}$  will be set to its default value ( $\gamma_{int} = 1$ ) after the first time step when the bonds have been created, and new contacts then occur between strictly contacting balls, which is the classic DEM simulations of granular materials.

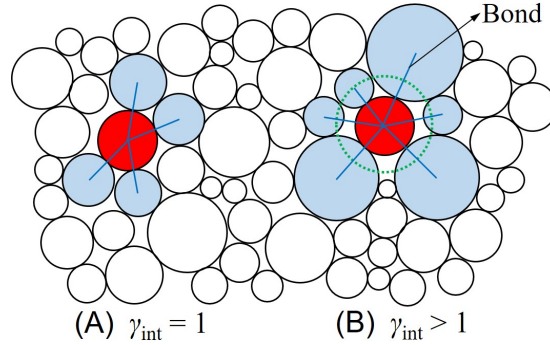


**Figure IV .8:** Interaction range on the contact fabric and grain blocking: (A)  $\gamma_{int} = 1$ ; (B)  $\gamma_{int} > 1$

The normal contact force  $F^n$  in JC-FPM is given by

$$F^n = \begin{cases} k^n u^n, & k^n u^n > F_{max}^n \\ 0, & k^n u^n \leq F_{max}^n \end{cases} \quad (\text{IV .12})$$

where  $F_{max}^n = -tA_{int} < 0$  is the maximum acceptable tensile force, which is calculated from the tensile strength  $t$  (in Pa) and  $A_{int} = \pi(\min(R_A, R_B))^2$ , a surface related to the interacting balls A and B. The normal contact stiffness  $k^n$  can be obtained by using Eq. (IV .9). By using the radii of two contacting balls,  $k^n$  can be written as following

$$k^n = \frac{2ER_A R_B}{R_A + R_B} \quad (\text{IV .13})$$

The tangential contact force  $F^s$  is calculated by a modified Mohr-Coulomb criterion. The maximum admissible shear force  $F_{max}^s$  is a function of the normal force  $F^n$ , the cohesion  $c$ , the local frictional angle  $\varphi_b$  and the local residual frictional angle  $\varphi_c$ . For a bonded interaction, the maximum shear force can be given as

$$F_{max}^s = F^n \tan \varphi_b + cA_{int} \quad (\text{IV .14})$$

When  $F^s \geq F_{max}^s$ , shear rupture occurs. The interaction between initially bonded balls then becomes purely frictional. The maximum shear force  $F_{max}^s$  is defined by the following function

$$F_{max}^s = F^n \tan \varphi_c \quad (\text{IV .15})$$

Similar to the linear contact model in YADE, the parameters of JC-FPM also depend on the ball size (see Eqs. IV .8, IV .9, IV .12-IV .15). This dependence can also ensure that

the model's predictions are independent of its resolution, in which the sample is composed of enough balls to be a REV.

### 3.2 Model calibration: single-particle crushing simulation

In this section, the model parameters are determined to calibrate the force-displacement curve obtained in the single-particle crushing test (section 3 in chapter III). Specimen No.1 in the size class 5 ~ 10 mm is chosen for the numerical simulation. In order to reproduce the experimental condition, the diameter of the agglomerate  $d$  is taken as the diameter of the studied rockfill particle, i.e  $d = 7.50$  mm. The agglomerate is arranged in a hexagonal close packing (HCP) to maximize its density and the average coordination number  $Z_m$ . A representative bonded particle model (BPM) of crushable particle without flaws is then established (Lim, 2004; Wang and Arson, 2016; McDowell and Harireche, 2002). Two loading platens are modelled by disc walls, which are further discretized into 24 triangular facets, respectively. The diameter of the platens are the same as that of the agglomerate. In order to model the platens as rigid bodies, the Young's modulus of the disc walls is ten times higher than that of the elementary balls.

For reasons of simplicity, the gravity force is neglected in the numerical simulations. The simulation is stopped when the vertical strain reaches 3%, implying a loose contact between the platen and the agglomerate as well as the failure of the agglomerate. The breakage strength  $\sigma_f$  is calculated by using the Eq. (IV .4). In order to dissipate the kinetic energy (see Potyondy and Cundall, 2004 for details) in the numerical simulation, a local non-viscous type damping should be used. In the present study, all the numerical simulations are run with a damping coefficient of 0.8.

#### 3.2.1 Preliminary study

In order to get a representative BPM for studied agglomerate and complete the calculation in a reasonable amount of time, a series of parametric study are firstly performed to understand the influence of the loading rate, the elementary ball size and the orientation of hexagonal close packing (HCP). The scheme of the parametric study is given in Table IV .2 while the values of other DEM input parameters are the same (Table IV .3).

**3.2.1.1 Effect of loading rate** In YADE, the loading step increment should be small enough to guarantee the stability of DEM algorithm and a quasi-static loading condition (McDowell and Harireche, 2002; Cho et al., 2007). On the contrary, a high loading rate is

**Table IV .2:** Scheme of parametric study for single-particle crushing test

Influencing factor	Case number	Loading rate (m/s)	Elementary ball size (mm)	HCP orientation(°)
Reference	1	0.020	0.36	0
Loading rate	2 ~ 9	<b>0.001~0.320</b>	0.36	0
Elementary ball size	10 ~ 21	0.020	<b>0.36~1.90</b>	0
HCP orientation	22 ~ 25	0.020	0.36	<b>0, 30, 60, 90</b>

usually adopted to reduce the calculation time. In this section, a series of simulations with eight loading rates (0.001 ~ 0.320 m/s) are conducted to study the influence of loading rate on the macro-behaviour of studied agglomerate as well as on the bond breakage.

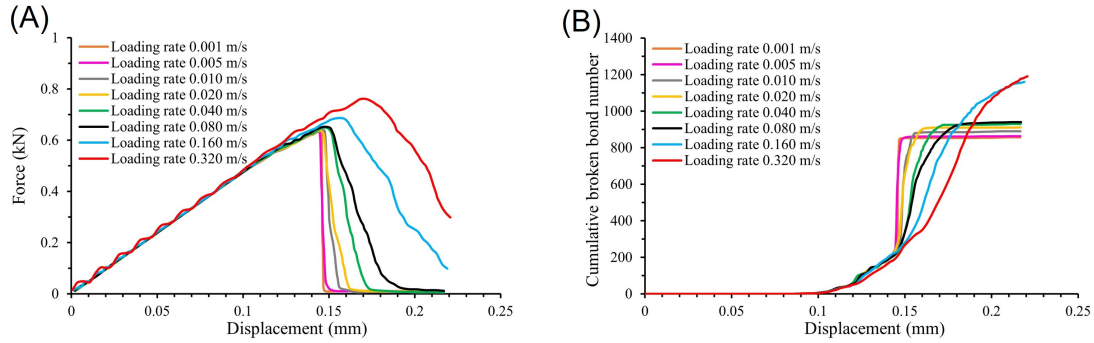


**Figure IV .9:** Influence of loading rate on (A) the force-displacement curves and (B) the evolution of broken bonds

The force-displacement curves of eight cases are given in Fig. V .21A. One observes that both the peak force and the maximum displacement increase with increasing loading rate. When the loading rate is smaller than 0.020 m/s, the curve overlaps more or less with each other. Moreover, the number of broken bonds is also studied (Fig. IV .9B). When the sudden force drop is observed (Fig. IV .9A), a sharp increase of the number of broken bonds is noticed under low loading rate while a gradual increase of broken bonds is gotten under high loading rate (greater than 0.020 m/s). These observations are due to the fact that under high loading rate, the platen still keeps in contact with the agglomerate after failure and the force applied on the platen then cannot drop immediately (Wang et al., 2017). Additionally, a dynamic response is observed in the force-displacement curve when

the loading rate reaches 0.320 m/s. As a result, the loading rate in DEM should be limited in a relatively low range to ensure a quasi-static loading condition. In the present work, the loading rate of 0.020 m/s is adopted in the following simulations.

**3.2.1.2 Effect of elementary ball size** To get a representative description of macro-behaviour of agglomerate, it is important to know how many elementary balls should be used in DEM simulations. With a suitable number of balls, the numerical sample can be considered as a REV of the studied material. In this section, the studied agglomerate with a diameter of 7.50 mm is discretized in numbers of balls (ranging from 24 to 6433), whose diameters vary from 1.90 mm to 0.36 mm.

The obtained breakage strength  $\sigma_f$  and the corresponding number of balls  $N_e$  are given in Fig. IV .10.  $\sigma_f$  augments with the increase of  $d_e$ . For a given studied agglomerate, its volume is fixed: the more balls one uses, the smaller size of elementary balls one obtains. As a result, the number of balls  $N_e$  decreases significantly with the increase of  $d_e$ . The  $N_e$ - $d_e$  relationship can be well fitted by a power function while the  $\sigma_f$ - $d_e$  relationship can be roughly fitted by a quadratic function. One observes that for the BPM adapted in the present study, the agglomerate should contain at least 5000 balls to ensure the algorithm stability. Lim & McDowell (2007) proposed that a minimum of around 500 balls in an agglomerate was necessary to reproduce the particle size effects. This number seems too few for the studied BPM. Three typical agglomerates respectively containing 6433, 120 and 24 balls are also shown in Fig. IV .10. The agglomerate presents a more spherical shape and a more smooth surface with the increase of  $N_e$ . Considering the expensive computational cost, the number of elementary balls is set to 6433 with a diameter of 0.36 mm in the following simulations.

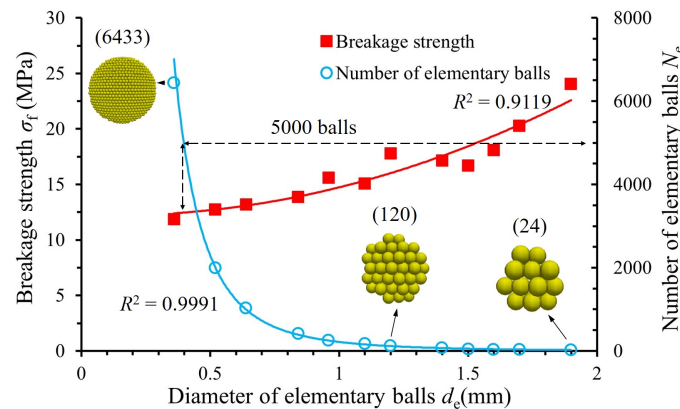


**Figure IV .10:** Evolution of breakage strength in the function of the diameter and the number of elementary balls

**3.2.1.3 Effect of hexagonal close packing orientation** In DEM, the hexagonal close packing (HCP) is always used to generate an agglomerate with maximum packing density (i.e., solid volume fraction of about 74%). In fact, it is the most space-efficient crystal structures (lattices), in which the coordination number of each particle is 12. However, due to the layer structure of HCP, the layer is connected with weak bonds and the obtained BPM then possesses an anisotropic structure. In order to understand the potential anisotropy induced by HCP orientation, the agglomerates with different HCP orientations ( $0^\circ$ ,  $30^\circ$ ,  $60^\circ$  and  $90^\circ$  in reference to the horizontal) are simulated in this section.

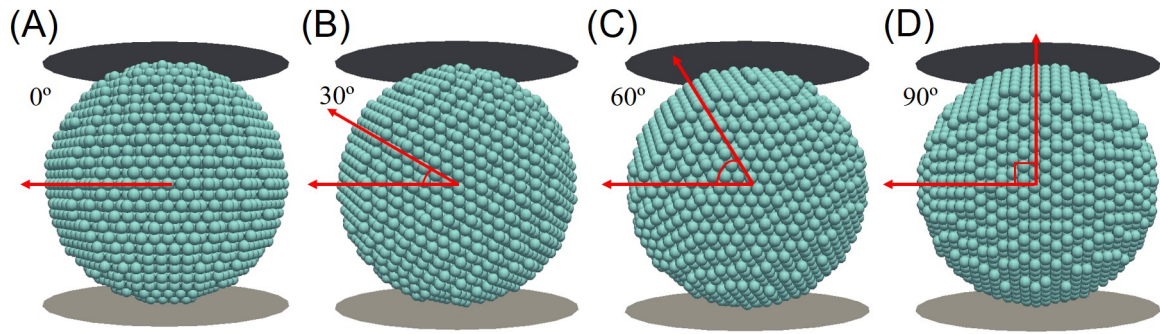


**Figure IV .11:** Agglomerate formed by HCPs with different orientations: (A)  $0^\circ$  ("Horizontal HCP"), (B)  $30^\circ$ , (C)  $60^\circ$ , (D)  $90^\circ$  to the horizontal

The agglomerate structures of HCPs are shown in Fig. IV .11. The obtained force-displacement curves are quite different from each other (Fig. IV .12). The agglomerate with the orientation of  $0^\circ$  (Horizontal HCP) presents the stiffest behaviour and the highest peak force. This observation is related to the lattice structure of HCP agglomerate: for the Horizontal HCP (angle of  $0^\circ$ ), the breakage plane is perpendicular to the layers (see Fig. IV .11a) which are formed by bonded balls. On the other hand, in the other cases (angles of  $30^\circ$ ,  $60^\circ$  and  $90^\circ$ ), the breakage plan may easily appear along one plane between layers. This observation indicates that the anisotropic lattice structure of HCP has a significant effect on the macro-behavior of BPM. Similar results have been found by Wang & Arson (2016). In the present work, the horizontal HCP is adopted in the numerical simulations.



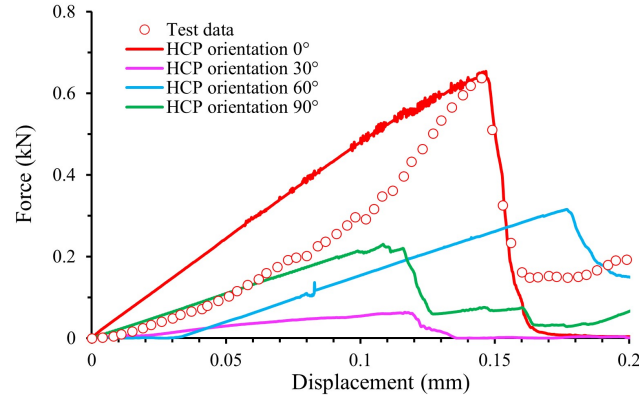


**Figure IV .12:** Force-displacement curves of agglomerates with different HCP orientations

### 3.2.2 Simulation of single-particle crushing test

Based on the preliminary study performed in the section 3.2.1, an agglomerate containing 6433 elementary particles (rigid balls), which allows considering the agglomerate as a REV (Lim and McDowell, 2007), is used in the following simulations. Moreover, the agglomerate is arranged in a hexagonal close packing (HCP) with an angle of  $0^\circ$ . The loading rate of 0.020 m/s is adopted to ensure quasi-static loading conditions.

The model parameters are calibrated by a trial and error process to reproduce the force-displacement curve of the studied sample (Table IV .3).

The force-displacement curve and the evolution of broken bonds are given in Fig. IV .13. Even though the simulated force-displacement curve is almost linear before the sample failure, the peak force and breakage behaviour of studied sample are satisfactorily captured by the numerical simulation. On the other hand, at the beginning of the test, the number of broken bonds increases progressively with the increase of displacement. These broken bonds are related to the induced damage, which can also be called as the development of internal flaws. Consequently, some slight fluctuation is observed in the force-displacement curve. When the applied force approaches the peak, a significant increase of bond breakage is observed in the sample (Fig. IV .13). Therefore, the force-displacement curve drops dramatically and the agglomerate splits into two main pieces (Fig. IV .14A). The observed breakage pattern is similar to that observed in the laboratory test (Fig. IV .14B). The tensile cracks in the agglomerate, represented as deep blue balls (see Fig. IV .14C), confirm the tensile failure of studied sample (Cil and Alshibli, 2012; Cheshomi and Sheshde,



**Table IV .3:** DEM parameters for elementary balls and loading platens

Yade element	Description	Parameter	Value
Elementary balls	Ball diameter (mm)	$d_e$	0.36
	Density (kg/m <sup>3</sup> )	$\rho$	2680
	Number of balls	$N_e$	6433
	Young's modulus (GPa)	$E_{\text{ball}}$	6.0
	Poisson's ratio	$\nu_{\text{ball}}$	0.30
	Friction angle (rad)	$\varphi_{\text{ball}}$	0.5
	Interaction range coefficient	$\gamma_{\text{int}}$	1.0
	Tensile strength (MPa)	$t$	20.6
	Cohesion (MPa)	$c$	206.0
Loading platens	Young's modulus (GPa)	$E_{\text{facet}}$	60.0
	Poisson's ratio	$\nu_{\text{facet}}$	0.45
	Friction angle (rad)	$\varphi_{\text{facet}}$	0.0

2013; McDowell and Bolton, 1998). Based on the obtained numerical results, we can conclude that the BPM is capable of describing the crushing behaviour of the studied rockfill particles.

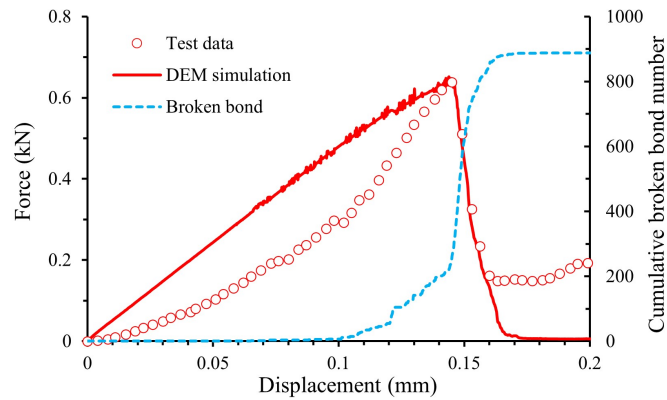


**Figure IV .13:** Force-displacement curve and evolution of broken bonds in single-particle crushing tests. The total number of initial bonds is 15728

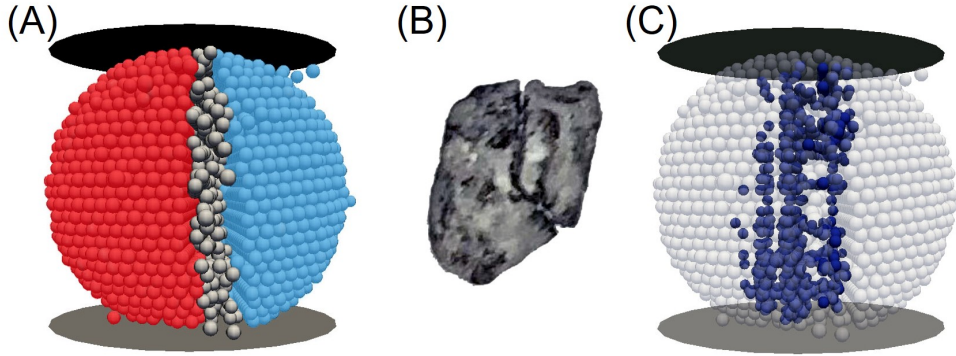


**Figure IV .14:** Comparison of the failure patterns observed in (A) the DEM simulation and (B) the laboratory test; (C) the tensile cracks observed in the broken agglomerate (deep blue balls)

### 3.2.3 Model validation using Buckingham $\pi$ theorem

According to the Buckingham  $\pi$  theorem (Buckingham, 1914), a physically meaningful equation can be expressed in terms of a set of  $p = n - k$  dimensionless parameters  $\pi_1, \pi_2, \dots, \pi_p$ . Here  $n$  and  $k$  are the numbers of physical variables and physical dimensions involved in the equation. This theorem provides a method to describe one variable with a set of dimensionless parameters, even when the form of the equation is still unknown. Based on the Buckingham  $\pi$  theorem, the relationships between micro-scale parameters and macro-scale properties have been investigated in contact bond and parallel bond models (Wang and Arson, 2016; Huang, 1999; Yang et al., 2006). In this section, the relationship between the particle breakage strength and micro-parameters of the jointed cohesive frictional particle model (JCFPM) will be studied via the Buckingham  $\pi$  theorem.

Inspired by the previous work of Huang (1999), the failure of the sample is governed by  $\{k^n R/T^n, T^s/T^n, \mu, k^s/k^n, n, R/L, V/\sqrt{k^n/\rho}\}$ , where  $T^n$  and  $T^s$  are respectively the normal and shear bond strengths,  $R$  is the average ball radius,  $n$  is the porosity,  $L$  is the length of the agglomerate,  $V$  is the loading rate and  $\rho$  is the density of balls. In the present work, the last dimensionless parameter  $V/\sqrt{k^n/\rho}$  can be ignored because the simulation is performed under quasi-static condition. In the JCFPM, as the  $k^n$  and  $k^s$  are expressed as a function of  $E$  and  $\nu$  (see Eq. (IV .9)),  $k^n R/T^n$  and  $k^s/k^n$  can be replaced by  $E/t$  and  $\nu$ . As the tensile and shear strengths are used as  $t$  and  $c$ ,  $T^s/T^n$  is rewritten as  $c/t$ . The porosity  $n$  is deleted from the list because for the BPM with regular HCP in our study, its porosity is constant. Lastly, we add the interaction range coefficient  $\gamma_{int}$  which directly controls the coordination number  $CN$ . Consequently, we propose the following

relationship for the breakage strength  $\sigma_f$

$$\sigma_f = t\Phi\left(\frac{E}{t}, \frac{c}{t}, \mu, \nu, \frac{R}{L}, \gamma_{int}\right) \quad (\text{IV .16})$$

To verify the previous function, a series of simulations with different diameters of agglomerate are conducted while the dimensionless parameters in Eq. (IV .16) are unchanged. The obtained breakage forces are given in Fig. IV .15A. It is observed that the breakage force increases with increasing agglomerate diameter and their relationship can be described by using a strict power law (Fig. IV .15A). On the contrary, the particle breakage strength remains constant (Fig. IV .15B). The obtained results are in consonance with the Buckingham  $\pi$  theorem and confirm the performance of the Eq. (IV .16): the breakage strength of agglomerate should be the same for all agglomerate sizes by using constant DEM dimensionless parameters.

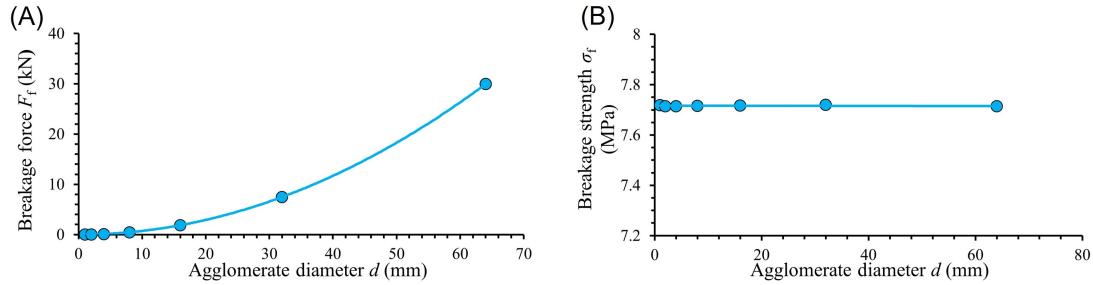


**Figure IV .15:** Evolution of (A) the breakage force and (B) the breakage strength in function of the agglomerate diameter

### 3.3 Numerical modelling of particle size effects

Experiment results exhibit that the breakage strength of small particles is higher than that of large ones. In general, this observation is explained by the fact that large particles possess more and larger flaws than small particles. However, the microscopic issues of the size effects are still not fully understood. In order to get a good understanding of the particle size effects on the breakage strength of studied RFM, some potential causes will be investigated via a series of parametric study, including the agglomerate size as well as the flaw sizes, the flaw numbers and the flaw volume ratios of studied agglomerate. The agglomerates are packed in a HCP with an angle of  $0^\circ$  and the loading rate is set to 0.020 m/s. The other DEM input parameters can be found in Table IV .3.

### 3.3.1 Effects of agglomerate size and internal flaws

The influence of agglomerate size on the breakage strength of the studied RFM and the role of internal flaws in the particle size effects are studied in this section. In view of this, 36 agglomerates with different diameters are prepared and divided into two categories: without and with internal flaws. In order to mimic the flaws, 10% balls of the agglomerate without flaws are randomly deleted to get one with internal flaws. In other words, an agglomerate without flaws possesses a flaw volume ratio of 0% while the flaw volume ratio of an agglomerate with flaws is equal to 10%.

The influence of agglomerate size on the breakage strength of studied RFM is firstly analysed. As the same sized elementary balls are used in the BPM, the diameter of agglomerate  $d$  increases with increasing the number of elementary balls  $N_e$  (Fig. IV .16). The  $N_e$ - $d$  relationship can be well fitted by a power function. When the agglomerate contains more than 5000 balls, a constant  $\sigma_f$  is obtained even though the diameter of agglomerate continues to increase. This observation indicates that the particle size is not the origin of particle size effects. Moreover, it confirms again that at least 5000 balls are necessary for the BPM to be a REV, which are previously proposed in section 3.2.1.

The relationship between the breakage strength  $\sigma_f$  and the agglomerate diameter  $d$  is also shown in Fig. IV .16. The  $\sigma_f$ - $d$  relationship can be roughly fitted by a power function. Similar tendencies can be found in the two types of agglomerates: the breakage strength  $\sigma_f$  tends to be a constant value with increasing the agglomerate diameter. When the agglomerate diameter  $d$  is less than 5 mm, a significant variation of breakage strength is observed in the agglomerates without flaw. These differences are due to the fact that the agglomerate with flaws possesses 10% balls less than the agglomerate without flaw. As numerous balls are removed, the average contact per particle, namely average coordination number, decreases and more stress concentrations are created in the agglomerate. Conversely, when  $d$  is greater than 5 mm, the same breakage strength is obtained for the agglomerates with different sizes. Therefore, the breakage strength of agglomerates does not depend on the particle size when the ratio of ball size to agglomerate size is smaller than 0.0514 (i.e., for the agglomerates formulated with at least 5000 balls). This observation is coincident with the fact that some particles with uniform structure have no size effects (Zhou et al., 2016; Yoshimoto et al., 2012). By comparing two curves obtained with two types of agglomerates, lower breakage strength is obtained in the samples with flaws (Huang et al., 2020). For instance, a breakage strength of 2.63 MPa is finally observed in the agglomerate without flaws while  $\sigma_f$  is equal to 1.87 MPa in the agglomerate with flaws (10%).

Consequently, we can conclude that the internal flaws is a key issue of particle size effects. In practice, as the RFM particle is a porous media, the flaws include the internal defects (such as micro cracks, confined air bubbles and impurities etc...) in the present work. In the following, the influence of flaw sizes, flaw numbers and flaw volume ratios will be analysed. As the random deletion of balls induces the fluctuation of numerical results, the same agglomerate with flaws will be simulated six times and the mean values are used for the numerical analysis.

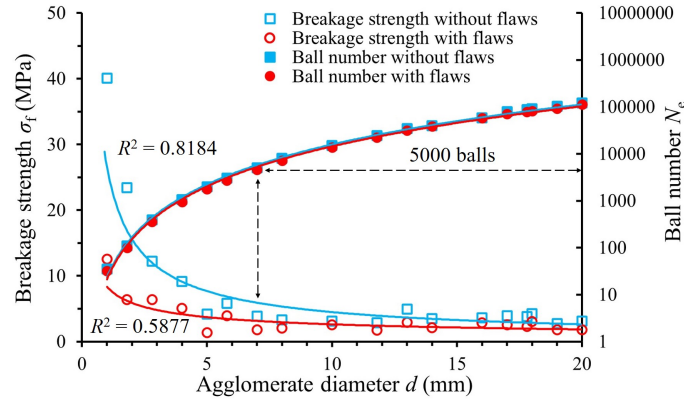


**Figure IV .16:** Relationship between the agglomerate diameter and breakage strength or ball number for the agglomerates without and with flaws

### 3.3.2 Effect of flaw size

In this section, the influence of flaw size on the breakage strength of agglomerate is studied. A series of numerical simulations are performed by using four flaw numbers (129, 257, 515 and 772 flaws) and three flaw sizes. Different flaw sizes are realized by deleting one ball solely, two balls in contact and three balls in contact. The flaw sizes of two/three balls are realized in two steps. Firstly, a random distribution of flaw centroids is generated. Then the flaws are created by deleting one/two balls in contact with each centroid ball.

For each given flaw number, the relationships between the particle breakage strength  $\sigma_f$  and the flaw size are given in Fig. IV .17, in which the error bars indicate the standard deviation. In general, the breakage strength  $\sigma_f$  decreases as the flaw size increases. By comparing the results obtained with different flaw numbers, the most important decrease of breakage strength is obtained in the case with the largest flaw number (i.e., 772 flaws). Additionally, for the sample with 772 flaws with the size of 3 balls,  $\sigma_f$  is almost equal to zero (0.70 MPa). This observation indicates that when 36% balls are deleted, the corresponding agglomerate almost loses its bearing capacity even though some balls are still bonded. Therefore, in the numerical simulation, great care should be taken in the

choice of the percentage of deleted balls. The obtained results are partially coherent with the Griffith theory: in the samples with the same number of flaws, the strength of the crushable particles depends on the size of the largest flaw.

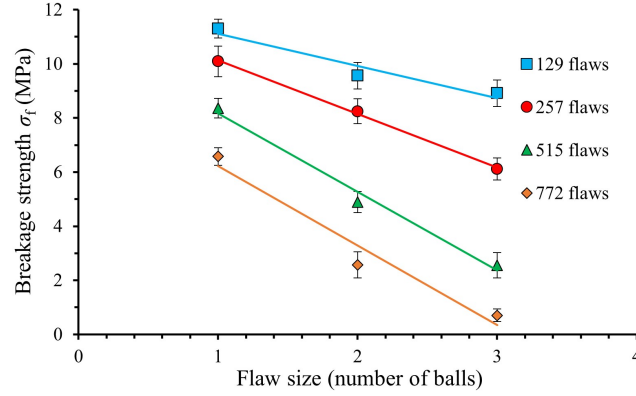


**Figure IV .17:** Relationship between the breakage strength and flaw size of the agglomerates with different flaw numbers

### 3.3.3 Effect of flaw number

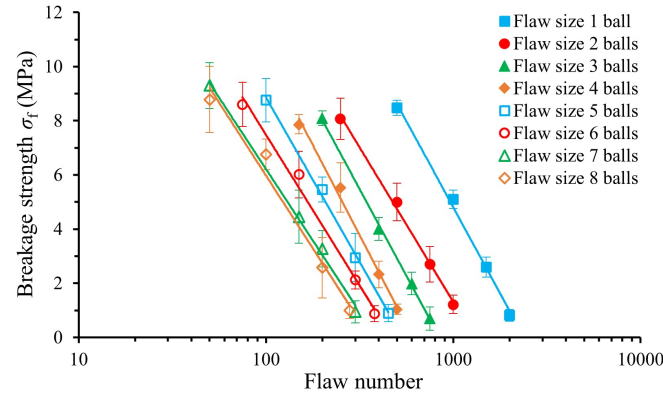


**Figure IV .18:** Relationship between the breakage strength and flaw number for agglomerates with different flaw sizes

In this section, the effect of flaw number on the particle breakage strength  $\sigma_f$  is studied. Eight series of samples are prepared by using different flaw sizes. Flaw sizes are classed by the number of balls deleted, from  $n = 1$  to  $n = 8$ . Firstly, a random distribution of flaw centroids is generated. Then the flaws are created by deleting  $(n - 1)$  balls in contact with each centroid ball. The particle breakage strength  $\sigma_f$  against flaw number is plotted in a semi-logarithmic plane (Fig. IV .18). For each flaw size, the particle breakage strength  $\sigma_f$  linearly decreases with the increase of flaw number. The comparison of eight cases shows

that the obtained slopes are very close to each other. By comparing the results obtained in this section and in section 3.3.2, it can be concluded that the flaw number has more pronounced effects on the particle breakage strength  $\sigma_f$  of RFM than the flaw size.

### 3.3.4 Effect of flaw volume ratio

The influence of flaw volume size is studied in this section. The "flaw volume ratio" is considered as the percentage of deleted balls in this work. Some samples are created with the same flaw volume ratio but different flaw sizes.

The breakage strengths  $\sigma_f$  of samples with different flaw sizes are given in Fig. IV .19. The breakage strength of agglomerate decreases with its flaw volume ratio. The results for the samples with the same flaw volume ratio but different flaw sizes are almost the same, indicating the relatively weak effects of flaw size on  $\sigma_f$  with respected to the flaw volume ratio. The obtained values can be fitted by a quadratic function, which is similar to the DEM results for sand particles by Wang & Arson (2016). Furthermore, Guida et al. (2018) recently confirmed that the particles with high internal porosity had a propensity to break in the 1-D compression in-situ X-ray test. In view of this, we can conclude that the size effects of particle strength is related to its "flaw volume ratio". The DEM simulations verify the previous assumption that "large particles have many flaws" in a microscopic view. However, the assumption "large particles have big flaws" still can not be validated by DEM in the present work.

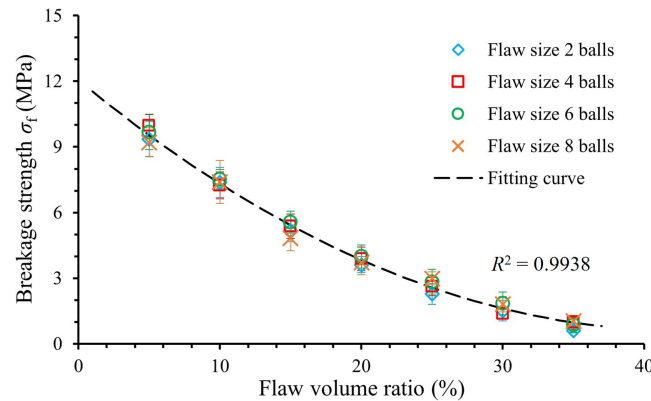


**Figure IV .19:** Relationship between the breakage strength and flaw volume ratio for the agglomerates with different fixed flaw sizes

## 4 Conclusions

A series of laboratory tests, theoretic analysis and numerical simulations of single-particle crushing tests are conducted to investigate the particle size effects on breakage characteristics of rockfill particles. The main conclusions can be summarized as follows:

(1) The relationship between the breakage strength of studied rockfill particles and their survival probability is obtained via a series of single-particle crushing tests. The breakage strength follows the Weibull distribution, with the Weibull modulus  $m$  of 3.29. The Weibull modulus  $m$  is independent of the particle size and can be considered as a material parameter.

(2) By comparing the values of characteristic strength obtained with different particle sizes, it is found that the characteristic strength decreases with increasing particle size, which can be described by the size effect parameter  $b$ . With respected to the absolute value of  $b$ , the particle size effects of different rock can be roughly divided into three types: weak size effect ( $|b| < 0.4$ ), medium size effect ( $0.4 < |b| < 0.7$ ) and strong size effect ( $|b| > 0.7$ ). The rockfill particles studied in the present work belong to the weak size effect type with  $|b| = 0.22$ . For rock particles, the size effect parameter  $b$  is recommended to be measured directly from laboratory tests. Otherwise, with respected to  $-3/m$ ,  $-2/m$  is more advisable for the estimation of  $b$ .

(3) In YADE, the crushable rockfill particle is simulated as a quasi-spherical agglomerate of bonded and packed balls. A bonded particle model (BPM) is then used to simulate the single-particle crushing tests. The model parameters are calibrated by using the force-displacement curve obtained in the laboratory test. The comparison of test data and numerical simulations exhibits that the adopted DEM model is capable of describing the breakage strength and failure pattern of studied rockfill particles. The BPM in our study needs at least 5000 balls to be a representative elementary volume (REV).

(4) The calibrated BPM is also used to study the particle size effects on breakage strength. By comparing the crushing processes of agglomerates with and without internal flaws, it is observed that for a given flaw volume ratio, the breakage strength of rockfill particles does not depend on the particle size when the ratio of ball size to agglomerate size is smaller than 0.0514 (i.e., for the agglomerates formulated with at least 5000 balls). On the other hand, for a given flaw size, the breakage strength of agglomerate decreases when the number of flaws increases. By considering that the internal flaws include all the internal defects of studied RFM, for the agglomerate with a flaw volume ratio smaller than 36%, particle breakage strength only depends on the flaw volume ratio, but not the flaw size.



As the rockfill particle is simulated as a spheric agglomerate, which is loaded at extreme points, the numerical simulation is only capable of reproducing one breakage type. In the near future, the numerical methods presented in this paper will be improved to model the failure patterns of rockfill particles considering their real geometry.

## Chapter V

# Influence of particle size on the mechanical behavior of studied rockfill materials in oedometer tests

### 1 Introduction

Rockfill materials are widely used in the construction of dams and embankments due to their numerous advantages, such as inherent flexibility, local availability, and good ability to absorb seismic energy, etc...([Alonso et al., 2012](#); [Lade et al., 1996](#); [Xiao et al., 2020](#)). As rockfill is generally obtained from rock quarry or riverbed, it usually covers a wide range of particle sizes. In the rockfill structures, large particles usually have a high coordination number since they are surrounded by a lot of small particles. Thus, the small particles are always in a more inhomogeneous internal stress state, making them more easily to break. On the other hand, it is generally accepted that the strength of rockfill particles decreases with increasing particle size due to the fact that small particles contain fewer internal defects. Hence, the intrinsic strength and extrinsic coordination number largely determine the crushing of particles. Under the high stress field of rockfill dams, the occurrence of grain crushing induces the settlement and then alters the mechanical behaviors and transport properties of rockfill materials ([Coop et al., 2004](#); [Kh et al., 2011](#); [Lade et al., 1996](#); [Luzzani and MR, 2002](#); [McDowell and Bolton, 1998](#); [Tarantino and Hyde, 2005](#); [Varadarajan et al., 2003](#)). As the force transmission in a pack of particles

depends on the number of contacts between the particles ([Ben-Nun and Einav, 2008](#); [Lobo-Guerrero and Vallejo, 2005a](#); [Lobo-Guerrero et al., 2006](#)), the packing of rockfill assembly has an important impact on the breakage mechanics of rockfill materials. In view of this, the durability of rockfill dams requires a good understanding of the crushing of rockfill materials with the consideration of the influence of coordination number.

The discrete element method (DEM) provides one of the most effective way to investigate grain crushing and mechanical behavior of granular materials. In DEM, two alternative approaches can be used to simulate particle breakage: bonded particle approach ([Cil and Alshibli, 2014b](#); [Lim and McDowell, 2007](#); [Potyondy and Cundall, 2004](#); [Tapias et al., 2015](#); [Wang and Yan, 2013](#)) and population balance approach ([Aström and Herrmann, 1998](#); [Ben-Nun and Einav, 2008, 2010](#); [Ciantia et al., 2015, 2014](#); [Couroyer et al., 2000](#); [Elghezal et al., 2013](#); [Esnault and Roux, 2013](#); [Hanley et al., 2015](#); [Lobo-Guerrero and Vallejo, 2005a](#); [Lobo-Guerrero et al., 2006](#); [Marketos and Bolton, 2009](#); [McDowell and de Bono, 2013](#); [Tapias et al., 2015](#); [Tsoungui et al., 1999](#); [Zhou et al., 2020, 2016](#)). In the bonded particle approach, the crushable particle is usually represented by an agglomerate, which is composed of a group of bonded balls. The particle breakage is modelled by the bond breakage within the agglomerate. On the other hand, in the population balance approach (also called the replacement method), the particle breakage is verified by a breakage criterion and embodied by replacing the broken particle with several small fragments. Therefore, with respect to the population balance approach, the bonded particle approach is more straightforward as no breakage criterion is needed to describe the particle breakage. However, the bonded particle approach demands a very high computational effort ([Lim and McDowell, 2007](#)) and cannot quantitatively capture the evolution of void ratio and particle size distribution. Therefore, the population balance approach has been widely used to simulate the crushing of granular materials because of its computational economy ([Weerasekara et al., 2013](#)) and the relatively realistic reproduction of particle size distribution and fractal dimension ([de Bono and McDowell, 2016b](#)).

The most important modelling choices in the population balance approach are a particle breakage criterion and a particle spawning criterion ([Ciantia et al., 2015](#); [de Bono and McDowell, 2016a](#); [Zheng and Tannant, 2018](#)). The particle breakage criterion is used to decide whether a particle is crushed while the relationship between the disappeared broken particle and the newly generated smaller particles is established by the particle spawning criterion. One important issue in the particle spawning processes is mass conservation of generations. According to commonly used breakage criteria in population balance approach, they can be divided into two groups: maximum contact force criteria ([Aström and](#)

Herrmann, 1998; Ciantia et al., 2015; Couroyer et al., 2000; Elghezal et al., 2013; Hanley et al., 2015; Lobo-Guerrero and Vallejo, 2005a; Lobo-Guerrero et al., 2006; Marketos and Bolton, 2009) and stress tensor criteria (Ben-Nun and Einav, 2010; Esnault and Roux, 2013; McDowell and de Bono, 2013; Tsoungui et al., 1999; Zhou et al., 2020, 2016). In the maximum contact force criteria, the particle crushing is deemed to be caused by one single contact force, for instance, the stress induced by the maximum normal contact force  $\sigma_{Fm}$ . Aström & Herrmann (1998) used  $\sigma_{Fm}$  to study the particle crushing. A stable breakage process was observed with the development of small fragments surrounding large particles. The survival of large particles is relative to the distribution of contact forces due to their high coordination numbers. The  $\sigma_{Fm}$  criterion was later used in 3D case by Couroyer, et al (2000). However, the broken particles were not replaced by any fragments, meaning that the mass conservation was not obeyed. Recently, Ciantia et al. (2015; 2014) have used a modified  $\sigma_{Fm}$  criterion in the 3D oedometer test simulations, in which the contact area  $A_F$  was considered as a function of the contact solid angle  $\theta_0$  and the particle diameter  $d$ . Hanley et al. (2015) adopted  $\sigma_{Fm}$  to simulate the triaxial compression tests performed on the samples with a poor gradation. The broken particles were replaced by small particles while the mass balance was realized by adding fine particles in the void space. The obtained normal compression and critical state lines were coincident with the experimental observation. However, the maximum contact force criterion emphasizes the effect of stress concentration on particle failure but neglects the global stress state of particles. The introduction of explicit correction factors are necessary to take into account the influence of coordination number.

On the other hand, the stress tensor criteria are developed by using the average particle stress tensor, for instance: mean stress  $p$ , octahedral shear stress  $q_{oct}$  and von Mises stress  $\sigma_{vm}$ , etc... Aström & Herrmann (1998) used a mean stress criterion in 2D case. However, unstable particle breakage was observed. By analyzing the particle stress distribution under biaxial compression conditions, Tsoungui et al. (1999) have proposed a 2D Drucker-Prager criterion, in which the grain fragmentation was controlled by the deviatoric stress  $q$ . The important contribution of their work is to exhibit an important restraining effects of hydrostatic stress on the particle breakage. Esnault & Roux (2013) adopted the von Mises  $\sigma_{vm}$  criterion in their 3D oedometer test simulations. However, the volume loss of 52% was noticed during fragmentation and only one allowable generation of fragments underestimated the mechanical role of small particles. With the assumption of no particle breakage induced by hydrostatic stress, McDowell & de Bono (2013) used the octahedral shear stress  $q_{oct}$  as the breakage index. The mass conservation was kept by an excessive

overlap of fragments inside the parent particle, and a fractal number of 2.5 was observed in the particle size distribution. Therefore, the stress tensor criterion is capable of taking into account the stress state of particle. In practice, the increasing coordination number or hydrostatic stress prevents the particle crushing (Salami et al., 2019; Todisco et al., 2015). However, due to the complex stress state applied on the particle, the consideration of the influence of coordination number in the breakage criterion is very limited in the literature.

Although numerous DEM studies have been performed to study the crushing of particles under compression, most of these works focus on the understanding of microscopic responses and the influence of micro-parameters on the macroscopic behaviour of granular materials. To the best of authors' knowledge, the calibration of a DEM study of particle crushing with the realistic experimental data has rarely been realized in the literature. The originality of the present study is to propose a new breakage criterion for the crushing of rockfill particles, in which the effects of coordination number on the crushing of rockfill particles are taken into account. The breakage criterion for the particle crushing will be calibrated by using a series of laboratory tests. The proposed criterion is firstly validated by simulating one oedometer test. Afterwards, the influence of particle size on the crushing processes and mechanical behaviour of rockfill materials is studied via the simulation of oedometer tests with different sizes of particles. In order to illustrate the advantage of proposed criterion in the consideration of the effects of coordination number, the proposed criterion is compared with different criteria of particle crushing.

## **2 Numerical analysis of the effect of coordination number on the crushing of rockfill particles**

As aforementioned, numerous studies (Ben-Nun and Einav, 2008; McDowell and de Bono, 2013; Salami et al., 2019; Todisco et al., 2015; Tsoungui et al., 1999) have shown that the coordination number  $CN$  plays an important role in the particle breakage. In order to get a better understanding of the  $CN$  effect on the failure pattern and strength of rockfill particles from a micro-scale view, an oedometer test (referred to as multi-particle crushing test) is studied in this section. The tested sample is simulated as a particle pack, composed of 75 particles. A single randomly selected particle is replaced with an agglomerate of 487 smaller bonded balls (red) while all other particles are simulated as unbreakable ones (grey) (Fig. V.1). As the emphasize of the present study focuses on the influence of coordination number on the particle breakage, for reason of simplicity, both the rigid

particles and the single agglomerate are simulated as balls.

To build the tested sample, 75 rigid particles are generated above a cylindrical container of  $40 \times 80$  mm (diameter  $\times$  high) and then drop into it under gravity. In order to get a dense packing, the friction angle is set to 0 during the deposition process. The friction angle is then reset to its original value before compression. One of the rigid particles is randomly chosen and replaced by an agglomerate. The sample is compressed by the upper wall with a constant velocity of 0.1 m/s.

The simulations are performed with YADE, an open source framework based on the discrete element method (Kozicki and Donze, 2008, 2009). In YADE, rigid "balls" are allowed to overlap with a contact area which is negligible with respect to the ball size. The linear contact model is applied on unbreakable balls (grey ones) while the jointed cohesive frictional particle model (JCFPM) (Duriez et al., 2016; Scholtès and Donzé, 2013) is adopted for the small bonded balls (red ones) in the agglomerate. Similar to the parallel bond in PFC (Potyondy and Cundall, 2004), the JCFPM bond in YADE is capable of transmitting contact force and moment between two contacting balls. Four contact parameters are used to define a bond in JCFPM: interaction range coefficient, bond radius, bond tensile strength and bond cohesion. The interaction range coefficient is used to adjust ball interlocking. The bond radius is equal to the minimum radii of two bonded balls. The forces applying on the two bonded balls create tensile and shear stresses in the bond. When the maximum stress is greater than the bond strength, the bond is removed and the crushing of the agglomerate occurs (Fig. V .1).

When the sample is compressed, the bond failure modes (tensile and shear) inside the agglomerate (red) are tracked. Cil & Alshibli (2014b) considered that the agglomerate was fractured when the cumulative number of broken bonds was equal or greater than 5% of the initial total bonds. In the present study, the 5% limit is adopted as the judgement of the failure of agglomerate. This process is accompanied by a sudden drop in contact forces acting on the single agglomerate and typically visible particle fragmentation. The contact forces acting on the agglomerate from adjacent particles are recorded when it is fractured. In order to study the influence of coordination number on the crushing of particles, the previous steps are repeated on a different randomly selected single particle inside the particle pack. In total, 314 agglomerates under different contact configurations are studied. The influence of coordination number on the failure pattern and strength of rockfill particles will be analysed.

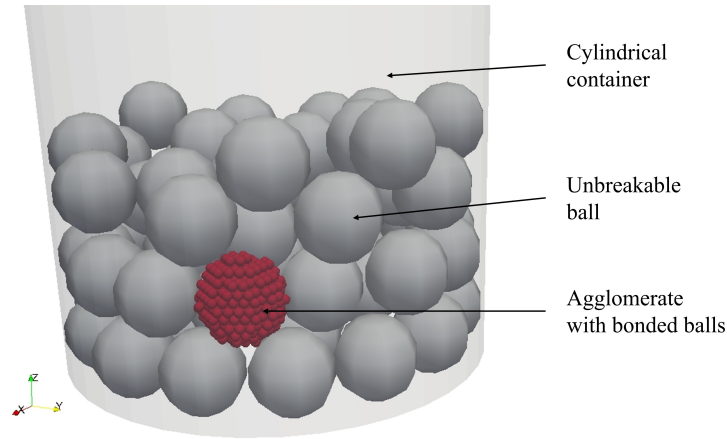


**Figure V .1:** Schematic of the multi-particle crushing test

**Table V .1:** Summary of DEM parameters in the multi-particle crushing test

Parameter	Value
Ball density ( $\text{kg/m}^3$ )	2680
Wall/unbonded ball Young's modulus (GPa)	0.06
Wall/unbonded ball Poisson's ratio	0.45
Wall/unbonded ball friction angle (rad)	0.52
Unbonded ball diameter (mm)	7.76
Bonded ball Young's modulus (GPa)	6.00
Bonded ball Poisson's ratio	0.30
Bonded ball friction angle (rad)	0.52
Bonded ball interaction range coefficient, $\gamma_{int}$	1.0
Bonded ball tensile strength, $t$ (MPa)	4.6
Bonded ball cohesion, $c$ (MPa)	46
Bonded ball diameter (mm)	0.80
Damping coefficient	0.3

## 2.1 Influence of coordination number on the crushing pattern of crushable agglomerate

Typical contact force chains (blue) and tensile breakage patterns (red) in the crushable agglomerate are given in Fig. V.2. It is observed that the agglomerate is usually broken in a tensile mode (Irwin, 1957). This observation confirms the fact that the tensile strength governs the breakage of particles under compression (Altuhafi and Coop, 2011; McDowell and Bolton, 1998). Moreover, the failure pattern is significantly affected by the coordination number  $CN$ . When  $CN \leq 4$ , large force chains are developed at contact points and the agglomerate is usually split into 2 or 3 main pieces (Fig. V.2 a,b,c). When  $CN > 4$ , the contact force chains are homogeneously distributed throughout the agglomerate, which is split into several smaller portions (Fig. V.2 d,e,f). In general, the distribution of bond breakage is coincident with that of force chains. When  $CN \leq 4$ , almost all the bond breakage occurs within the strong force chains while the distribution of bond breakage becomes homogeneous when  $CN > 4$ . This observation is coherent with the previous DEM simulation results (Cil and Alshibli, 2014b; Zheng and Tannant, 2018).

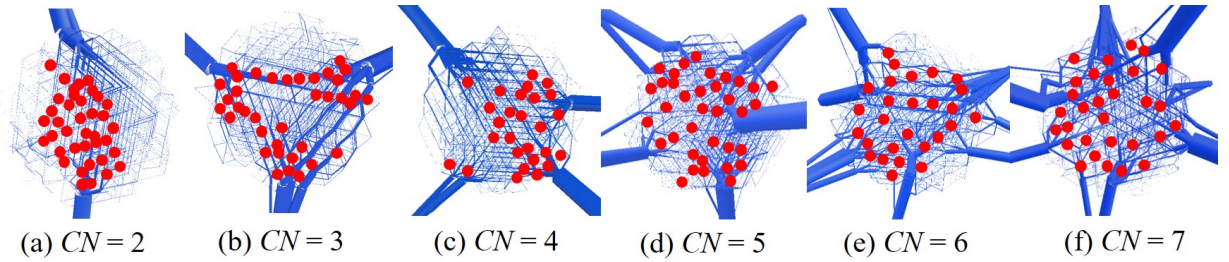


**Figure V.2:** Typical force chain network (blue lines) and tensile bond breakage patterns (red points) for the broken agglomerates with different coordination number  $CN = 2 \sim 7$

In Figs. V.2, all the contact points participate in the strong force chain network, which are the common cases in the simulation. However, some weak force chains are also observed in Figs. V.3, indicating that not all the contact points participate in the strong force chains. Here, the number of contact points participating in the strong force chains is noted by  $NSF$ , which is equal or less than  $CN$ . As shown in Fig. V.3a, the coordination number  $CN$  is 5, and only two contact points form the strong force chain ( $NSF = 2$ ). Moreover, the force chain network in Fig. V.3a with  $CN = 5$  is similar to that in the Fig. V.2a with  $CN = 2$ . In view of this, it is not reasonable to directly consider the coordination number in the estimation of particle strength, like the work of Ben-Nun & Einav (2008). This observation also exhibits the complexity effects of coordination number



on the failure pattern of rockfill particles.

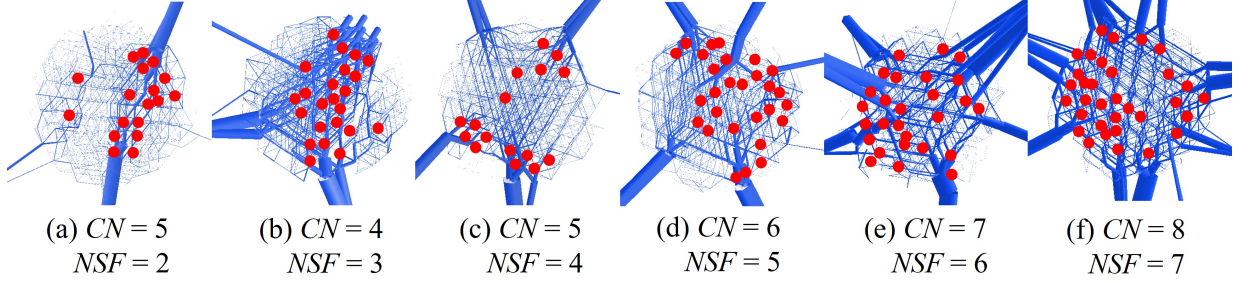


**Figure V .3:** Typical force chain network (blue lines) and tensile bond breakage patterns (red points) for the broken agglomerates with different values of coordination number  $CN = 5 \sim 8$  and different values of contact points participating in the strong force chains  $NSF = 2 \sim 7$

## 2.2 Influence of coordination number on the crushing strength of crushable agglomerate

In order to investigate the effect of coordination number on the breakage index, the the "maximum contact force" type stress, i.e., the stress induced by the maximum normal contact force  $\sigma_{Fm}$  (Eq. V .2) and four most widely used "stress tensor" type stress indexes: mean stress  $p$  (Eq. V .3), deviatoric stress  $q$  (Eq. V .4), octahedral shear stress  $q_{oct}$  (Eq. V .5) and major principal stress  $\sigma_1$  are calculated for 314 agglomerates under different contact configurations. The stress tensor type indexes can be estimated by using the average stress tensor  $\sigma_{ij}$ , which can be obtained by:

$$\sigma_{ij} = \frac{1}{V} \sum_{N_c} (x_i^{(c)} - x_i^{(p)}) F_j^{(c,p)} \quad (V .1)$$

where  $V$  is the particle volume,  $N_c$  is the total number of contacts on the particle,  $x^{(c)}$  and  $x^{(p)}$  are the locations of the contact and particle, respectively, and  $F_j^{(c,p)}$  is the force acting on the particle at contact (c).

Following the previous works (de Bono and McDowell, 2016a; Esnault and Roux, 2013; Hanley et al., 2015; Marketos and Bolton, 2009), the stress induced by the maximum normal contact force  $\sigma_{Fm}$ , can be written as:

$$\sigma_{Fm} = F_{max}/d^2 \quad (V .2)$$

where  $d$  is the particle diameter and  $F_{max}$  is the maximum normal contact force.

The stress tensor index 1 is based on the mean particle stress  $p$ , which has been used by Aström & Herrmann (1998):

$$p = \frac{1}{3}(\sigma_1 + \sigma_2 + \sigma_3) \quad (\text{V .3})$$

where  $\sigma_1$ ,  $\sigma_2$  and  $\sigma_3$  are three principal stresses.

The stress tensor index 2 is as the von Mises stress  $\sigma_{vm}$  or the deviatoric stress  $q$ , used by Esnault & Roux (2013):

$$\sigma_{vm} = q = \sqrt{\frac{1}{2}[(\sigma_1 - \sigma_2)^2 + (\sigma_2 - \sigma_3)^2 + (\sigma_1 - \sigma_3)^2]} \quad (\text{V .4})$$

The octahedral shear stress  $q_{oct}$  adopted by McDowell & de Bono (2013) is used as the third stress tensor index:

$$q_{oct} = \frac{1}{3}\sqrt{[(\sigma_1 - \sigma_2)^2 + (\sigma_2 - \sigma_3)^2 + (\sigma_1 - \sigma_3)^2]} \quad (\text{V .5})$$

Besides, the major principal stress adopted by McDowell & de Bono (2016a) is also used as the fourth stress tensor index.

For different samples, the frequency distribution of coordination number of the single agglomerate is shown in Fig. V .4a. It can be seen that the coordination number  $CN$  varies from 2 to 9 and is mostly located between 4 and 7 in the particle assembly. Similar results have been obtained by de Bono & McDowell (2015) in a particle packing with irregular particle shapes. For a given coordination number, the mean values of five stress indexes ( $\sigma_{Fm}$ ,  $\sigma_1$ ,  $q_{oct}$ ,  $p$ , and  $q$ ) are given in Fig. V .4b. One observes that except the data points with  $CN = 2$ , a clear increase of particle strength with increasing  $CN$ . This dependence of particle strength on the coordination number is coherent with the experimental studies (Salami et al., 2019; Todisco et al., 2015). By comparing the mean values of different stress index, one can observe that the octahedral shear stress  $q_{oct}$  increase very slightly with the increase of coordinate number. Conversely, the deviatoric stress  $q$  increases more obviously with the coordinate number. According to the Eqs. V .4 and V .5, the values of  $q_{oct}$  and  $q$  are proportional:  $q_{oct} = \frac{\sqrt{2}}{3}q \approx 0.236q$ . Therefore,  $q_{oct}$  exhibits a small dependence on the coordination number with respect to  $q$ . On the other hand, the slight increase of stress indexes with  $CN$  could be attributed to the narrow range of  $CN$  in the present study. This is due to the use of particle packing with uniform sizes. Furthermore, according to the work of Wang & Arson (2016), the particle strength will be improved a lot with the

increase of  $CN$  when the  $CN$  is in the range of  $10 \sim 120$ .

According to the high value of stress obtained with  $CN = 2$ , this observation may be related to the numerical inaccuracy due to the low frequency of  $CN = 2$  (Fig. V.4a), the artificial choice of 5% cumulative broken bonds for the judgement of particle failure, and the anisotropic structure of the agglomerate due to the hexagonal close packing.

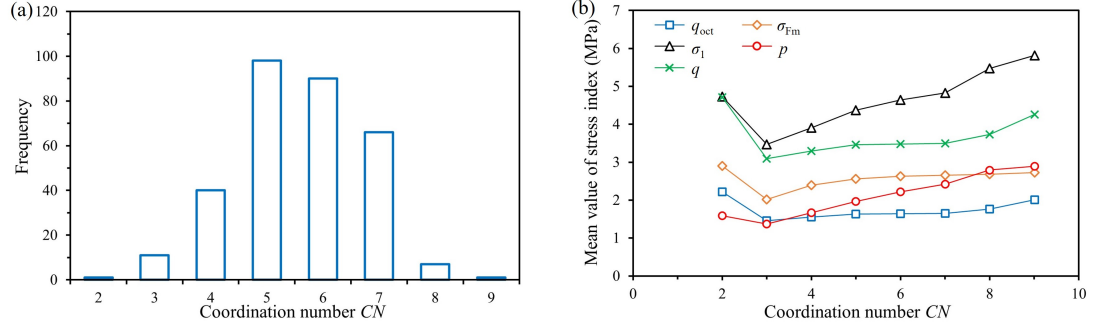


**Figure V.4:** Simulation results of multi-particle crushing tests: (a) frequency distribution of coordination number and (b) evolution of the mean value of five stress indexes in function of coordination number

### 2.3 Partial conclusion

As discussed above, the coordination number have an important impact on the breakage pattern and failure strength of rockfill particles. Therefore, it is reasonable to consider the influence of coordination number  $CN$  in the breakage criterion. Additionally, due to the existence of strong and weak force chains (Fig. V.3), it's unreasonable to directly introduce  $CN$  in the breakage criterion. In order to properly take into account the effect of  $CN$  on the crushing behaviour of rockfill particles, a breakage criterion will be proposed in the next section.

## 3 Proposition of a new breakage criterion for rockfill particles considering the effect of coordination number

In practice, large particles generally have a high coordination number, which creates a hydrostatic stress effect around them. Moreover, McDowell & de Bono (2013) have shown that in the multi-grain structures, the particle failure is generally induced by a "shear" type stress, e.g., deviatoric stress  $q$ . In view of these observations, the values of mean stress  $p$  and deviatoric stress  $q$  acting on 314 agglomerates at the breakage moment are drawn in Fig. V.5. For a given coordination number, one observes that the deviatoric

stress  $q$  increases with increasing mean stress  $p$ : at a high level of mean stress  $p$ , a high value of  $q$  is needed for particle breakage. In general, the relationship between  $p$  and  $q$  at the failure moment can be fitted by a regression line (black dashed line in Fig. V.5).

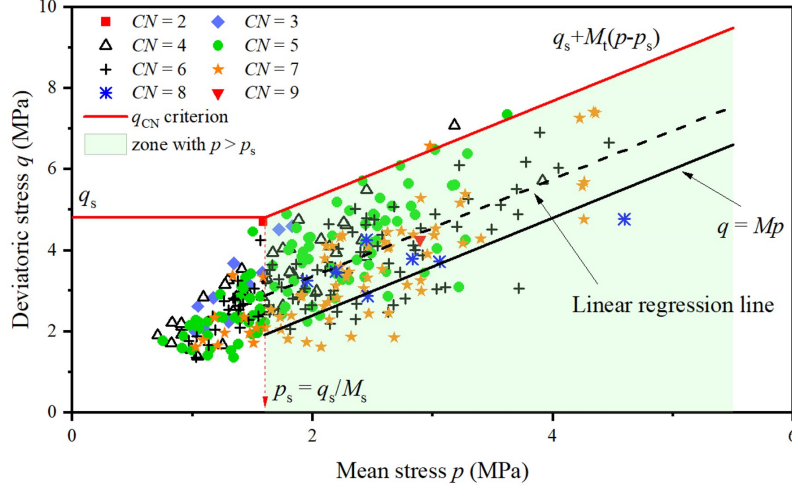


**Figure V.5:** Stress state of agglomerates at failure in  $p - q$  plane

Based on these observations, a new breakage criterion is proposed for the crushing of rockfill particles, considering the effect of coordination number.

### 3.1 Proposition of a breakage criterion

Inspired by the research works of McDowell & de Bono (2016a; 2015; 2013), it is observed that gain crushing is induced by the deviatoric stress. A particle breakage criterion (referred to as  $q_{CN}$  criterion), based on the deviatoric stress  $q$ , is proposed in the present work:

$$q \geq q_{CN} \quad (\text{V.6})$$

In order to take into account the strength improvement due to the increases of coordination number, the particle strength  $q_{CN}$  is proposed as follows:

$$q_{CN} = \begin{cases} q_s, & p \leq p_s \\ q_s + M_t(p - p_s), & p > p_s \end{cases} \quad (\text{V.7})$$

where  $q$  and  $p$  are respectively the current deviatoric and mean stresses.  $q_s$  and  $p_s$  are respectively the initial strength and the corresponding mean stress. The incremental stress ratio  $M_t$  describes the relation between the deviatoric stress increment and the mean stress increment. Here,  $M_t$  is roughly deemed equal to the stress ratio  $M$  used in Cam-clay model

(Roscoe et al., 1963), which can be estimated as:

$$M_t = \frac{6 \sin \varphi_{rock}}{3 - \sin \varphi_{rock}} \quad (V .8)$$

where  $\varphi_{rock}$  is the friction angle of the parent rock. The part  $M_t(p - p_s)$  in Eq. V .7 implicitly reflects the effect of coordination number on particle strength. When  $M_t = 0$ , the proposed criterion can degrade into the standard deviatoric stress type breakage criterion (McDowell and de Bono, 2013), which is largely used in the literature to study the crushing of granular materials.

The relation between  $q_s$  and  $p_s$  can be described by the initial stress ratio  $M_s$ , as

$$M_s = \frac{q_s}{p_s} \quad (V .9)$$

The values of  $q_s$  and  $p_s$  can be determined by using the single-particle crushing tests. For instance, in single-particle crushing tests, the particle is crushed with  $CN = 2$  and the corresponding  $M_s$  of 3 (de Bono and McDowell, 2016a). Inspired by the research work of Jaeger (1967), the tensile strength in single-particle crushing tests, can be measured as:

$$\sigma_f = \frac{F}{d^2} \quad (V .10)$$

where  $\sigma_f$  is the tensile stress at failure,  $F$  the diametral compressive force applied by the platens and  $d$  is the particle diameter at failure. Therefore, the values of  $q_s$  and  $p_s$  can be obtained by:

$$q_s = \frac{6}{\pi} \sigma_f; p_s = \frac{q_s}{M_s} = \frac{2}{\pi} \sigma_f \quad (V .11)$$

In Fig. V .5, it can be seen that the breakage of some agglomerates is even seen when  $p < p_s$ . This observation may be due to two phenomena. The first phenomenon is the artificial choice of 5% of cumulative broken bonds as the limit of particle failure. The second one is the anisotropic structure of agglomerate due to the fact that the bonded balls inside the agglomerate are generated in hexagonal close packing (HCP). Moreover, one observes that the slope of the regression line is almost parallel to that of the  $q = Mp$  line. This observation confirms the choice of  $M$  to describe the  $p - q$  relation. Note that only the data points in the zone with  $p > p_s$  (shaded area in Fig. V .5) are used for the linear regression.

According to the initial material strength  $q_s$ , experimental investigation (Xiao et al., 2020) exhibits that the crushing strength of particles varies with its size: the particle strength decreases with increasing particle size. This observation can be explained by

the fact that large particles have more and bigger flaws than small ones (Alonso et al., 2012; Lade et al., 1996; Zhou et al., 2016). According to the work by McDowell & Amon (McDowell and Amon, 2000), the size effects of particle strength can be described in the form  $\sigma \propto d^{-b} = d^{-3/m}$ . The characteristic particle strength  $q_0$  can be described by the following equation:

$$q_0 \propto d^{-b} = d^{-3/m} \quad (\text{V .12})$$

Based on Weibull theory (Weibull, 1951), the survival probability  $P_s(V_0)$  for a particle with the volume  $V_0$  under a tensile stress  $q_s$  can be given by:

$$P_s(V_0) = \exp[-(\frac{q_s}{q_0})^m] \quad (\text{V .13})$$

where  $q_0$  is the characteristic strength, at which 37% of the samples survive. The Weibull modulus  $m$  describes the distribution of particle strength with a given particle size, and it can be obtained by single-particle crushing tests. The cumulative function of Weibull distribution can be given as:

$$P_f(V_0) = 1 - P_s(V_0) = 1 - \exp[-(\frac{q_s}{q_0})^m] \quad (\text{V .14})$$

which is the failure probability of one particle. The inverse function of  $P_f(V_0)$  can be expressed as:

$$q_s = P_f^{-1}(V_0) = q_0[\ln(1 - P_f(V_0))^{-1}]^{1/m} \quad (\text{V .15})$$

Here, the particle strength  $q_s$  will obey the Weibull distribution if  $P_f(V_0)$  follows the standard uniform distribution  $U(0, 1)$ . Replace  $P_f(V_0)$  by  $U(0, 1)$ , the particle strength  $q_s$  can be given as

$$q_s = q_0[\ln(1 - U(0, 1))^{-1}]^{1/m} \quad (\text{V .16})$$

The current particle strength  $q_{CN}$  can then be obtained based on the initial particle strength  $q_s$  by Eq. (V .7). Eq. (V .12) describes the fact that particle strength decreases with increasing particle size, which is the size-hardening law for natural crushable particles, e.g., sand, rockfill, etc. Eq. (V .16) illustrates that the particle strength with a given size follows the Weibull distribution law. And finally, Eq. (V .7) in  $q_{CN}$  breakage criterion indicates the effect of coordination number on the particle strength. By using the Eqs. (V .7, V .12, and V .16), the strength of the surviving particles and new fragments can be calculated with the consideration of the size-hardening law, the Weibull distribution and the  $CN$  effect. The detail of the breakage detection and the allocation of particle strength

is shown in Fig. V .6. When the breakage is detected, the information of the particle (position, radius, stress tensor) will be recorded for subsequent fragments spawning, rotating and expanding.

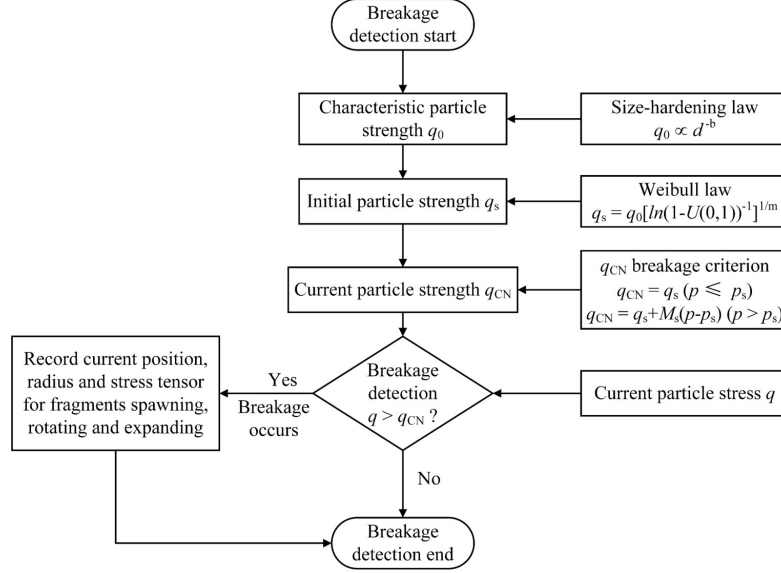


**Figure V .6:** Numerical procedure of breakage detection in population balance model (PBM)

### 3.2 Simulation setup

The proposed criterion is then implemented in the software YADE. The oedometer tests realized by Xiao et al. (2020) will be used for the verification of proposed criterion. As a result, for the particles under multiple contact ( $CN \geq 2$ ), the particle crushing occurs when its actual value of deviatoric stress  $q$  is either equal to or greater than its strength  $q_{CN}$  ( $q \geq q_{CN}$ ).

In the numerical simulation of the particle crushing, one important issue in the particle spawning approach is the mass conservation because any loss of mass will alter the macro-mechanical behavior and the evolving PSD (de Bono and McDowell, 2016a). Therefore, several methods have been proposed, e.g., the expanding fragment method (Ben-Nun and Einav, 2008, 2010; Zhou et al., 2020), the overlap method (de Bono and McDowell, 2016a; McDowell and de Bono, 2013; Zhou et al., 2016) and the insertion of small particles into the voids (Aström and Herrmann, 1998; Elghezal et al., 2013; Hanley et al., 2015; Tapias et al., 2015; Tsoungui et al., 1999) in the literature. In order to reduce the influence of unphysical pressure and guarantee a high computing performance, the expanding fragment method is use in the present study.

Fig. V.7 shows the schematic of particle breakage in population balance model (PBM). During the simulation, the stress applied on each particle is calculated and then compared with the breakage criterion. When the stress state of parent particle (Fig. V.7a) satisfies the breakage criterion, two equally sized fragments (Fig. V.7b) will be generated to replace the parent particle. The two fragments are then rotated to make sure that the axis joining their centres along the direction of the minor principal stress. This rotation just mimics the failure pattern of particles under two opposite forces. Finally, the fragments are expanded in a few steps to guarantee the mass conservation during particle breakage.

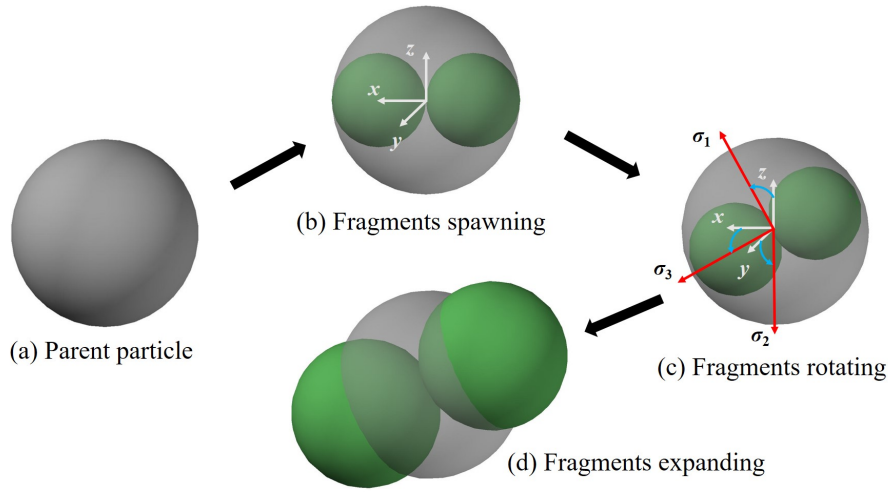


**Figure V.7:** Schematic of particle breakage in population balance model (PBM)

In the laboratory, the oedometer tests are performed under quasi-static condition. However, the crushing of particles may induce a local and small dynamic reaction due to the release of strain energy stocked in the broken particles. Moreover, in the numerical simulation, the fragments expansion will create unphysical energy, which leads the system into an unreasonable dynamic state. Zhou et al. (2020) proposed the quasi-static criterion to divide the simulation into two state: quasi-static and dynamic. In the dynamic state, the particle breakage and fragments expansion can lead the system to an unrealistic dynamic condition, in which energy and unbalanced force are much larger than that in the quasi-static condition. To avoid non-physical mechanical response or energy accumulation due to the fragments expansion, the system will fall into the dynamic state once the particle breakage occurs, in which the timestep is dramatically shorter (reduced timestep, one-tenth of the normal timestep in present study) than the normal timestep in quasi-static state. The system will get back to the quasi-state state with normal timestep if the quasi-static detection is satisfied. However, once the timestep is set back to the normal



value, the system may still in an unsteady state due to the dramatic increase of timestep. Consequently, a critical state is adopted here as a transitional state between quasi-static and dynamic states. In the critical state, the timestep is set back to normal but the system is still outside of the quasi-static state. The detail of breakage processor is given in Fig. V .8. The critical state detection connects the two principal states: quasi-static and dynamic. During the crushing of particles and the expanding of their fragments, the loading process and the breakage detection are paused. The maximum unbalanced force criterion is considered in the critical state detection. After that, the system will be in the critical state. Here, inspired by the previous work of McDowell and de Bono (2013), the quasi-static state detection is realized by detecting particle breakage after a certain time interval (0.001 s in present study). If no particle breakage occurs, the system will get back to the quasi-static condition and the mechanical loading is restarted.

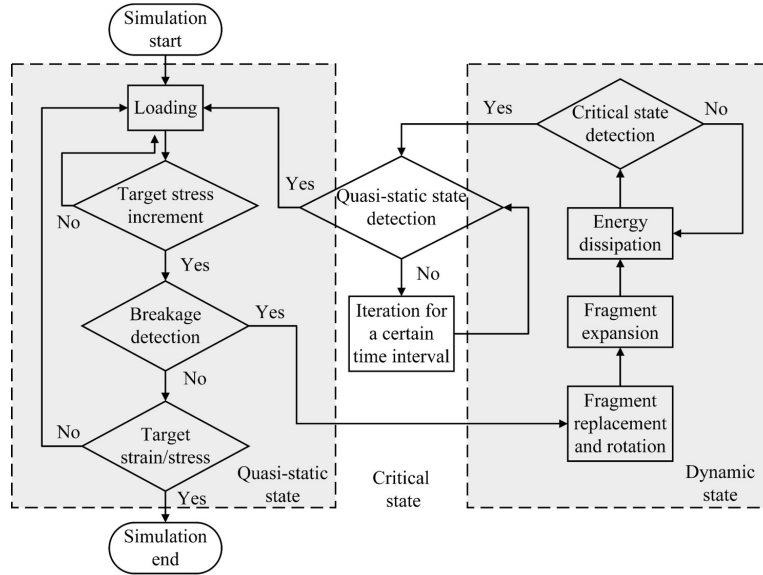


**Figure V .8:** Numerical procedure of particle breakage in population balance model (PBM)

## 4 Numerical simulation of oedometer tests

Three oedometer test with different nominal particle sizes  $d_n$  (2.5, 5.0 and 10.0 mm) are studied in this section. The numerical samples are prepared by depositing the particles in a cylindrical rigid container under gravity. They are then preliminarily compressed by the upper wall with a vertical stress of 30 kPa. The friction angle is set to 0 in the depositing procedure to get a dense packing and is reset to its normal value before the application

of compression. By using the samples with similar geometry, three sizes of cylindrical containers with diameters 25, 50 and 100 mm are used for the samples with  $d_n = 2.5, 5.0$  and 10.0 mm, respectively. The particles in the three samples are respectively generated following a uniform distribution of particle size  $2.2 \sim 2.8, 4.7 \sim 5.3$  and  $9.7 \sim 10.3$  mm for  $d_n = 2.5, 5.0$  and 10.0 mm. The details of three sample sizes are given in Table V .2.

**Table V .2:** DEM parameters for three sample sizes

Nominal diameter (mm)	Container size: height $\times$ diameter (mm)	Characteristic stress (MPa)	Initial grading (mm)	Initial void ratio	$q_s$ (MPa)	$M_s$	$M_t$
2.5	25 $\times$ 25	8.05	2.2 $\sim$ 2.8	0.83	15.37	3	0.3
5.0	50 $\times$ 50	4.61	4.7 $\sim$ 5.3	0.88	8.80	3	0.3
10.0	100 $\times$ 100	2.25	9.7 $\sim$ 10.3	0.86	4.35	3	0.3

The main DEM parameters are listed in Table V .3 while the specific parameters for three sample are given in Table V .2. The Hertz-Mindlin contact model is adopted in the simulations. The simulation is run in a stress-controlled mode. Firstly, the sample is loaded by a given macroscopic stress increment. The particles are then checked and replaced by fragments if the breakage criterion is attained. If breakage happens, the breakage detection is temporarily stopped until the particles are balanced again. The sample is then re-applied to the current stress level and the breakage is checked again. The sample will be applied for the next stress level if no particle breakage happens. The macroscopic stress increment used is 125 kPa. The maximum velocity of upper loading wall is respectively limited to 0.005, 0.010 and 0.020 m/s for  $d_n = 2.5, 5.0$  and 10.0 mm to guarantee the same loading strain rate. For reason of simplicity, the gravity is neglected in the numerical simulation.

In DEM, the computation time depends on not only the particle numbers but also the minimum particle size. In order to guarantee the computational efficiency, the minimum particle size should be limited to a certain value, called  $d_{limit}$ . On the other hand, the  $d_{limit}$  value should be small enough to assure the simulation accuracy. In the literature, different values of  $d_{limit}$  have been used. McDowell & de Bono (2016b) adopted the  $d_{limit} = 0.04d_M$  in their simulations, where  $d_M$  is the maximum particle size. Ciantia et al. (2015) have used  $d_{limit} = 0.25d_{50}$ , where  $d_{50}$  is the mean particle size. Recently, Zhou et al. (2020) used a smaller value of  $d_{limit} = 0.015d_M$  in their simulations, in which the balls are small

enough to get a correct macroscopic response and a realistic PSD evolution. In view of this, the minimum particle size is set as  $d_{limit} = 0.015d_{50}$  in the present study.

**Table V .3:** Main DEM parameters in the oedometer test on rockfill materials

Parameter	Value
Ball density (kg/m <sup>3</sup> )	2500
Ball Young's modulus (GPa)	1.1
Ball Poisson's ratio	0.25
Ball friction angle (rad)	0.35
Initial number of balls	600
Weibull modulus, $m$	3.24
Wall Young's modulus (GPa)	200.0
Wall Poisson's ratio	0.30
Wall friction angle (rad)	0.00
Damping coefficient	0.5

#### 4.1 Parametric study

In order to understand the influence of three parameters ( $q_s$ ,  $M_s$  and  $M_t$ ) in the proposed breakage criterion on the macroscopic behaviour of rockfill materials, the oedometer tests with the nominal particle size  $d_n = 2.5$  mm are simulated. The scheme of the parametric study is given in Table V .4 while other DEM parameters can be found in Tables V .2 and V .3.

**Table V .4:** Scheme of parametric study for oedometer test

Influencing factor	Case number	$q_s$ (MPa)	$M_s$	$M_t$
Reference	1	15.37	3.0	0.3
$q_s$	2 ~ 4	<b>5.00~30.00</b>	3.0	0.3
$M_s$	5 ~ 8	15.37	<b>0.5~6.0</b>	0.3
$M_t$	9 ~ 12	15.37	3.0	<b>0~1.5</b>

The influence of  $q_s$  on macroscopic behaviors of samples in oedometer tests is given in Fig. V .9. Fig. V .9a shows the vertical stress  $\sigma_v$  versus vertical strain  $\varepsilon_v$  curves obtained with different values of initial particle strengths  $q_s$ . The modulus of compressibility  $E_s$  (the slope of the  $\sigma_v$ - $\varepsilon_v$  curve) is significantly affected by  $q_s$ :  $E_s$  increases with the increase of  $q_s$ . The relationship between the void ratio  $e$  and vertical stress  $\sigma_v$  are given in the double logarithmic scale (Fig. V .9b). When the initial strength  $q_s$  increases, the yield point appears at higher level of stress. The particle size distribution curves of samples with different  $q_s$  are presented in Fig. V .9c. It can be observed that  $q_s$  has a pronounced effect on the shape of PSD. Samples with small  $q_s$  will suffer more particle breakages under the same level of vertical stress. Therefore, a more developed PSD can be obtained in the case with small  $q_s$ .

The influence of  $M_s$  on the macroscopic behaviour of samples in oedometer tests is given in Fig. V .10. Figs. V .10a and b indicate that the initial stress ratio  $M_s$  has no pronounced effects on the modulus of compressibility  $E_s$  and the normal consolidation line (NCL). However, the PSD is affected by  $M_s$ : the sample with a small value of  $M_s$  suffer more particle breakages for a given level of vertical stress (Fig. V .10c). For particles with a given initial strength  $q_s$ , a big value of  $p_s$  is obtained by using a low value of  $M_s$ . As  $p_s$  is the initial mean stress, it controls the activation of the  $CN$  effect on particle strength. As a result, the strength improvement can only be activated under a high mean stress and the particles are more likely to break at low stress level.

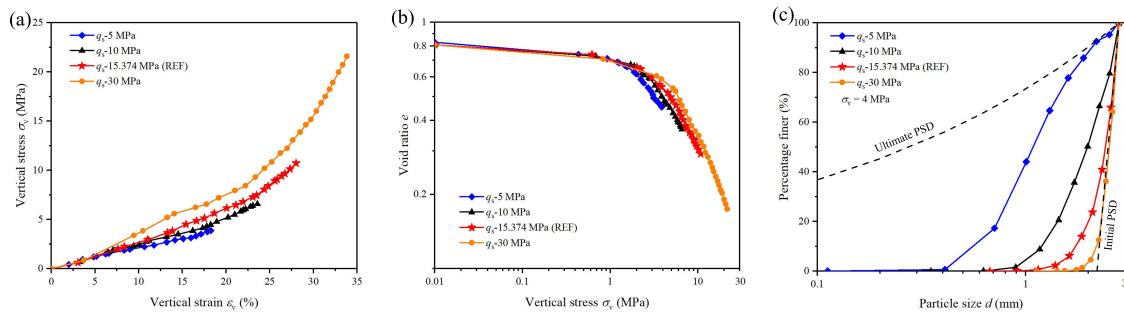


**Figure V .9:** Effect of parameter  $q_s$  on the macroscopic response in oedometer tests for samples with nominal diameters  $d_n = 2.5$  mm: (a) vertical stress and vertical strain; (b) void ratio and vertical stress in the double logarithmic scale; (c) particle size distribution after compression at 4 MPa of vertical stress

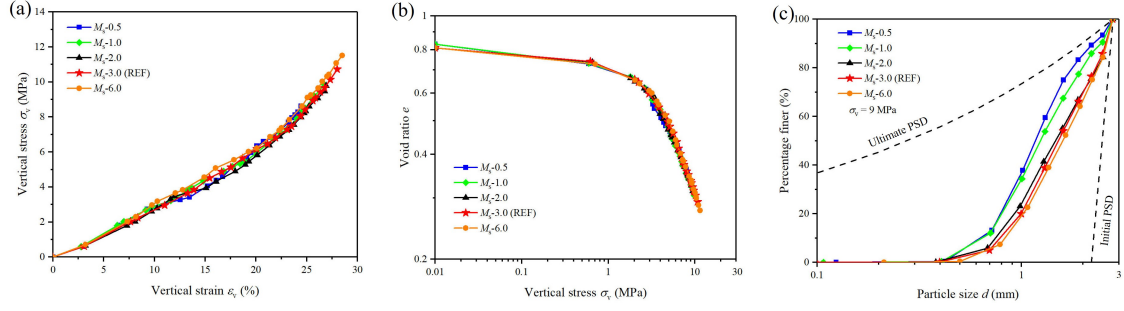


**Figure V .10:** Effect of parameter  $M_s$  on the macroscopic response in oedometer tests for samples with nominal diameters  $d_n = 2.5$  mm: (a) relationship between the vertical stress and vertical strain; (b) relationship between the void ratio and vertical stress in the double logarithmic scale; (c) particle size distribution after compression at 9 MPa of vertical stress

The simulation results with different values of  $M_t$  are presented in Fig. V .11. Fig. V .11a shows that the incremental stress ratio  $M_t$  has a pronounced effect on the modulus of compressibility  $E_s$ , i.e.,  $E_s$  increases with the increase of  $M_t$ .  $M_t$  has also an important impact on the post-yield part of the NCLs (Fig. V .11b). It should be noted that the shape of PSDs is sensitive to the value of  $M_t$  (Fig. V .11c). Specifically, when  $M_t$  is small ( $M_t = 0.0$ ), the PSD is in a sigmoid shape. With the increase of  $M_t$ , the shape of PSD is changed from straight line type to the hyperbola type. In the case with  $M_t = 1.5$ , a non-realistic mechanical response is observed due to excessive restraint of particle breakage. Consequently, the recommended value of  $M_t$  is in the range of  $0 \sim 1.0$ .

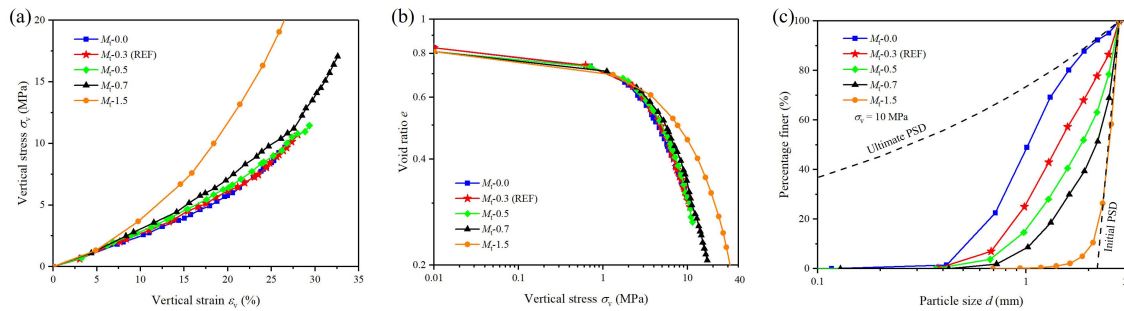


**Figure V .11:** Effect of parameter  $M_t$  on the macroscopic response in oedometer tests for samples with nominal diameters  $d_n = 2.5$  mm: (a) vertical stress and vertical strain; (b) void ratio and vertical stress in the double logarithmic scale; (c) particle size distribution after compression at 10 MPa of vertical stress

## 4.2 Numerical simulation of the oedometer test with the nominal diameter $d_n = 2.5$ mm

In this section, the principal results of the oedometer test with nominal diameter  $d_n = 2.5$  mm are presented to validate the proposed breakage criterion.

The vertical stress  $\sigma_v$  versus vertical strain  $\epsilon_v$  curves are given in Fig. V.12a. A good agreement is obtained between the numerical simulations and experimental data. The increase of compressibility modulus of studied rockfill materials is satisfactorily reproduced by the numerical simulation. In addition, the  $\sigma_v$ - $\epsilon_v$  curve obtained neglecting the particle breakage is also given (dash-dotted line) in Fig. V.12a. It can be seen that without crushing, the model curve is too far from the test data.

The normal consolidation line (NCL) is presented in Fig. V.12b. The numerical results and laboratory data exhibit the same shape. Moreover, the yield point in numerical and experimental results appear at the same level of vertical stress. In addition, one observes that the NCL without crushing (dash-dotted line) cannot approximate the test data. The NCL with the particle crushing diverges from the one without crushing at the yielding point. This observation confirms the fact that the yield point in oedometer test is the onset of particle breakage (Guida et al., 2018; McDowell and Bolton, 1998; McDowell and Humphreys, 2002; Nakata et al., 2001a). Note that the NCL without crushing begins to bend when vertical stress  $\sigma_v$  exceeds 10 MPa. This phenomenon is due to the particle overlap (Ciantia et al., 2015; Masín, 2012).

Based on the work of McDowell & de Bono (2013), the NCL after yielding can be described as

$$\log e = \log e_y - \frac{1}{2b} \log \frac{\sigma}{\sigma_y} \quad (\text{V.17})$$

where  $e$  and  $e_y$  are respectively the voids ratio at present and at the yield point,  $\sigma$  and  $\sigma_y$  are respectively the current stress and yield stress. The parameter  $b$  describes the size-hardening law of particles, and its value can be estimated as  $b = 3/m = 3/3.24 = 0.93$  in our study, see Eq. (V.12).

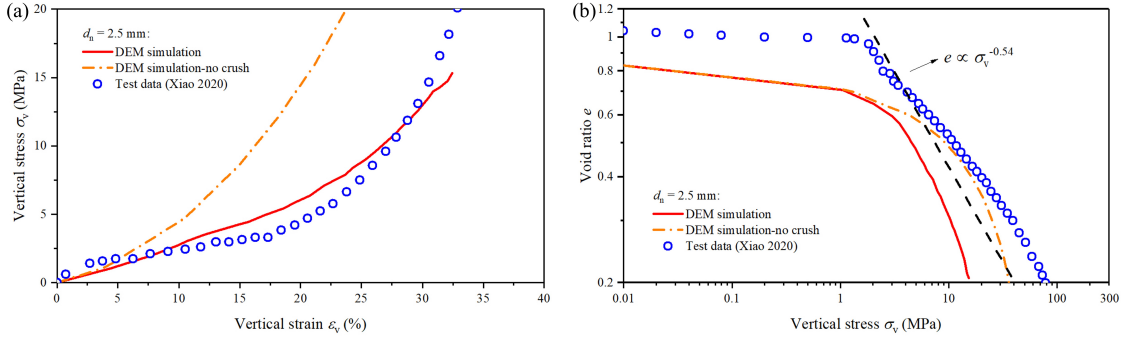


**Figure V .12:** Simulation results of the oedometer test with the nominal diameter  $d_n = 2.5$  mm: (a) the vertical stress and vertical strain curves and (b) the void ratio and vertical stress in the double logarithmic scale

The ideal slope predicted by Eq. (V .17) is shown as the black dashed line (Fig. V .12b), with a value of 0.54. It can be seen that the the numerical and experimental results are approximately parallel during the yield stage, and the slopes of them finally approach the black dashed line. Therefore, the influence of particle size on the the mechanical characteristics of rockfill materials is satisfactorily reproduced by the the numerical simulations.

Based on the previous work of Tyler & Wheatcraft (1989), the fractal grading can be expressed as

$$F_u(d) = \left(\frac{d}{d_M}\right)^{3-D} \quad (\text{V .18})$$

where  $F_u(d)$  is the percentage finer,  $d_M$  is the largest particle size and  $D$  is the fractal dimension. The fractal dimension  $D$  is usually in the range of 2.0 ~ 3.0 for the granular materials in compression (de Bono and McDowell, 2016b). Based on the research work of Xiao et al. (2020), the value of the ultimate dimension of  $D = 2.7$  can be used for the studied rockfill samples.

With the increase of applied stress, the particle size distribution (PSD) curve approaches to the ultimate one due to the continuous particle breakage. The simulation of particle size distribution lines with  $d_n = 2.5$  mm are given in Fig. V .13a. The progressive evolution of PSDs with the increase of applied stress is satisfactorily reproduced by the numerical simulations, especially in the right-hand part. However, it should be noted that for DEM simulation, the number of small particles is still less than the test data. This phenomenon is related to several factors, i.e., the comminution limit, the stress increment mode for breakage detection, the selection of two equally sized balls as the fragment replacement mode, etc. Zhou et al. (2020) compared three different fragment modes and

found that the breakage of small particles was restrained by using two equally sized balls. Less number of small particles will also induce more breakage of large particles since there are not enough small particles to protect the large ones.

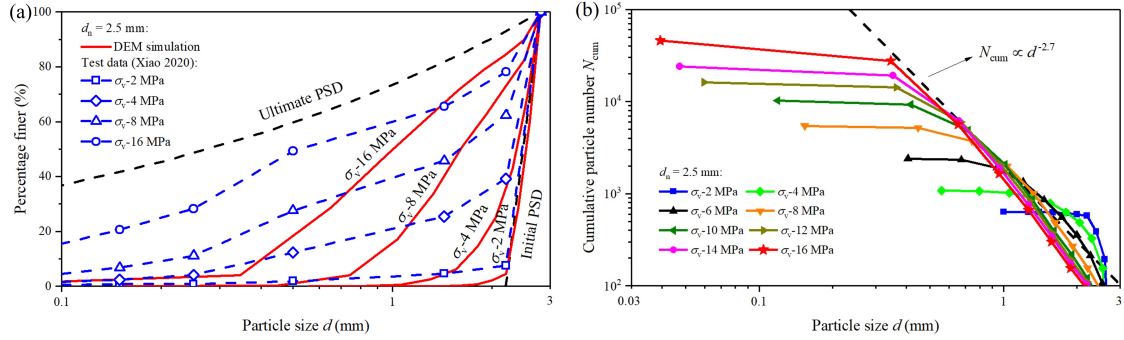


**Figure V .13:** Evolution of particle size distribution curves in the oedometer tests for the sample with nominal diameter  $d_n = 2.5$  mm: (a) mass distribution and (b) number distribution

The PSD can also be represented by the particle numbers. According to the work by Turcotte (1986), a fractal behaviour of PSD can be given as

$$N_{cum} \propto d^{-D} \quad (\text{V} .19)$$

where the cumulative particle number  $N_{cum}$  is the particle number larger than  $d$ . Eq. (V .19) indicates that in the  $N_{cum} - d$  curve plotted in two logarithmic scale, a linear PSD will emerge with the fractal dimension as the slope. The evolutions of cumulative particle number are given in Fig. V .13b. A reference curve with  $D = 2.7$  is drawn for ease of comparison. It can be seen that the right-hand sections of the PSDs become linear with the slope close to the fractal dimension. This observation indicates that the fractal dimension emerges in the PSDs. The left-hand section still diverges from the fractal dimension since the breakage of small particles has still not been well developed. With the continuous breakage of particles, the left-part of PSD will progressively approach to the fractal line.

The numerical samples with  $d_n = 2.5$  mm before and after the compression ( $\sigma_v = 16$  MPa) are shown in Fig. V .14. Additionally, the corresponding force chain networks are given in Fig. V .15.



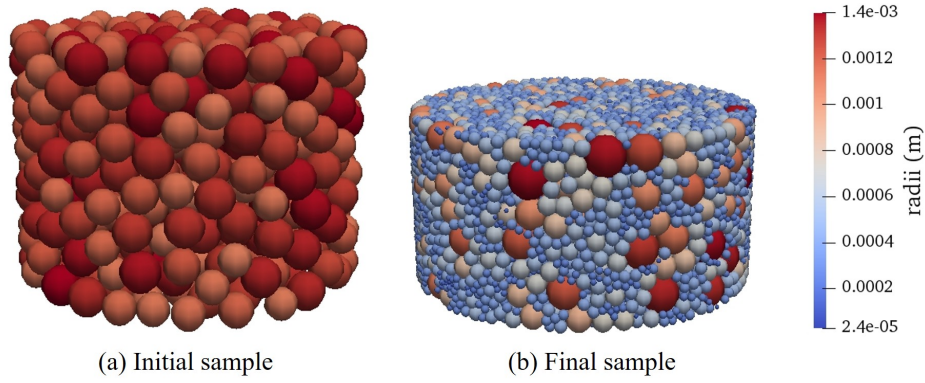


**Figure V .14:** Numerical sample with  $d_n = 2.5$  mm: (a) before compression and (b) after compression ( $\sigma_v = 16$  MPa)

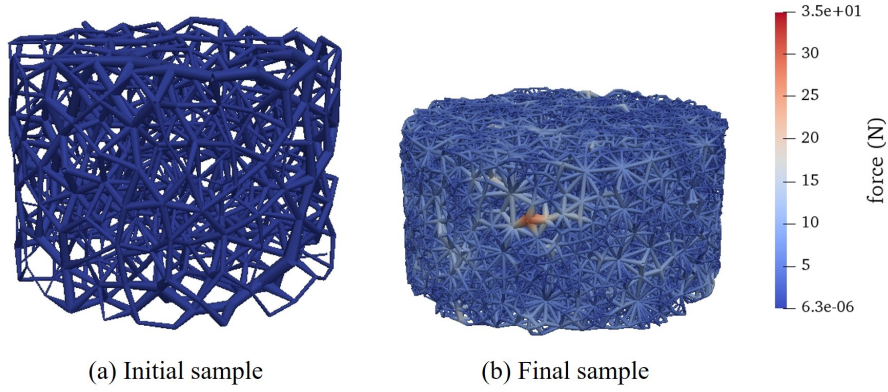


**Figure V .15:** Force chain network inside the numerical sample with  $d_n = 2.5$  mm: (a) before compression and (b) after compression ( $\sigma_v = 16$  MPa)

### 4.3 Numerical analysis of the effects of particle size

In this section, the numerical simulation of three oedometer tests with different nominal particle diameters  $d_n$  (2.5, 5.0 and 10.0 mm) are compared in order to study the influence of particle size on the mechanical behavior of studied rockfill materials.

Fig. V .16a presents vertical stress versus vertical strain curves. The influence of particle size on the deformation behavior of rockfill materials is satisfactorily captured by the numerical simulation: at a given strain level, the vertical stress increases with the decrease of particle size. The compressibility modulus of studied rockfill materials increases with decreasing particle size. This phenomenon can be explained by the fact that small particles process high strength and then are capable of bearing high vertical loads before crushing. However, the numerical curves is stiffer than the laboratory ones

due to the fact that less number of small particles is created in the DEM simulations.

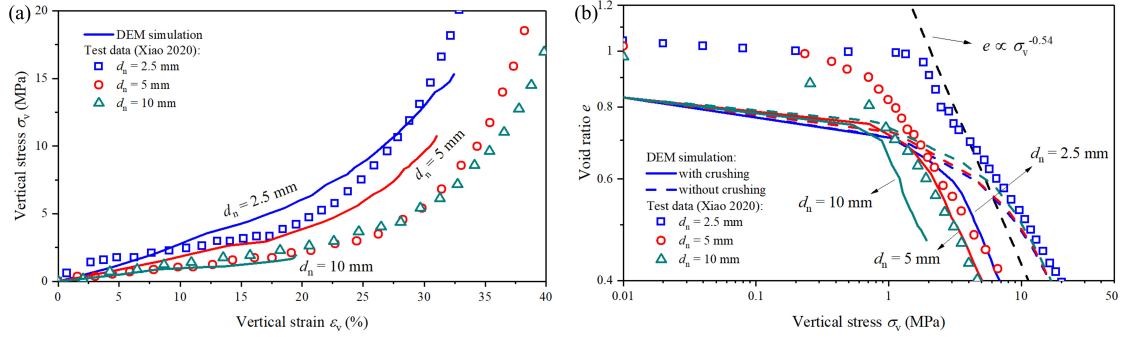


**Figure V.16:** Numerical simulations of oedometer tests with three nominal diameters ( $d_n = 2.5, 5.0$  and  $10.0$  mm): (a) vertical stress and vertical strain curve and (b) void ratio and vertical stress curve plotted in the double logarithmic scale

The NCLs for different  $d_n$  are given in Fig. V.16b. In general, the numerical and experimental results present the similar shape. At the yield stage, the NCLs with different  $d_n$  are approximately parallel to one another while the slopes of them approach that of the dashed line predicted by Eq. (V.17). Again, the effect of particle size on the mechanical behavior of studied rockfill materials is well reproduced by the numerical simulations. In addition, the yield point shifts rightward with the decrease of particle size, indicating that the yield stress increases with the decrease of particle strength. This observation confirms previous studies that the yield stress is related to the particle strength (McDowell and Humphreys, 2002; Nakata et al., 2001b). In short, the size-hardening law and initial particle strength control the compressive behaviour of crushable granular materials.

Note that the NCLs of three tests without crushing almost overlap each other at the yield stage, indicating that particle breakage is the origin of size effects on RFM. This observation is consistent with the DEM results of Zhou et al. (2016) in their study on the effect of particle size on the triaxial samples. In the present study, it should be noted that the particle size effects on the particle shape and particle surface roughness are not considered.

## 5 Comparison of the proposed breakage criterion with different breakage criteria

In previous sections, the  $q_{CN}$  criterion has been validated by a satisfactory reproduction of macro-mechanical behavior of rockfill materials and the emergence of fractal in the

particle size distribution. In order to get a deeper understanding of the  $q_{CN}$  criterion in the function of particle breakage, the numerical results of  $q_{CN}$  criterion are compared with those performed by using  $q_{oct}$ ,  $\sigma_{Fm}$ ,  $\sigma_1$  and  $p$  as breakage indexes. In this section, only the sample with nominal diameter  $d_n = 2.5$  mm is used. The simulation results by using different criteria will be compared. The evolution of coordination number and particle stress will also be discussed.

### 5.1 NCL and PSD

The NCLs with five breakage criteria are given in Fig. V.17a. It can be seen that the NCLs at the yield stage are approximately parallel to one another, and the slopes of them finally approach the dashed line (given by Eq. (V.17)).

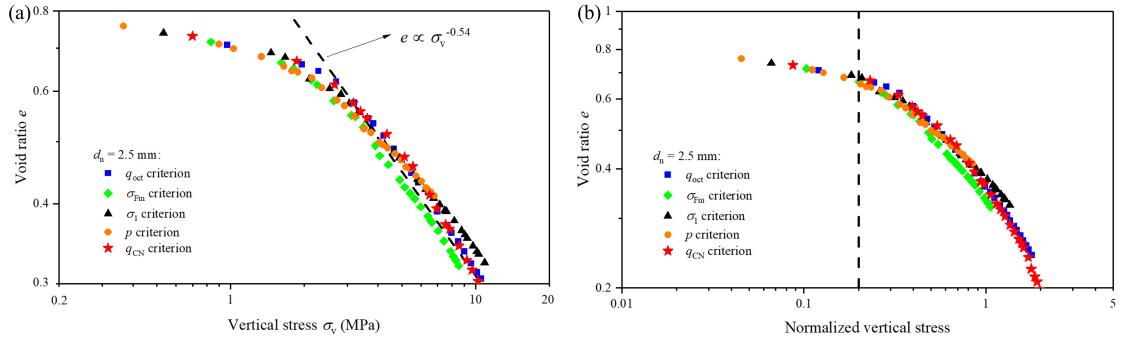


**Figure V.17:** Numerical simulation of the oedometer by using different breakage criteria: (a) void ratio and vertical stress curve in the double logarithmic scale and (b) void ratio and normalized average particle stress

The void ratio against the normalized vertical stress  $\sigma_v/\sigma_0$  curves are given in Fig. V.17b. The NCLs almost yield at the same normalized vertical stress of 0.2 (shown as the vertical dashed line) regardless of breakage criteria. The yield value agrees with the simulation results on sand (de Bono and McDowell, 2016a). In practice, McDowell & Humphreys (2002) concluded that the region of maximum curvature is at  $\sigma_v/\sigma_0 \approx 0.1 \sim 0.3$  in oedometer tests on several weak granular materials. This observation is due to the fact that as one quarter particles participated in the strong force chain, the yield stress was approximately 25% of the particle strength.

The final PSDs of five breakage criteria are given in Fig.V.18a. Note that the corresponding vertical stresses for five criteria are different since the simulations are terminated when there is a large number of particles covering a wide range of sizes, which occurs at different stresses for five cases. One observes that only the PSD of  $q_{CN}$  criterion is closer

to the ultimate one while fractal emerges in the PSDs by using  $q_{CN}$ ,  $q_{oct}$  and  $\sigma_{Fm}$  criteria. As the influence of  $CN$  on particle strength is not considered in the  $q_{oct}$  and  $\sigma_{Fm}$  criteria, an important crushing of large particles is observed in the curves by using  $q_{oct}$  and  $\sigma_{Fm}$  criteria. However, in the cases using  $\sigma_1$  and  $p$  criteria, present an excessive breakage of large particles, and the PSDs are not fractal in character.

The final PSDs for five breakage criteria are given in the  $N_{cum} - d$  plot (Fig. V.18b). It can be seen that in the cases of  $q_{CN}$ ,  $q_{oct}$  and  $\sigma_{Fm}$  criteria, the right-hand sections of the PSDs become linear with the slope close to the fractal dimension. This means the fractal dimension emerges in these PSDs. In contrast, the curvatures of the PSDs for  $\sigma_1$  and  $p$  criteria indicate that no fractal behaviours can be observed in these two cases.

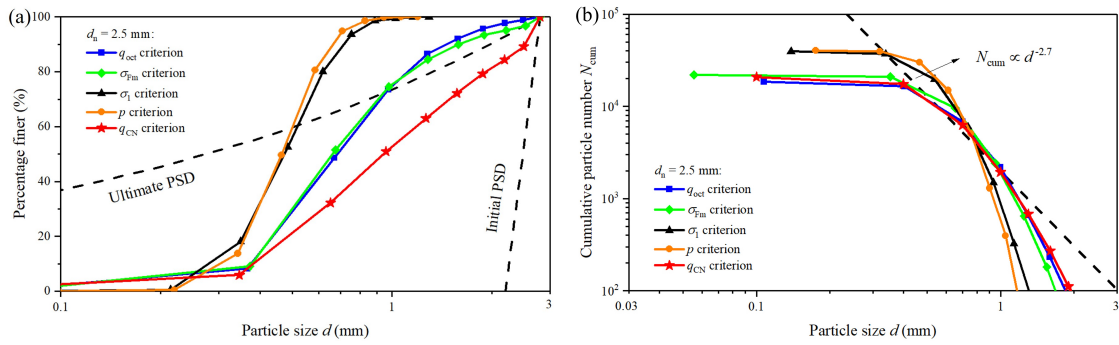


**Figure V.18:** Particle size distribution after compression under different breakage criteria: (a) mass distribution and (b) number distribution

## 5.2 Evolution of $CN$

In this section, the evolution of coordination number  $CN$  is analyzed to understand the dependence of particle crushing on the breakage criterion. The final proportion of particles with different  $CNs$  is presented in Fig. V.19. In practice, the particles with  $CN = 0$  means no neighbouring particles around them, and they float in the assembly with no contribution to the load-bearing network. Based on the previous work (de Bono and McDowell, 2016b; Zhou et al., 2020), the particles with  $CN = 1 \sim 3$  are in a transitory state, and the minimum value of  $CN$  for a load-carrying particle would be 4. The final proportion of particles with different  $CNs$  is given in Fig. V.19. Similar distributions of  $CN$  are observed in the cases with different criteria. In the case with  $q_{CN}$ , up to 3% particles have no contacts, but these particles only occupy about 0.2% of the total mass. Consequently, in the following study, particles with  $CN = 0, 1$  are neglected for the calculation of average  $CN$  in order to avoid the stress deviation induced by these floating

particles.

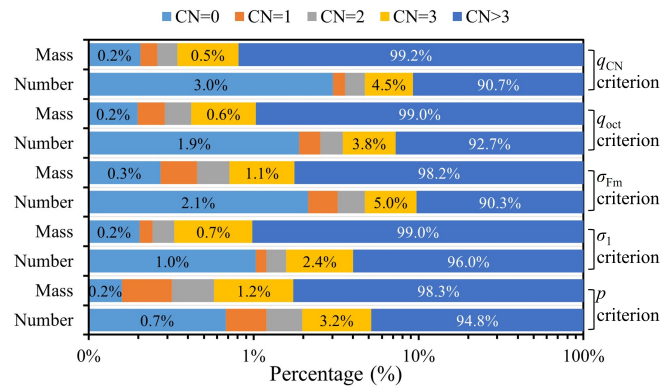


**Figure V .19:** Final proportion of different  $CN$ s with respect to mass and number by using different breakage criteria

Fig. V .20 shows the evolution of average  $CN$  by using different breakage criteria. Generally, the average  $CN$  increases with the increase of vertical stress. This observation is due to the increase of small fragments caused by particle comminution. On the other hand, the increase of  $CN$  in the large particles indicates that large particles are surrounded by a lot of small particles in the assembly.

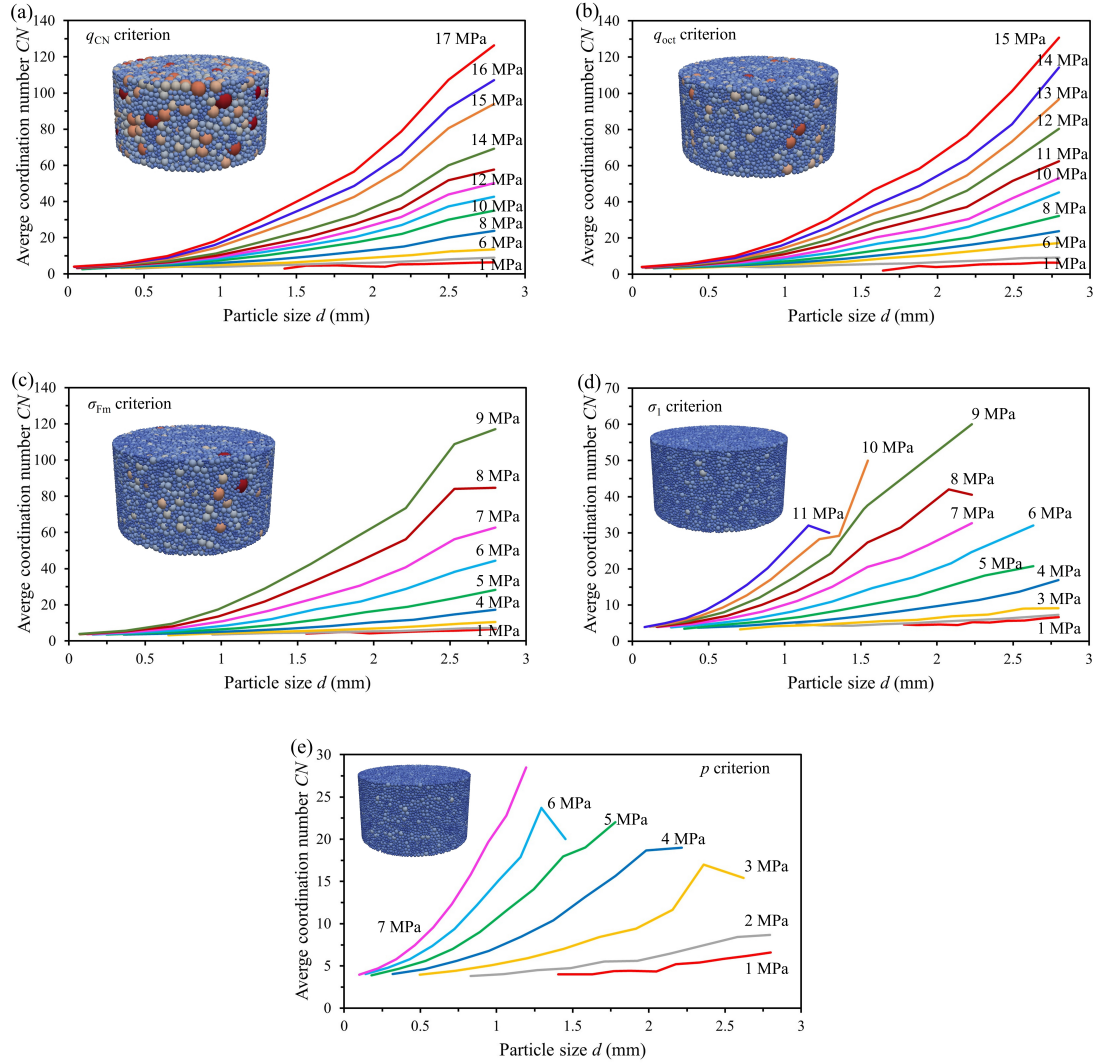


**Figure V.20:** Evolution of average coordination number  $CN$  under different breakage criteria: (a)  $q_{CN}$  criterion; (b)  $q_{oct}$  criterion; (c)  $\sigma_{fm}$  criterion; (d)  $\sigma_1$  criterion; (e)  $p$  criterion

Based on the evolution of  $CN$  obtained by using different criteria, the breakage criteria can be divided into two categories. The first group is composed of  $q_{CN}$ ,  $q_{oct}$  and  $\sigma_{fm}$  criteria, in which the  $CN - d$  lines increase gradually and a constant slope appears in the right part of them. This observation also indicates a fractal behaviour. The second type includes the  $\sigma_1$  and  $p$  criteria, in which no steady evolution is obtained because of the continuous disappearance of the large particles under compression. By comparing the results of  $q_{CN}$  with other criteria, one can conclude that the breakage criterion  $q_{CN}$  is capable of describing the mechanical behavior of studied rockill materials, and its PSD



presents a fractal trend.

### 5.3 Evolution of particle stress

To analyze the influence of breakage criterion  $q_{CN}$  on the stress states of particles, the evolutions of different average particle stresses are plotted in Fig. V .21. The calculation of average particle stresses is similar to that of  $CN$ , only considering the particles of  $CN > 1$ . Inspired by the research work of McDowell & de Bono (2013), the average particle strength  $q_m$  can be determined by the characteristic strength  $q_0$  due to the fact that the particle strength follows the Weibull distribution:

$$q_m = q_0 \Gamma\left(\frac{1}{m} + 1\right) \quad (\text{V .20})$$

where  $\Gamma$  is the gamma function. The value of  $q_m$  is nearly  $0.9q_0$  in our study. The dashed line represents the theoretical average particle strengths (based on Eqs. V .12, V .20). One observes that the particle strength increases with the particle size in the theoretical strength line, which is the typical size-hardening law. The dash-dotted line (Fig. V .21a) is the actual particle strength  $q_{CN}$  at the vertical stress of 17 MPa, which exhibits the effect of  $CN$  on particle strength.

From Fig. V .21, it is observed that the average particle stress decreases with the increase of particle size. The drop of stress for the smallest few particles should be due to the undeveloped number of these particles, as explained by de Bono & McDowell (2016b). Most of these particles are in the transitory state, with  $CN < 4$ . The slopes of the curves in the cases with  $q$ ,  $q_{oct}$  and  $\sigma_{Fm}$  are steeper than that with  $\sigma_1$  and  $p$ . For instance, in the case with the mean stress  $p$  (Fig. V .21e), most particles exhibit similar average stresses except that the small particles process a high value. In addition, all the average particle stresses increase progressively with the increase of vertical stress. In the cases of  $q$ ,  $q_{oct}$  and  $\sigma_{Fm}$ , the average stress of large particles gradually approaches a certain value, and the same phenomenon is then developed for the second large particle size successively. In contrast, in the case of  $\sigma_1$  and  $p$ , the average stress increases continuously in all sizes of particle. The right part of curves gradually approaches and exceeds the average particle strength line, indicating that all large particles will be crushed consecutively. This observation can be used to explain why there is no fractal responses in the cases of  $\sigma_1$  and  $p$  criteria.

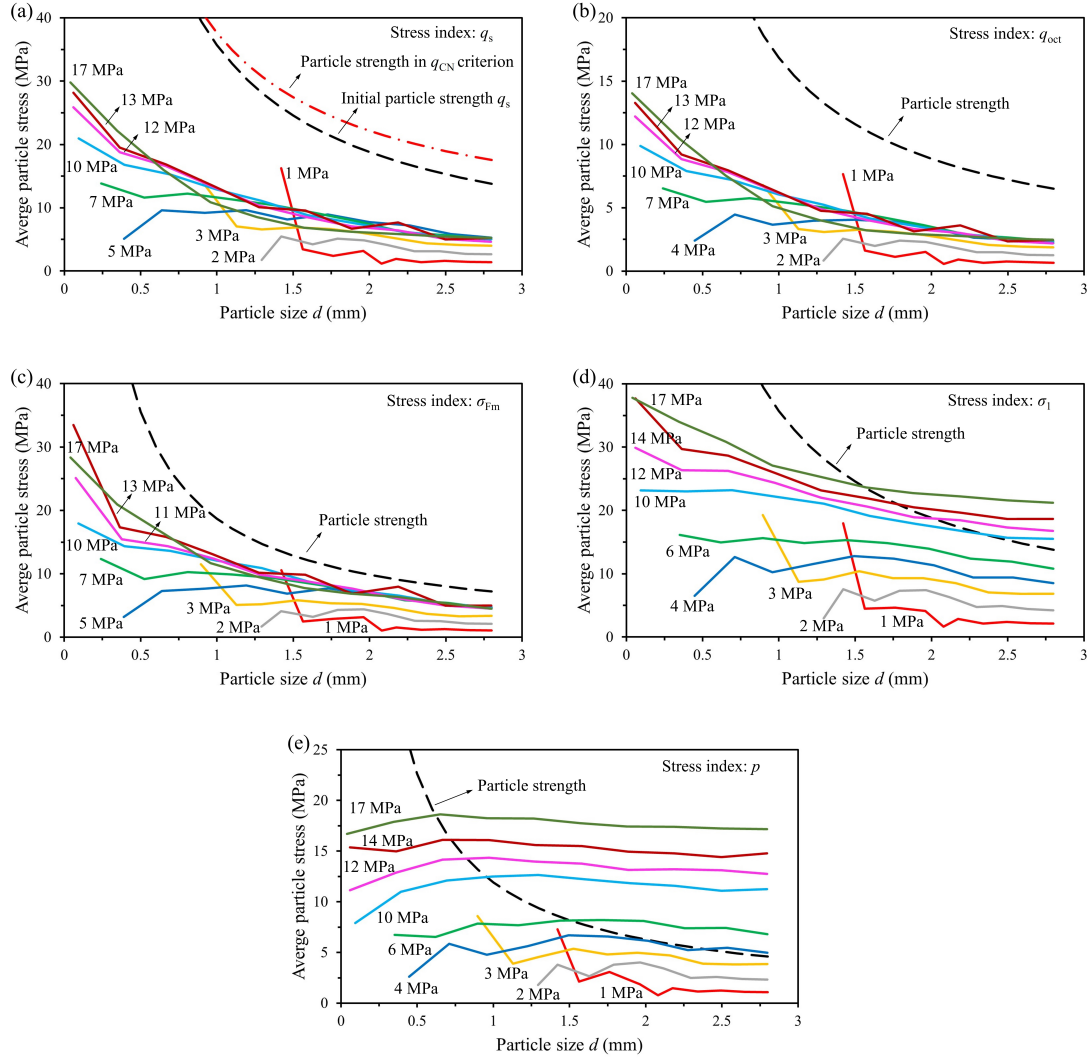


**Figure V.21:** Evolution of different average particle stresses under  $q_{CN}$  breakage criteria: (a) deviatoric stress  $q$ ; (b) octahedral shear stress  $q_{oct}$ ; (c) stress induced by the maximum normal contact force  $\sigma_{Fm}$ ; (d) major principal stress  $\sigma_1$ ; (e) mean stress  $p$

Based on the above analysis, we can conclude that  $q_{CN}$ ,  $q_{oct}$  and  $\sigma_{Fm}$  criteria are suitable to describe the particle breakage. During compression, the number of small particles increases progressively due to the continuous breakage of large particles. When the number of small particle reaches a certain value, the surviving large particles will have a high value of  $CN$  since they are surrounded by many small particles. The high  $CN$  can create a hydrostatic effect on the large particles, which results in a limited increase of deviatoric stress  $q$  (or  $\sigma_{Fm}$ ) and a continuous increase of mean stress  $p$ . Note that in  $q_{CN}$  criterion, the strength of large particles will also be enhanced due to the continuous increasing  $p$ ,



which makes them even more difficult to break. This observation can be used to explain why the large particles can survive under high vertical stress even though they have a lower strength than small particles.

The obtained results emphasize the influence of  $CN$  on the mechanical behavior of crushable rockfill materials. The high  $CN$  in large particles lead to a remarkable hydrostatic effect and improve the survival probability of large particles. It should be noticed that the conclusions above are drawn based on the oedometer tests. Different from the oedometer tests, the large particles may suffer a relatively high deviatoric stress in triaxial tests, especially in the shear bands. In practice, laboratory tests (Coop and Lee, 1992) and DEM simulations (Hanley et al., 2015) show that more particle breakage takes place in the triaxial compression tests. The advantage of the proposed  $q_{CN}$  criterion, in which the improvement of particle strength related to the increase of  $CN$  is taken into account, will be more obvious in the simulations of triaxial compression tests.

## 6 Conclusions

The effect of coordination number  $CN$  on particle strength is studied via a series of simulations of oedometer tests. A new breakage criterion considering  $CN$  effect is proposed and implemented in YADE. The proposed breakage criterion is validated by the good agreement obtained between the numerical simulations and experimental data. The main conclusions are summarized as follows:

(1) The preliminary results of multi-particle crushing tests show that the failure pattern and particle strength are significantly affected by  $CN$ . For  $CN \leq 4$ , the particle breakage is controlled by the strong force chains connecting each contact points, and agglomerates are split into 2 or 3 main pieces. Comparatively, when  $CN > 4$ , the forces chains are homogeneously distributed inside the agglomerates, and they are split into more small pieces. Five commonly-used stress indexes in breakage criteria (octahedral shear stress  $q_{oct}$ , stress induced by the maximum normal contact force  $\sigma_{Fm}$ , major principal stress  $\sigma_1$  and mean stress  $p$ ) are studied, and all of them increase with the increase of  $CN$ .

(2) Although  $CN$  has an important impact on the particle strength, it is not suitable to directly introduce  $CN$  in the breakage criterion due to the existence of strong and weak force chains. Mean stress  $p$  is chosen as a replacement of  $CN$ , and a new breakage criterion, called  $q_{CN}$  criterion, is then proposed. The parameters in this criterion can be determined by using the single-particle crushing tests and the characteristics of parent rock.

(3) By using the proposed breakage criterion  $q_{CN}$ , the oedometer tests with three different particle sizes are simulated. A good concordance is obtained between the numerical simulations and the experimental data. The proposed breakage criterion is capable of describing satisfactorily the macro-mechanical behavior of studied rockfill materials. A fractal number of 2.7 emerges in the particle size distribution (PSD). The size effects of rockfill materials can also be captured by the numerical simulation. The obtained results confirm that particle breakage is the main origin of size effect on rockfill materials.

(4) During compression, with the continuous particle breakage, the  $CN$  of large particles increases dramatically since they are surrounded by lots of small particles. The high value of  $CN$  enhances the hydrostatic effect on large particles, by a limited increase of deviatoric stress and a continuous increase of mean stress. As a result, the large particles are more difficultly broken under high applied stress even though they have lower strength than small particles.

The proposed breakage criterion  $q_{CN}$  has been validated by the simulations of the oedometer tests. The proposed criterion has taken into account the hydrostatic effect on the improvement of particle strength, which is not well considered in  $q_{oct}$  and  $\sigma_{Fm}$  criteria. The difference between  $q_{CN}$  and other criteria in triaxial tests should be more important because large particles may be subjected to a high deviatoric stress, especially in shear bands. Triaxial test simulations will be done by using  $q_{CN}$  criterion for a further validation soon.



## Chapter VI

# Conclusions and perspectives

### 1 Conclusions

The main objective of this thesis is to study the particle crushing and mechanical behavior of rockfill materials via a series of laboratory tests and numerical simulations. A special attention is put on the particle breakage of rockfill materials. In the experimental parts, the strength of individual Shuangjiangkou rockfill particles is studied by using single-particle crushing tests. Moreover, dry density tests and triaxial tests are performed on rockfill materials with different maximum particle sizes. In the numerical parts, single-particle crushing tests and oedometer tests are simulated by using discrete element method (DEM) models. The main conclusions are summarized below:

- Single-particle crushing test results show that the strength of rockfill particles decreases with increasing particle size. The distribution of particle strength follows the Weibull distribution with the Weibull modulus of 3.29. Dry density test results indicate that both the maximum and minimum dry densities of rockfill materials increase with increasing maximum particle size.
- Triaxial test results show that the stress-strain relation curves are significantly affected by the maximum particle size  $d_M$ . Both the mobilized internal friction angle at peak and the secant Young's modulus increase with the increase of  $d_M$ . The samples in triaxial tests present a fractal behavior in the particle size distribution (PSD) and the fractal dimension of 2.7 can be used as the ultimate fractal dimension. Both the fractal dimension and relative breakage index increase with the increase of  $d_M$ .
- A bonded particle model (BPM) is established in YADE (an open-source DEM software) to simulate the single-particle crushing tests. Model parameters are calibrated

against the physical test curves. Simulation results indicate that the flaw volume ratio is the key issue of particle size effects. For a given flaw volume ratio, the particle strength is independent of its size when the ratio of elementary ball size to agglomerate size is sufficiently small.

- A breakage criterion considering the effect of coordination number is proposed for DEM simulation and implemented in YADE. The proposed model is firstly verified by a series of oedometer test simulations. A good agreement between the numerical simulation and experimental data show that the PBM model can qualitatively reproduce the particle size effects on rockfill materials. The particle size distribution (PSD) emerges fractal behavior under vertical stress.

## 2 Perspectives

The present research work pushes forward the study of crushing and particle size effect on rockfill materials. However, some work is still preliminary. Further studies may be beneficial as follows:

- The present study only focuses on one kind of rockfill materials with angular/subangular particles obtained from crushing parent rock. In fact, there is another group of rockfill materials with rounded/subrounded particles collected from river bed (Varadarajan et al., 2006, 2003; Honkanadavar and Sharma, 2016). As a result, several other kinds of rockfill materials should be used for laboratory tests to further confirm the conclusions drawn in this thesis.
- In the single-particle crushing studies, DEM simulation results indicate that the flaw volume ratio is the key factor of particle strength. This conclusion may be further confirmed by using the X-ray micro-tomography method on single-particle crushing tests (Zhao et al., 2015) or oedometer tests (Cil and Alshibli, 2012, 2014b).
- In the present bonded particle model, only spherical agglomerates are used, which are different from the physical particles with irregular shapes. The particles with a realistic shape could be reconstructed in DEM by collecting morphologies of particles with 3D laser scanning and image processing (Fu et al., 2017; Huang et al., 2020).
- The established population balance model is only used for simulation of oedometer tests. Simulations on triaxial test could be done (Zhou et al., 2016), and a comparison with physical test results can lead to a thorough understanding of particle size effect on the mechanical behavior of rockfill materials.

- 
- Some irregular particles could also be used in the population balance model, such as polyhedral particles ([Eliás, 2014](#)). Then the effect of particle shape can be considered in the DEM study of crushable granular materials.



# Bibliography

- Agnolin, I. and Roux, J.-N. (2007). Internal states of model isotropic granular packings. i. assembling process, geometry, and contact networks. *Physical Review E*, 76(6):061302.
- Aharonov, D. and Stephenson, K. (1998). Geometric sequences of discs in the apollonian packing. *St Petersburg Mathematical Journal C/C Of Algebra I Analiz*, 9:509–542.
- Alonso, E., Tapias, M., and Gili, J. (2012). Scale effects in rockfill behaviour. *Géotechnique Letters*, 2(3):155–160.
- Altuhafi, F. and Coop, M. R. (2011). Changes to particle characteristics associated with the compression of sands. *Géotechnique*, 61(6):459–471.
- Antony, S. J., Imafidon, O., and Barakat, T. (2015). Micromechanical analysis of inclusions in particulate media using digital photo stress analysis tomography. *Optical Engineering*, 54(8):081202.
- ASTM, I. (2011). Standard test method for direct shear test of soils under consolidated drained conditions (withdrawn 2020). *D 3080/D3080M-11*.
- ASTM, I. (2016a). Standard test methods for maximum index density and unit weight of soils using a vibratory table. *ASTM D 4253-16e1*.
- ASTM, I. (2016b). Standard test methods for minimum index density and unit weight of soils and calculation of relative density. *ASTM D 4254-16*.
- ASTM, I. (2020a). Standard test method for consolidated drained triaxial compression test for soils. annual book of astm standards. *ASTM D 7181-20*.
- ASTM, I. (2020b). Standard test methods for determination of maximum dry unit weight of granular soils using a vibrating hammer. *ASTM D 7382-20*.
- Aström, J. A. and Herrmann, H. J. (1998). Fragmentation of grains in a two-dimensional packing. *The European Physical Journal B-Condensed Matter and Complex Systems*, 5(3):551–554.
- Baladi, G. Y. and Wu, T. T. (1988). Interpretation of triaxial test results of cohesionless soils: A new model. In *Advanced Triaxial Testing of Soil and Rock*. ASTM International.



- Barreto, D. and O'Sullivan, C. (2012). The influence of inter-particle friction and the intermediate stress ratio on soil response under generalised stress conditions. *Granular Matter*, 14(4):505–521.
- Behringer, R., Howell, D., Kondic, L., Tennakoon, S., and Veje, C. (1999). Predictability and granular materials. *Physica D: Nonlinear Phenomena*, 133(1-4):1–17.
- Belheine, N., Plassiard, J.-P., Donzé, F.-V., Darve, F., and Seridi, A. (2009). Numerical simulation of drained triaxial test using 3d discrete element modeling. *Computers and Geotechnics*, 36(1-2):320–331.
- Ben-Nun, O. and Einav, I. (2008). A refined dem study of grain size reduction in uniaxial compression. In *Proceedings of the 12th international conference of the international association for computer methods and advances in geomechanics (IACMAG), Goa, India*, pages 702–708.
- Ben-Nun, O. and Einav, I. (2010). The role of self-organization during confined comminution of granular materials. *Philosophical Transactions of the Royal Society A: Mathematical, Physical and Engineering Sciences*, 368(1910):231–247.
- Berger, K. J. and Hrenya, C. M. (2014). Challenges of dem: Ii. wide particle size distributions. *Powder Technology*, 264:627–633.
- Billam, J. (1972). Some aspects of the behaviour of granular materials at high pressures. In *Proc. of the Roscoe Memorial Symp., Cambridge*, pages 69–80.
- Bishop, A. W. (1948). A large shear box for testing sands and gravels. In *Proceedings of the 2nd international conference on soil mechanics and foundation engineering, Rotterdam, The Netherlands*, pages 21–30.
- Bishop, A. W. and Green, G. E. (1965). The influence of end restraint on the compression strength of a cohesionless soil. *Géotechnique*, 15(3):243–266.
- Borkovec, M., De Paris, W., and Peikert, R. (1994). The fractal dimension of the apollonian sphere packing. *Fractals*, 2(04):521–526.
- Boutt, D. and McPherson, B. (2002). The role of particle packing in modeling rock mechanical behavior using discrete elements. In *Discrete Element Methods: Numerical Modeling of Discontinua*, pages 86–92.

- Brzesowsky, R., Spiers, C., Peach, C., and Hangx, S. (2011). Failure behavior of single sand grains: theory versus experiment. *Journal of Geophysical Research: Solid Earth*, 116(B6).
- Buckingham, E. (1914). On physically similar systems; illustrations of the use of dimensional equations. *Physical Review*, 4(4):345.
- Casagrande, A. (1936). Characteristics of cohesionless soils affecting the stability of slopes and earth fills. *J. Boston Society of Civil Engineers*, 23(1):13–32.
- Cerato, A. B. and Lutenecker, A. J. (2006). Specimen size and scale effects of direct shear box tests of sands. *Geotechnical Testing Journal*, 29(6):507–516.
- Charles, J. (2008). The engineering behaviour of fill materials: the use, misuse and disuse of case histories. *Géotechnique*, 58(7):541–570.
- Charles, J. and Watts, K. (1980). The influence of confining pressure on the shear strength of compacted rockfill. *Géotechnique*, 30(4):353–367.
- Charles, J. A. (1973). Correlation between laboratory behaviour of rockfill and field performance with particular reference to scammonden dam.
- Cheng, Y. and Minh, N. (2009). Dem investigation of particle size distribution effect on direct shear behaviour of granular agglomerates. In *AIP Conference Proceedings*, volume 1145, pages 401–404. American Institute of Physics.
- Cheshomi, A. and Sheshde, E. A. (2013). Determination of uniaxial compressive strength of microcrystalline limestone using single particles load test. *Journal of Petroleum Science and Engineering*, 111:121–126.
- Cheung, G. and O’Sullivan, C. (2008). Effective simulation of flexible lateral boundaries in two-and three-dimensional dem simulations. *Particuology*, 6(6):483–500.
- Cho, N. a., Martin, C., and Sego, D. (2007). A clumped particle model for rock. *International Journal of Rock Mechanics and Mining Sciences*, 44(7):997–1010.
- Ciantia, M. O., Arroyo, M., Calvetti, F., and Gens, A. (2015). An approach to enhance efficiency of dem modelling of soils with crushable grains. *Géotechnique*, 65(2):91–110.
- Ciantia, M. O., Arroyo, M., Gens, A., and Calvetti, F. (2014). Particle failure in DEM models of crushable soil response. In Hicks, M. A., Brinkgreve, R. B. J., and Rohe,

- A., editors, *Numerical Methods in Geotechnical Engineering*, volume 1, pages 345–350. CRC Press/Balkema, Leiden, the Netherlands.
- Cil, M. and Alshibli, K. (2012). 3d assessment of fracture of sand particles using discrete element method. *Géotechnique Letters*, 2(3):161–166.
- Cil, M. and Alshibli, K. (2014a). 3d evolution of sand fracture under 1d compression. *Géotechnique*, 64(5):351–364.
- Cil, M. B. and Alshibli, K. A. (2014b). 3D evolution of sand fracture under 1D compression. *Géotechnique*, 64(5):351–364.
- Cil, M. B. and Alshibli, K. A. (2015). Modeling the influence of particle morphology on the fracture behavior of silica sand using a 3d discrete element method. *CR Mécanique.*, 343(2):133–142.
- Cleary, P. W., Prakash, M., Sinnott, M. D., Rudman, M., and Das, R. (2011). Large scale simulation of industrial, engineering and geophysical flows using particle methods. In *Particle-Based Methods*, volume 25 of *Computational Methods in Applied Sciences*, pages 89–111. Springer Netherlands, Dordrecht.
- Coop, M., Sorensen, K., Freitas, T. B., and Georgoutsos, G. (2004). Particle breakage during shearing of a carbonate sand. *Géotechnique*, 54(3):157–163.
- Coop, M. R. and Lee, I. (1992). The behaviour of granular soils at elevated stresses. In *Predictive soil mechanics: Proceedings of the Wroth Memorial Symposium held at St Catherine's College, Oxford, 27-29 July 1992*, pages 186–198. Thomas Telford Publishing.
- Corriveau, D., Savage, S., and Oger, L. (1997). Internal friction angles: characterization using biaxial test simulations. In *IUTAM Symposium on Mechanics of Granular and Porous materials*, pages 313–324. Springer, Springer Netherlands.
- Couroyer, C., Ning, Z., and Ghadiri, M. (2000). Distinct element analysis of bulk crushing: effect of particle properties and loading rate. *Powder Technology*, 109(1-3):241–254.
- CS, C. S. (1999). “standard test methods for soils.”. *SL237-1999*.
- CS, C. S. (2006). “code for coarse-grained soil tests for hydropower and water conservancy engineering.”. *DL/T 5356-2006*.

- Cundall, P. (1988). Computer simulations of dense sphere assemblies. In *Studies in Applied Mechanics*, volume 20, pages 113–123. Elsevier.
- Cundall, P. A. (1971). A computer model for simulating progressive, large-scale movement in blocky rock system. In *Proceedings of the International Symposium on Rock Mechanics, 1971*.
- Cundall, P. A. (2001). A discontinuous future for numerical modelling in geomechanics? *Proceedings of the institution of civil engineers-geotechnical engineering*, 149(1):41–47.
- Cundall, P. A. and Strack, O. D. (1979). A discrete numerical model for granular assemblies. *Géotechnique*, 29(1):47–65.
- Daouadji, A. and Hicher, P.-Y. (2010). An enhanced constitutive model for crushable granular materials. *International Journal for Numerical and Analytical Methods in Geomechanics*, 34(6):555–580.
- Daouadji, A., Hicher, P.-Y., and Rahma, A. (2001). An elastoplastic model for granular materials taking into account grain breakage. *European Journal of Mechanics-A/Solids*, 20(1):113–137.
- Darvell, B. (1990). Uniaxial compression tests and the validity of indirect tensile strength. *Journal of Materials Science*, 25(2):757–780.
- das Neves, E. M. (1991). *Advances in rockfill structures*, volume 89. London: Kluwer Academic Publishers.
- de Bono, J. and McDowell, G. (2016a). Particle breakage criteria in discrete-element modelling. *Géotechnique*, 66(12):1014–1027.
- de Bono, J. P. (2013). *Discrete element modeling of cemented sand and particle crushing at high pressures*. PhD thesis, University of Nottingham, UK.
- de Bono, J. P. and McDowell, G. R. (2014). Dem of triaxial tests on crushable sand. *Granular Matter*, 16(4):551–562.
- de Bono, J. P. and McDowell, G. R. (2015). An insight into the yielding and normal compression of sand with irregularly-shaped particles using dem. *Powder Technology*, 271:270–277.
- de Bono, J. P. and McDowell, G. R. (2016b). The fractal micro mechanics of normal compression. *Computers and Geotechnics*, 78:11–24.

- de Bono, J. P., McDowell, G. R., and Wanatowski, D. (2014). Dem of triaxial tests on crushable cemented sand. *Granular Matter*, 16(4):563–572.
- Deluzarche, R. and Cambou, B. (2006). Discrete numerical modelling of rockfill dams. *International Journal for Numerical and Analytical Methods in Geomechanics*, 30(11):1075–1096.
- Donaghe, R. T. and Torrey III, V. H. (1985). Strength and deformation properties of earth-rock mixtures. Technical report, ARMY ENGINEER WATERWAYS EXPERIMENT STATION VICKSBURG MS GEOTECHNICAL LAB.
- Drescher, A. and De Jong, G. D. J. (1972). Photoelastic verification of a mechanical model for the flow of a granular material. *Journal of the Mechanics and Physics of Solids*, 20(5):337–340.
- Drlik, G. J. (1987). *Simulation of the crushing of a two-dimensional particle bed due to compressive loading*. PhD thesis, Massachusetts Institute of Technology, USA.
- Drnevich, V., Evans, A. C., and Prochaska, A. (2007). A study of effective soil compaction control of granular soils. *Joint Transportation Research Program*, page 234.
- Duran, J. (2000). *Sands, powders, and grains: an introduction to the physics of granular materials*. Springer Science & Business Media.
- Duriez, J., Scholtès, L., and Donzé, F.-V. (2016). Micromechanics of wing crack propagation for different flaw properties. *Engineering Fracture Mechanics*, 153:378–398.
- Einav, I. (2007). Breakage mechanics—part i: theory. *Journal of the Mechanics and Physics of Solids*, 55(6):1274–1297.
- Elghezal, L., Jamei, M., and Georgopoulos, I. O. (2013). DEM simulations of stiff and soft materials with crushable particles: an application of expanded perlite as a soft granular material. *Granular Matter*, 15(5):685–704.
- Eliás, J. (2014). Simulation of railway ballast using crushable polyhedral particles. *Powder Technology*, 264:458–465.
- EM, T. (1988). Evaluation of vibratory table displacement-acceleration behavior. report no. gr-88-5. Technical report, U. S. Department of the Interior, Bureau of Reclamation.
- Ergenzinger, C., Seifried, R., and Eberhard, P. (2012). A discrete element model predicting the strength of ballast stones. *Computers and Structures*, 108:3–13.

- Esnault, V. P. B. and Roux, J. N. (2013). 3D numerical simulation study of quasistatic grinding process on a model granular material. *Mechanics of Materials*, 66:88–109.
- Evans, T. M., Mojarad, H., Cunningham, C., and Tayebali, A. A. (2009). Grain size distribution effects in 2d discrete numerical experiments. In *Contemporary Topics in In Situ Testing, Analysis, and Reliability of Foundations*, pages 58–65.
- Fakhimi, A., Hosseinpour, H., et al. (2008). The role of oversize particles on the shear strength and deformational behavior of rock pile material. In *The 42nd US Rock Mechanics Symposium (USRMS)*. American Rock Mechanics Association.
- Feng, G. and Vitton, S. (1999). Laboratory determination of compaction criteria for rockfill material embankments. In *International Conference on Soil Mechanics and Foundation Engineering*, pages 485–488.
- Fonseca, J., O’SULLIVAN, C., Coop, M. R., and Lee, P. (2013). Quantifying the evolution of soil fabric during shearing using directional parameters. *Géotechnique*, 63(6):487–499.
- Forssblad, L. (1981). Vibratory soil and rock fill compaction. Technical report.
- Fox, Z. P. (2011). Critical state, dilatancy and particle breakage of mine waste rock. *2000-2019-CSU Theses and Dissertations*.
- Frossard, E., Hu, W., Dano, C., and Hicher, P.-Y. (2012). Rockfill shear strength evaluation: a rational method based on size effects. *Géotechnique*, 62(5):415–427.
- Frost, R. (1973). Some testing experiences and characteristics of boulder-gravel fill in earth dams. In *Evaluation of Relative Density and its Role in Geotechnical Projects Involving Cohesionless Soils*. ASTM International.
- Fu, G. and Dekelbab, W. (2003). 3-d random packing of polydisperse particles and concrete aggregate grading. *Powder Technology*, 133(1-3):147–155.
- Fu, R., Hu, X., and Zhou, B. (2017). Discrete element modeling of crushable sands considering realistic particle shape effect. *Computers and Geotechnics*, 91:179–191.
- Fukumoto, T. and Hara, T. (1998). A study on the granule strength distribution of granular soil. *Doboku Gakkai Ronbunshu*, 1998(596):91–99.
- Fukushima, S. and Kitajima, A. (1998). History and contribution of super large scale triaxial compression testing apparatus. *Soil Mechanics and Foundation Engineering*, 46(11):29–32.

- Fumagalli, E. (1969). Tests on cohesionless materials for rockfill dams. *Journal of Soil Mechanics and Foundations Division*, 92(SM5, Proc Paper 490).
- Fumagalli, E. (1970). Laboratory tests on materials and static models for rockfill dams. In *10th Int. Congress on Large Dams*, pages 531–551.
- Geng, J., Reydellet, G., Clément, E., and Behringer, R. (2003). Green's function measurements of force transmission in 2d granular materials. *Physica D: Nonlinear Phenomena*, 182(3-4):274–303.
- Griffith, A. A. (1920). Vi. the phenomena of rupture and flow in solids. *Philosophical Transactions of the Royal Society of London. Series A, Containing Papers of A Mathematical or Physical Character*, 221(582-593):163–198.
- Guida, G., Casini, F., Viggiani, G. M., Ando, E., and Viggiani, G. (2018). Breakage mechanisms of highly porous particles in 1D compression revealed by X-ray tomography. *Géotechnique Letters*, 8(2):155–160.
- Gupta, A. K. (2016). Effects of particle size and confining pressure on breakage factor of rockfill materials using medium triaxial test. *Journal of Rock Mechanics and Geotechnical Engineering*, 8(3):378–388.
- Hagerty, M., Hite, D., Ullrich, C., and Hagerty, D. (1993). One-dimensional high-pressure compression of granular media. *Journal of Geotechnical Engineering*, 119(1):1–18.
- Ham, T.-G., Nakata, Y., Orense, R. P., and Hyodo, M. (2010). Influence of gravel on the compression characteristics of decomposed granite soil. *Journal of Geotechnical and Geoenvironmental Engineering*, 136(11):1574–1577.
- Hanley, K. J., O'Sullivan, C., and Huang, X. (2015). Particle-scale mechanics of sand crushing in compression and shearing using DEM. *Soils and Foundations*, 55(5):1100–1112.
- Hanley, K. J., O'Sullivan, C., Oliveira, J. C., Cronin, K., and Byrne, E. P. (2011). Application of taguchi methods to dem calibration of bonded agglomerates. *Powder Technology*, 210(3):230–240.
- Hardin, B. O. (1985). Crushing of soil particles. *Journal of Geotechnical Engineering*, 111(10):1177–1192.

- Hasan, A. and Alshibli, K. (2010). Experimental assessment of 3d particle-to-particle interaction within sheared sand using synchrotron microtomography. *Géotechnique*, 60(5):369–379.
- Head, K. H. et al. (2006). *Manual of soil laboratory testing. Volume 1: Soil classification and compaction tests*. Number Ed. 3. CRC Press Ltd.
- Head, K. H. et al. (2011). *Manual of soil laboratory testing. Volume 2: Permeability, shear strength and compressibility tests*. Number Ed. 3. CRC Press Ltd.
- Holtz, R. D., Kovacs, W. D., and Sheahan, T. C. (1981). *An introduction to geotechnical engineering*, volume 733. Prentice-Hall Englewood Cliffs, NJ.
- Holtz, W. and Lowitz, C. (1958). “compaction characteristics of gravelly soils”. In *Conference on Soils for Engineering Purposes: ASTM Special Technical Publication*, pages 67–101.
- Holtz, W. G. and Gibbs, H. J. (1956). Triaxial shear tests on pervious gravelly soils. *Journal of the Soil Mechanics and Foundations Division*, 82(1):1–22.
- Honkanadavar, N. and Sharma, K. (2014). Testing and modeling the behavior of riverbed and blasted quarried rockfill materials. *International Journal of Geomechanics*, 14(6):04014028.
- Honkanadavar, N. and Sharma, K. (2016). Modeling the triaxial behavior of riverbed and blasted quarried rockfill materials using hardening soil model. *Journal of Rock Mechanics and Geotechnical Engineering*, 8(3):350–365.
- Hsu, T.-S. and Saxena, S. K. (1991). A general formula for determining density of compacted soils with oversize particles. *Soils and Foundations*, 31(3):91–96.
- Hu, W., Dano, C., Hicher, P.-Y., Le Touzo, J.-Y., Derkx, F., and Merliot, E. (2011). Effect of sample size on the behavior of granular materials. *Geotechnical Testing Journal*, 34(3):186–197.
- Huang, H. (1999). *Discrete element modeling of tool-rock interaction*. University of Minnesota, USA.
- Huang, J., Xu, S., Yi, H., and Hu, S. (2014). Size effect on the compression breakage strengths of glass particles. *Powder Technology*, 268:86–94.



- Huang, Q., Zhou, W., Ma, G., Ng, T.-T., and Xu, K. (2020). Experimental and numerical investigation of the behavior of grain crushing strength. *Geoscience Frontiers*, 11(2):401–411.
- Hurley, R., Hall, S., Andrade, J., and Wright, J. (2016). Quantifying interparticle forces and heterogeneity in 3d granular materials. *Physical Review Letters*, 117(9):098005.
- Indraratna, B., Wijewardena, L., and Balasubramaniam, A. (1993). Large-scale triaxial testing of grey wacke rockfill. *Géotechnique*, 43(1):37–51.
- Institution, B. S. (1990). *British Standard Methods of Test for Soils for Civil Engineering Purposes: Part 7: Shear strength tests (total stress) tests*. British Standards Institution.
- Irwin, G. R. (1957). Analysis of stresses and strains near the end of a crack transversing a plate. *International Journal Of Applied Mechanics*, 24:361–364.
- Itasca, C. (2007). 3dec version 4.1 user’s guide. *Minneapolis, Minnesota USA*.
- Itasca, P. (2015). 5.0 documentation. *Itasca Inc, Minneapolis, MN, USA*.
- Iwashita, K. and Oda, M. (1998). Rolling resistance at contacts in simulation of shear band development by dem. *Journal of Engineering Mechanics*, 124(3):285–292.
- Iwashita, K. and Oda, M. (2000). Micro-deformation mechanism of shear banding process based on modified distinct element method. *Powder Technology*, 109(1-3):192–205.
- Jaeger, J. (1967). Failure of rocks under tensile conditions. In *International Journal of Rock Mechanics and Mining Sciences & Geomechanics Abstracts*, volume 4, pages 219–227. Elsevier.
- Jansen, U. and Stoyan, D. (2000). On the validity of the weibull failure model for brittle particles. *Granular Matter*, 2(4):165–170.
- Jewell, R. and Wroth, C. (1987). Direct shear tests on reinforced sand. *Géotechnique*, 37(1):53–68.
- Jiang, M., Leroueil, S., Zhu, H., Yu, H.-S., and Konrad, J.-M. (2009). Two-dimensional discrete element theory for rough particles. *International Journal of Geomechanics*, 9(1):20–33.
- Jiang, M., Yu, H.-S., and Harris, D. (2005). A novel discrete model for granular material incorporating rolling resistance. *Computers and Geotechnics*, 32(5):340–357.

- Kalman, H. and Goder, D. (1998). Design criteria for particle attrition. *Advanced Powder Technology*, 9(2):153–167.
- Kh, A. B. and Mirghasemi, A. (2009). Numerical and experimental direct shear tests for coarse-grained soils. *Particuology*, 7(1):83–91.
- Kh, A. B., Mirghasemi, A., and Mohammadi, S. (2011). Numerical simulation of particle breakage of angular particles using combined dem and fem. *Powder Technology*, 205(1-3):15–29.
- Kim, C. S. (2007). *Evaluating shear mobilization in rockfill columns used for riverbank stabilization*. PhD thesis, University of Manitoba, Canada.
- Kloss, C. and Goniva, C. (2011). Liggghts—open source discrete element simulations of granular materials based on lammmps. *Supplemental Proceedings: Materials Fabrication, Properties, Characterization, and Modeling*, 2:781–788.
- Kloss, C., Goniva, C., Hager, A., Amberger, S., and Pirker, S. (2012). Models, algorithms and validation for opensource dem and cfd-dem. *Progress in Computational Fluid Dynamics, an International Journal*, 12(2-3):140–152.
- Kong, C. M. and Lannutti, J. J. (2000). Effect of agglomerate size distribution on loose packing fraction. *Journal of the American Ceramic Society*, 83(9):2183–2188.
- Kong, X., Ning, F., and Liu, J. (2019). Scale effect of rockfill materials using super-large triaxial tests. *Chinese Journal of Geotechnical Engineering*, 41(2):255–261.
- Kozicki, J. and Donze, F. V. (2008). A new open-source software developed for numerical simulations using discrete modeling methods. *Computer Methods in Applied Mechanics and Engineering*, 197(49-50):4429–4443.
- Kozicki, J. and Donze, F. V. (2009). Yade-open dem: An open-source software using a discrete element method to simulate granular material. *Engineering Computations*.
- Kuhn, M. R. (1999). Structured deformation in granular materials. *Mechanics of Materials*, 31(6):407–429.
- Kuhn, M. R. and Bagi, K. (2009). Specimen size effect in discrete element simulations of granular assemblies. *Journal of Engineering Mechanics*, 135(6):485–492.
- Lade, P. V. and Yamamuro, J. A. (1996). Undrained sand behavior in axisymmetric tests at high pressures. *Journal of Geotechnical Engineering*, 122(2):120–129.

- Lade, P. V., Yamamuro, J. A., and Bopp, P. A. (1996). Significance of particle crushing in granular materials. *Journal of Geotechnical Engineering*, 122(4):309–316.
- Latha, G. M. and Sitharam, T. (2008). Effect of particle size and gradation on the behaviour of granular materials simulated using dem. *Indian Geotechnical Journal*, 38(1):89–100.
- Le Pen, L., Powrie, W., Zervos, A., Ahmed, S., and Aingaran, S. (2013). Dependence of shape on particle size for a crushed rock railway ballast. *Granular Matter*, 15(6):849–861.
- Lee, D.-M. (1992). *The angles of friction of granular fills*. PhD thesis, University of Cambridge, UK.
- Lee, K. L. and Farhoomand, I. (1967). Compressibility and crushing of granular soil in anisotropic triaxial compression. *Canadian Geotechnical Journal*, 4(1):68–86.
- Leslie, D. (1963). Large scale triaxial tests on gravelly soils. In *Proc. of the 2nd Pan-American Conf. on SMFE, Brazil*, volume 1, pages 181–202.
- Leslie, D. (1969). Relationships between shear strength, gradation and index properties of rockfill materials. specialty session no. 13. In *7th International Conference on Soil Mechanics and Foundation Engineering, Mexico*, pages 201–210.
- Lewis, J. et al. (1955). Shear strength of rock fill. *New Zealand Engineering*, 10(11):388.
- Li, H. (2013). *Discrete element method (DEM) modelling of rock flow and breakage within a cone crusher*. PhD thesis, University of Nottingham, UK.
- Li, N.-h., Zhu, T., and Zhan-kuan, M. (2001). Strength and deformation properties of transition zone material of xiaolangdi dam and scale effect. *Water Resources and Power*, 19(2):39–42.
- Lim, W. and McDowell, G. (2007). The importance of coordination number in using agglomerates to simulate crushable particles in the discrete element method. *Géotechnique*, 57(8):701–705.
- Lim, W. L. (2004). *Mechanics of railway ballast behaviour*. PhD thesis, University of Nottingham Nottingham, UK.
- Lim, W. L., McDowell, G. R., and Collop, A. C. (2004). The application of weibull statistics to the strength of railway ballast. *Granular Matter*, 6(4):229–237.

- Liu, B.-c., ZHANG, J.-s., Du, Q.-z., et al. (1998). A study of size effect for compression strength of rock. *Chinese Journal of Rock Mechanics and Engineering*, 17(6):611–614.
- Liu, J., Zhou, W., Ma, G., Yang, S., and Chang, X. (2020). Strong contacts, connectivity and fabric anisotropy in granular materials: A 3d perspective. *Powder Technology*.
- Liu, J., Zou, D., Kong, X., and Liu, H. (2016). Stress-dilatancy of zipingpu gravel in triaxial compression tests. *Science China Technological Sciences*, 59(2):214–224.
- Liu, L. and Yuan, Y. (2000). Dynamic simulation of powder compact by random packing of monosized and polydisperse particles. *Journal of Materials Science Letters*, 19(10):841–843.
- Liu, L., Zhang, Z., and Yu, A. (1999). Dynamic simulation of the centripetal packing of mono-sized spheres. *Physica A: Statistical Mechanics and its Applications*, 268(3-4):433–453.
- Liu, S.-h. (2009). Application of in situ direct shear device to shear strength measurement of rockfill materials. *Water Science and Engineering*, 2(3):48–57.
- Liu, Y., Yin, Z., Hicher, P., Wang, J., and Xia, X. (2013). Macro and micro analysis for grading-dependent mechanical behavior of granular materials. In *Poromechanics V: Proceedings of the Fifth Biot Conference on Poromechanics*, pages 1082–1089.
- Lobo-Guerrero, S. and Vallejo, L. (2005a). Crushing a weak granular material: experimental numerical analyses. *Géotechnique*, 55(3):245–249.
- Lobo-Guerrero, S. and Vallejo, L. (2005b). Dem analysis of crushing around driven piles in granular materials. *Géotechnique*, 55(8):617–623.
- Lobo-Guerrero, S. and Vallejo, L. E. (2005c). Discrete element method evaluation of granular crushing under direct shear test conditions. *Journal of Geotechnical and Geoenvironmental Engineering*, 131(10):1295–1300.
- Lobo-Guerrero, S. and Vallejo, L. E. (2006a). Application of weibull statistics to the tensile strength of rock aggregates. *Journal of Geotechnical and Geoenvironmental Engineering*, 132(6):786–790.
- Lobo-Guerrero, S. and Vallejo, L. E. (2006b). Discrete element method analysis of railtrack ballast degradation during cyclic loading. *Granular Matter*, 8(3-4):195.

- Lobo-Guerrero, S., Vallejo, L. E., and Vesga, L. F. (2006). Visualization of crushing evolution in granular materials under compression using DEM. *International Journal Of Geomechanics*, 6(3):195–200.
- Lowe, J. (1964). Shear strength of coarse embankment dam materials. In *Proc., 8th Int. Congress on Large Dams*, volume 3, pages 745–761. International Commission on Large Dams Paris.
- Luding, S. (2008). Introduction to discrete element methods: basic of contact force models and how to perform the micro-macro transition to continuum theory. *European journal of Environmental and Civil Engineering*, 12(7-8):785–826.
- Luzzani, L. and MR, C. (2002). On the relationship between particle breakage and the critical state of sands. *Soils and Foundations*, 42(2):71–82.
- Mahinroosta, R., Alizadeh, A., and Gatmiri, B. (2015). Simulation of collapse settlement of first filling in a high rockfill dam. *Engineering Geology*, 187:32–44.
- Makse, H. A., Johnson, D. L., and Schwartz, L. M. (2000). Packing of compressible granular materials. *Physical Review Letters*, 84(18):4160.
- Maqbool, S. and Koseki, J. (2010). Large-scale triaxial tests to study effects of compaction energy and large cyclic loading history on shear behavior of gravel. *Soils and Foundations*, 50(5):633–644.
- Marachi, N. (1969). *Strength and deformation characteristics of rockfill materials*. PhD thesis, University of California, Berkeley, USA.
- Marachi, N., Seed, H., and Chan, C. (1969). Strength characteristics of rockfill materials. In *Seventh International Conference on Soil Mechanics and Foundation Engineering*, pages 217–224.
- Marachi, N. D., Chan, C. K., and Seed, H. B. (1972). Evaluation of properties of rockfill materials. *Journal of the Soil Mechanics and Foundations Division*, 98(1):95–114.
- Marketos, G. and Bolton, M. (2009). Compaction bands simulated in discrete element models. *Journal of Structural Geology*, 31(5):479–490.
- Marketos, G. and Bolton, M. D. (2010). Flat boundaries and their effect on sand testing. *International Journal for Numerical and Analytical Methods in Geomechanics*, 34(8):821–837.

- Marsal, R. (1969). Mechanical properties of rock-fill and gravel materials. *Special Session, 7th. ICSMFE*, 3:499–506.
- Marsal, R. J. (1967). Large scale testing of rockfill materials. *Journal of the Soil Mechanics and Foundations Division*, 93(2):27–43.
- Mařín, D. (2012). Asymptotic behaviour of granular materials. *Granular Matter*, 14(6):759–774.
- McDowell, G. (2001). Statistics of soil particle strength. *Géotechnique*, 51(10):897–900.
- McDowell, G. (2002). On the yielding and plastic compression of sand. *Soils and Foundations*, 42(1):139–145.
- McDowell, G. and Amon, A. (2000). The application of weibull statistics to the fracture of soil particles. *Soils and Foundations*, 40(5):133–141.
- McDowell, G. and Bolton, M. (1998). On the micromechanics of crushable aggregates. *Géotechnique*, 48(5):667–679.
- McDowell, G., Bolton, M., and Robertson, D. (1996). The fractal crushing of granular materials. *Journal of the Mechanics and Physics of Solids*, 44(12):2079–2102.
- McDowell, G. and Harireche, O. (2002). Discrete element modelling of soil particle fracture. *Géotechnique*, 52(2):131–135.
- McDowell, G. and Humphreys, A. (2002). Yielding of granular materials. *Granular Matter*, 4(1):1–8.
- McDowell, G. R. and de Bono, J. P. (2013). On the micro mechanics of one-dimensional normal compression. *Géotechnique*, 63(11):895–908.
- Mindlin, R. D. (1953). Elastic spheres in contact under varying oblique forces. *Journal of Applied Mechanics*, 20:327–344.
- Miura, N., Sukeo, O., et al. (1979). Particle-crushing of a decomposed granite soil under shear stresses. *Soils and Foundations*, 19(3):1–14.
- Moreno, R., Ghadiri, M., and Antony, S. (2003). Effect of the impact angle on the breakage of agglomerates: a numerical study using dem. *Powder Technology*, 130(1-3):132–137.

- Muthuswamy, M. and Tordesillas, A. (2006). How do interparticle contact friction, packing density and degree of polydispersity affect force propagation in particulate assemblies? *Journal of Statistical Mechanics: Theory and Experiment*, 2006(09):P09003.
- Nakata, A., Hyde, M., Hyodo, H., and Murata (1999). A probabilistic approach to sand particle crushing in the triaxial test. *Géotechnique*, 49(5):567–583.
- Nakata, Y., Hyodo, M., Hyde, A. F., Kato, Y., and Murata, H. (2001a). Microscopic particle crushing of sand subjected to high pressure one-dimensional compression. *Soils and Foundations*, 41(1):69–82.
- Nakata, Y., Kato, Y., Hyodo, M., Hyde, A. F., and Murata, H. (2001b). One-dimensional compression behaviour of uniformly graded sand related to single particle crushing strength. *Soils and Foundations*, 41(2):39–51.
- Ng, T.-T. and Zhou, W. (2016). Sample size effect on dem simulations of binary mixture. In *International Conference on Discrete Element Methods*, pages 73–80. Springer.
- Nguyen, C. L., Inui, T., and Katsumi, T. (2016). Scale effects on the shear strength of waste in coastal landfill sites. *Japanese Geotechnical Society Special Publication*, 2(52):1824–1828.
- Ni, Q., Powrie, W., Zhang, X., and Harkness, R. (2000). Effect of particle properties on soil behavior: 3-d numerical modeling of shearbox tests. In *Numerical Methods in Geotechnical Engineering*, pages 58–70.
- Oda, M. (1977). Co-ordination number and its relation to shear strength of granular material. *Soils and Foundations*, 17(2):29–42.
- Oda, M., Konishi, J., and Nemat-Nasser, S. (1982). Experimental micromechanical evaluation of strength of granular materials: effects of particle rolling. *Mechanics of Materials*, 1(4):269–283.
- Omar, M., Shanableh, A., Basma, A., and Barakat, S. (2003). Compaction characteristics of granular soils in united arab emirates. *Geotechnical & Geological Engineering*, 21(3):283–295.
- Otsubo, M. (2016). *Particle scale analysis of soil stiffness and elastic wave propagation*. PhD thesis, Imperial College London London, UK.

- Ovalle, C., Frossard, E., Dano, C., Hu, W., Maiolino, S., and Hicher, P.-Y. (2014). The effect of size on the strength of coarse rock aggregates and large rockfill samples through experimental data. *Acta Mechanica*, 225(8):2199–2216.
- Oyanguren, P. R., Nicieza, C. G., Fernández, M. Á., and Palacio, C. G. (2008). Stability analysis of Ilerin rockfill dam: An in situ direct shear test. *Engineering Geology*, 100(3-4):120–130.
- O’Sullivan, C. (2011). Particle-based discrete element modeling: geomechanics perspective. *International Journal of Geomechanics*, 11(6):449–464.
- Park, J. and Santamarina, J. C. (2017). Revised soil classification system for coarse-fine mixtures. *Journal of Geotechnical and Geoenvironmental Engineering*, 143(8):04017039.
- Parsons, A. W. et al. (1992). *Compaction of soils and granular materials: a review of research performed at the Transport Research Laboratory*. HMSO.
- Peters, J., Muthuswamy, M., Wibowo, J., and Tordesillas, A. (2005). Characterization of force chains in granular material. *Physical Review E*, 72(4):041307.
- Pike, D. (1972). *Compactability of Graded Aggregates: 1. Standard Laboratory Tests*. Transport and Road Research Laboratory.
- Portnikov, D., Kalman, H., Aman, S., and Tomas, J. (2013). Investigating the testing procedure limits for measuring particle strength distribution. *Powder Technology*, 237:489–496.
- Potyondy, D. O. and Cundall, P. (2004). A bonded-particle model for rock. *International Journal of Rock Mechanics and Mining Sciences*, 41(8):1329–1364.
- Prochaska, A. B. and Drnevich, V. P. (2005). One-point vibrating hammer compaction test for granular soils. In *Advances in Pavement Engineering*, pages 1–15.
- Radjai, F., Jean, M., Moreau, J.-J., and Roux, S. (1996). Force distributions in dense two-dimensional granular systems. *Physical Review Letters*, 77(2):274.
- Radjai, F., Wolf, D. E., Jean, M., and Moreau, J.-J. (1998). Bimodal character of stress transmission in granular packings. *Physical Review Letters*, 80(1):61.
- Rathee, R. and RK, R. (1981). Shear strength of granular soils and its prediction by modelling techniques.



- Refahi, A., Rezai, B., and Mohandesi, J. A. (2007). Use of rock mechanical properties to predict the bond crushing index. *Minerals Engineering*, 20(7):662–669.
- Rodriguez, J., Johansson, J., and Edeskär, T. (2012). Particle shape determination by two-dimensional image analysis in geotechnical engineering. In *Nordic Geotechnical Meeting: 09/05/2012-12/05/2012*, pages 207–218. Danish Geotechnical Society.
- Roscoe, K. H., Schofield, A., and Thurairajah, A. (1963). Yielding of clays in states wetter than critical. *Géotechnique*, 13(3):211–240.
- Rothenburg, L. and Kruyt, N. P. (2004). Critical state and evolution of coordination number in simulated granular materials. *International Journal of Solids and Structures*, 41(21):5763–5774.
- Rozenblat, Y., Portnikov, D., Levy, A., Kalman, H., Aman, S., and Tomas, J. (2011). Strength distribution of particles under compression. *Powder Technology*, 208(1):215–224.
- Sakaguchi, H. and Murakami, A. (2002). Initial packing in discrete element modeling. In *Discrete Element Methods: Numerical Modeling of Discontinua*, pages 104–106.
- Salami, Y., Dano, C., and Hicher, P.-Y. (2019). An experimental study on the influence of the coordination number on grain crushing. *European Journal of Environmental and Civil Engineering*, 23(3):432–448.
- Salimi, N., Yazdanjou, V., and Hamidi, A. (2008). Shape and size effects of gravel grains on the shear behavior of sandy soils. In *Proceedings of the 10th International Symposium on Landslides and Engineered Slopes*, pages 469–474.
- Santamarina, J. and Cascante, G. (1996). Stress anisotropy and wave propagation: a micromechanical view. *Canadian Geotechnical Journal*, 33(5):770–782.
- Scholtès, L. and Donzé, F.-V. (2013). A dem model for soft and hard rocks: role of grain interlocking on strength. *Journal of the Mechanics and Physics of Solids*, 61(2):352–369.
- Selig, E. T. and Roner, C. J. (1987). Effects of particle characteristics on behavior of granular material. *Transportation Research Record*, (1131).
- Shao, L., Chi, S., and Jia, Y. (2009). Meso-mechanical simulation of a large scale triaxial test of rockfill materials. *Rock and Soil Mechanics*, 30(s1):239–243.

- Shao, X.-q., Chi, S.-c., Tao, Y., and Zhou, X.-x. (2020). Dem simulation of the size effect on the wetting deformation of rockfill materials based on single-particle crushing tests. *Computers and Geotechnics*, 123:103429.
- Sharma, V., Venkatachalam, K., and ROYAM, A. (1994). Strength and deformation characteristics of rockfill materials. In *International Conference on Soil Mechanics and Foundation Engineering*, pages 959–962.
- Shipway, P. and Hutchings, I. (1993). Fracture of brittle spheres under compression and impact loading. i. elastic stress distributions. *Philosophical Magazine A*, 67(6):1389–1404.
- Singh, D. (2017). *An investigation into the use of the discrete element method for modelling particle breakage*. PhD thesis, Glasgow Caledonian University, UK.
- Sitharam, T. and Nimbkar, M. (2000). Micromechanical modelling of granular materials: effect of particle size and gradation. *Geotechnical & Geological Engineering*, 18(2):91–117.
- Sitharam, T. G. (2003). Discrete element modelling of cyclic behaviour of granular materials. *Geotechnical & Geological Engineering*, 21(4):297–329.
- Sitharam, T. G., Dinesh, S., and Shimizu, N. (2002). Micromechanical modelling of monotonic drained and undrained shear behaviour of granular media using three-dimensional dem. *International Journal for Numerical and Analytical Methods in Geomechanics*, 26(12):1167–1189.
- Smilauer, V., Catalano, E., Chareyre, B., Dorofeenko, S., Duriez, J., Gladky, A., Kozicki, J., Modenese, C., Scholtès, L., Sibille, L., et al. (2020). Yade documentation 2nd ed.
- Solutions, D. (2010). Edem 2.3 user guide. *Edinburgh, Scotland, UK*.
- Stoeber, J. N. (2012). *Effects of maximum particle size and sample scaling on the mechanical behavior of mine waste rock; a critical state approach*. PhD thesis, Colorado State University. Libraries.
- Subero-Couroyer, C., Ghadiri, M., Brunard, N., and Kolenda, F. (2003). Weibull analysis of quasi-static crushing strength of catalyst particles. *Chemical Engineering Research and Design*, 81(8):953–962.
- Sullivan, J. and Lauzon, P. (1986). Experimental probability estimators for weibull plots. *Journal of Materials Science Letters*, 5(12):1245–1247.

- Tabibnejad, A., Heshmati, A., Salehzadeh, H., and Tabatabaei, S. H. (2015). Effect of gradation curve and dry density on collapse deformation behavior of a rockfill material. *KSCE Journal of Civil Engineering*, 19(3):631–640.
- Takei, M., Kusakabe, O., and Hayashi, T. (2001). Time-dependent behavior of crushable materials in one-dimensional compression tests. *Soils and Foundations*, 41(1):97–121.
- Tapias, M., Alonso, E. E., and Gili, J. A. (2015). A particle model for rockfill behaviour. *Géotechnique*, 65(12):975–994.
- Tarantino, A. and Hyde, A. F. (2005). An experimental investigation of work dissipation in crushable materials. *Géotechnique*, 55(8):575–584.
- Teixeira, R. (2009). *Computational modelling of structures using discrete and finite elements*. PhD thesis, Swansea University, UK.
- Thornton, C. (2000). Numerical simulations of deviatoric shear deformation of granular media. *Géotechnique*, 50(1):43–53.
- Thornton, C. (2015). Granular dynamics, contact mechanics and particle system simulations. *Springer, New York*, 24:25.
- Thornton, C. and Antony, S. (2000). Quasi-static shear deformation of a soft particle system. *Powder Technology*, 109(1-3):179–191.
- Thornton, C. and Barnes, D. (1986). Computer simulated deformation of compact granular assemblies. *Acta Mechanica*, 64(1-2):45–61.
- Thornton, C., Ciomocos, M., and Adams, M. (2004). Numerical simulations of diametrical compression tests on agglomerates. *Powder Technology*, 140(3):258–267.
- Thornton, C., Yin, K., and Adams, M. (1996). Numerical simulation of the impact fracture and fragmentation of agglomerates. *Journal of Physics D: Applied Physics*, 29(2):424.
- Todisco, M. C., Coop, M. R., Guo, Q., and Senetakis, K. (2015). The effect of the coordination number on particle crushing. In *International Symposium on Geomechanics from Micro to Macro, IS-Cambridge 2014*, pages 1063–1068. Taylor and Francis-Balkema.
- Tombs, S. G. (1969). *Strength and deformation characteristics of rockfill*. PhD thesis, Imperial College London.
- Tsoungui, O., Vallet, D., and Charmet, J.-C. (1999). Numerical model of crushing of grains inside two-dimensional granular materials. *Powder Technology*, 105(1-3):190–198.

- Turcotte, D. L. (1986). Fractals and fragmentation. *Journal of Geophysical Research-Solid Earth*, 91(B2):1921–1926.
- Tyler, S. W. and Wheatcraft, S. W. (1989). Application of fractal mathematics to soil water retention estimation. *Soil Science Society of America Journal*, 53(4):987–996.
- Ueda, T., Matsushima, T., and Yamada, Y. (2013). Dem simulation on the one-dimensional compression behavior of various shaped crushable granular materials. *Granular matter*, 15(5):675–684.
- Ueng, T.-S. and Chen, T.-J. (2000). Energy aspects of particle breakage in drained shear of sands. *Géotechnique*, 50(1):65–72.
- Vallerga, B., Seed, H., Monismith, C., and Cooper, R. (1957). Effect of shape, size, and surface roughness of aggregate particles on the strength of granular materials. In *Road and Paving Materials*. ASTM International.
- Varadarajan, A., Sharma, K., Abbas, S., and Dhawan, A. (2006). The role of nature of particles on the behaviour of rockfill materials. *Soils and foundations*, 46(5):569–584.
- Varadarajan, A., Sharma, K., Venkatachalam, K., and Gupta, A. (2003). Testing and modeling two rockfill materials. *Journal of Geotechnical and Geoenvironmental Engineering*, 129(3):206–218.
- Vasistha, Y., Gupta, A. K., and Kanwar, V. (2013). Medium triaxial testing of some rockfill materials.
- Verdugo, R. and de la Hoz, K. (2007). Strength and stiffness of coarse granular soils. In *Soil Stress-Strain Behavior: Measurement, Modeling and Analysis*, pages 243–252. Springer.
- Walker, F. and Holtz, W. (1953). Control of embankment material by laboratory testing. *Transactions of the ASCE*, 118(1):1–25.
- Walsh, K. D., Houston, W. N., and Houston, S. L. (1997). Field implications of current compaction specification design practices. *Journal of Construction Engineering and Management*, 123(4):363–370.
- Wang, B., Martin, U., and Rapp, S. (2017). Discrete element modeling of the single-particle crushing test for ballast stones. *Computers and Geotechnics*, 88:61–73.

- Wang, J. and Gutierrez, M. (2010). Discrete element simulations of direct shear specimen scale effects. *Géotechnique*, 60(5):395–409.
- Wang, J. and Yan, H. (2013). On the role of particle breakage in the shear failure behavior of granular soils by dem. *International Journal for Numerical and Analytical Methods in Geomechanics*, 37(8):832–854.
- Wang, L., Zhu, J., Zhang, Z., and Zheng, H. (2021). Effects of dry density on shear behavior and particle breakage for slate rockfill material. *Bulletin of Engineering Geology and the Environment*, 80(2):1181–1192.
- Wang, P. and Arson, C. (2016). Discrete element modeling of shielding and size effects during single particle crushing. *Computers and Geotechnics*, 78:227–236.
- Wang, Y. and Tonon, F. (2010). Calibration of a discrete element model for intact rock up to its peak strength. *International Journal for Numerical and Analytical Methods in Geomechanics*, 34(5):447–469.
- Weatherley, D., Hancock, W., and Boros, V. (2014). Esys-particle tutorial and user’s guide version 2.1. *Earth Systems Science Computational Centre, The University of Queensland*.
- Weerasekara, N., Powell, M., Cleary, P., Tavares, L. M., Evertsson, M., Morrison, R., Quist, J., and Carvalho, R. (2013). The contribution of dem to the science of comminution. *Powder Technology*, 248:3–24.
- Weibull, W. (1951). A statistical distribution function of wide applicability. *Journal of Applied Mechanics*, 18(3):293–297.
- Weng, H., Zhu, J., Yu, T., and WANG, G.-q. (2009). Status quo and tendency of studies on scale effects of coarse-grained materials. *Journal of Hohai University (Natural Science)*, 37(4):425–429.
- White, D., Bergeson, K., Jahren, C., and Wermager, M. (1999). Embankment quality: Phase ii final report. Technical report, Center for Transportation Research and Education, Iowa State University.
- Wood, D. M. and Maeda, K. (2008). Changing grading of soil: effect on critical states. *Acta Geotechnica*, 3(1):3.

- Xiao, Y., Liu, H., Chen, Y., and Jiang, J. (2014a). Strength and deformation of rockfill material based on large-scale triaxial compression tests. i: Influences of density and pressure. *Journal of Geotechnical and Geoenvironmental Engineering*, 140(12):04014070.
- Xiao, Y., Liu, H., Chen, Y., and Jiang, J. (2014b). Strength and deformation of rockfill material based on large-scale triaxial compression tests. ii: Influence of particle breakage. *Journal of Geotechnical and Geoenvironmental Engineering*, 140(12):04014071.
- Xiao, Y., Liu, H., Zhang, W., Liu, H., Yin, F., and Wang, Y. (2016). Testing and modeling of rockfill materials: A review. *Journal of Rock Mechanics and Geotechnical Engineering*, 8(3):415–422.
- Xiao, Y., Meng, M., Daouadji, A., Chen, Q., Wu, Z., and Jiang, X. (2020). Effects of particle size on crushing and deformation behaviors of rockfill materials. *Geoscience Frontiers*, 11(2):375–388.
- Xiao, Y., Sun, Y., and Hanif, K. F. (2015). A particle-breakage critical state model for rockfill material. *Science China Technological Sciences*, 58(7):1125–1136.
- Xu, M., Song, E., and Cao, G. (2009). Compressibility of broken rock-fine grain soil mixture. *Geomechanics and Engineering*, 1(2):169–178.
- Xu, W.-J., Xu, Q., and Hu, R.-L. (2011). Study on the shear strength of soil–rock mixture by large scale direct shear test. *International Journal of Rock Mechanics and Mining Sciences*, 48(8):1235–1247.
- Yamamuro, J. A. and Lade, P. V. (1996). Drained sand behavior in axisymmetric tests at high pressures. *Journal of Geotechnical Engineering*, 122(2):109–119.
- Yan, W. and Dong, J. (2011). Effect of particle grading on the response of an idealized granular assemblage. *International Journal of Geomechanics*, 11(4):276–285.
- Yang, B., Jiao, Y., and Lei, S. (2006). A study on the effects of microparameters on macroproperties for specimens created by bonded particles. *Engineering Computations*.
- Yang, Z., Xue, Y., Wang, L., Liu, X., Liu, Q., and Zhao, J. (2018). Field large-scale relative density tests of gravel soil of yulongkashi high earth-rock fill dam. In *2018 7th International Conference on Energy and Environmental Protection (ICEEP 2018)*. Atlantis Press.
- Yao, Y.-P., Liu, L., Luo, T., Tian, Y., and Zhang, J.-M. (2019). Unified hardening (uh) model for clays and sands. *Computers and Geotechnics*, 110:326–343.

- Yi, Y., Meles, D., Nassiri, S., and Bayat, A. (2015). On the compressibility of tire-derived aggregate: comparison of results from laboratory and field tests. *Canadian Geotechnical Journal*, 52(4):442–458.
- Yoshimoto, N., Hyodo, M., Nakata, Y., Orense, R. P., Hongo, T., and Ohnaka, A. (2012). Evaluation of shear strength and mechanical properties of granulated coal ash based on single particle strength. *Soils and Foundations*, 52(2):321–334.
- Zeller, J. and Wullimann, R. (1957). The shear strength of the shell materials for the goschenalp dam, switzerland. In *4th International Conference on Soil Mechanics and Foundation Engineering, Londres*, volume 2, pages 399–415.
- Zhang, Z., Yu, A., and Dodds, J. A. (1997). Analysis of the pore characteristics of mixtures of disks. *Journal of Colloid and Interface Science*, 195(1):8–18.
- Zhao, B., Wang, J., Coop, M., Viggiani, G., and Jiang, M. (2015). An investigation of single sand particle fracture using x-ray micro-tomography. *Géotechnique*, 65(8):625–641.
- Zhao, T. (2019). *The developments of multi-level computational methodologies for discrete element modelling of granular materials*. PhD thesis, Swansea University, UK.
- Zheng, W. and Tannant, D. D. (2018). Grain breakage criteria for discrete element models of sand crushing under one-dimensional compression. *Computers and Geotechnics*, 95:231–239.
- Zhong, S., Baitalow, F., Nikrityuk, P., Gutte, H., and Meyer, B. (2014). The effect of particle size on the strength parameters of german brown coal and its chars. *Fuel*, 125:200–205.
- Zhou, C. (2011). *Investigation of micro-and macro-phenomena in densely packed granular media using the discrete element method*. PhD thesis, The University of Edinburgh, UK.
- Zhou, J., Chi, Y.-w., Chi, Y., and Xu, J.-P. (2000). Simulation of biaxial test on sand by particle flow code. *Chinese Journal of Geotechnical Engineering-Chinese Edition*, 22(6):701–704.
- Zhou, W., Hua, J., Chang, X., and Zhou, C. (2011). Settlement analysis of the shuibuya concrete-face rockfill dam. *Computers and Geotechnics*, 38(2):269–280.

- Zhou, W., Ma, G., Chang, X., and Zhou, C. (2013). Influence of particle shape on behavior of rockfill using a three-dimensional deformable dem. *Journal of Engineering Mechanics*, 139(12):1868–1873.
- Zhou, W., Wang, D., Ma, G., Cao, X., Hu, C., and Wu, W. (2020). Discrete element modeling of particle breakage considering different fragment replacement modes. *Powder Technology*, 360:312–323.
- Zhou, W., Yang, L., Ma, G., Chang, X., Cheng, Y., and Li, D. (2015). Macro–micro responses of crushable granular materials in simulated true triaxial tests. *Granular Matter*, 17(4):497–509.
- Zhou, W., Yang, L., Ma, G., Chang, X., Lai, Z., and Xu, K. (2016). Dem analysis of the size effects on the behavior of crushable granular materials. *Granular Matter*, 18(3):64.
- Zhu, H., Zhou, Z., Yang, R., and Yu, A. (2007). Discrete particle simulation of particulate systems: theoretical developments. *Chemical Engineering Science*, 62(13):3378–3396.
- Zhu, J., Weng, H., Wu, X., and Liu, H. (2010). Experimental study of compact density of scaled coarse-grained soil. *Rock and Soil Mechanics*, 31(8):2394–2398.
- Zou, D.-g., Tian, J.-r., Liu, J.-m., et al. (2018). Three-dimensional shape of rockfill material and its influence on particle breakage. *Rock and Soil Mechanics*, 39(10):3525–3530.